Widely-tunable and ultra-stable hybrid-integrated diode lasers
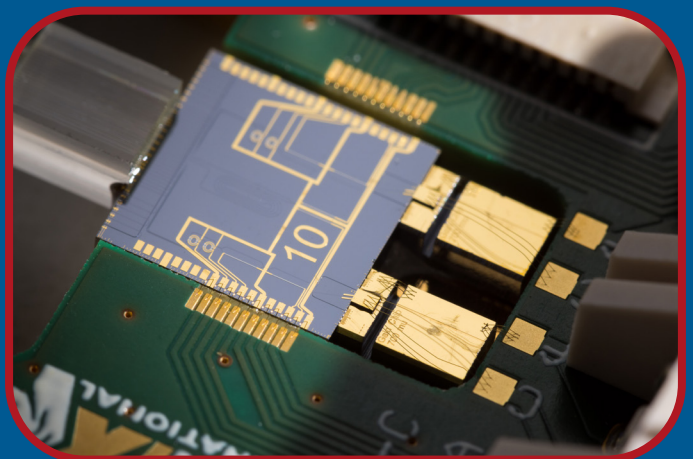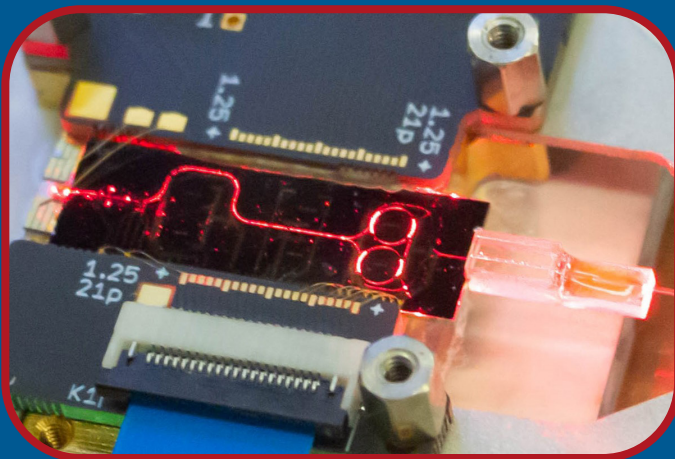
Albert van Rees

WIDELY-TUNABLE AND ULTRA-STABLE HYBRID-INTEGRATED DIODE LASERS

Albert van Rees

Widely-tunable and ultra-stable hybrid-integrated diode lasers

Dissertation

to obtain
the degree of doctor at the University of Twente,
on the authority of the rector magnificus,
prof.dr.ir. A. Veldkamp
on account of the decision of the Doctorate Board,
to be publicly defended
on Friday the 12th of January 2024 at 12.45 hours

by

Albert van Rees

born on the 20th of April 1984
in Zwolle, the Netherlands

This dissertation has been approved by:

Promotor: Prof.dr. K.-J. Boller
Co-promotor: Dr. P.J.M. van der Slot

GRADUATION COMMITTEE:

Chair/secretary:
Prof.dr. J.L. Herek   University of Twente

Promotor:
Prof.dr. K.-J. Boller   University of Twente

Co-promotor:
Dr. P.J.M. van der Slot   University of Twente

Members:
Prof.dr. M. Burla   Technische Universität Berlin
Prof.dr. C. Fallnich   Universität Münster
Prof.dr.ir. H.L. Offerhaus   University of Twente
Prof.dr. P.W.H. Pinkse   University of Twente

Contents

Chapter 1

Introduction

Nowadays, lasers are used in unaccountably many situations, from high power lasers for laser welding, consumer products such as optical mice and DVD players, to the backbone of the internet based on optical communication via guiding laser light through glass fibers. When the laser was invented 65 years ago, its current impact was still unthinkable. Although the special properties of lasers were clear at the time, especially the brightness of laser light, there was no direct application yet. Therefore, the laser was also called a *"bright solution looking for a problem"* [1]. A few years before the first laser was demonstrated, a microwave device for stimulated emission was already built, called maser (microwave amplification by stimulated emission of radiation). At that time Schawlow and Townes [2] wrote their seminal paper about *"the extension of maser techniques to the infrared and optical region"* in which they predicted remarkably monochromatic emission if the output frequency of masers would be increased to optical wavelengths. Two years later, the first working device for stimulated emission at the optical wavelength of 694.3 nm was demonstrated by Maiman [3] and the optical maser was eventually called laser (light amplification by stimulated emission of radiation).

Since the first ideas about the laser became reality, the ideal has always remained to create sources for light emission with the highest possible stability and controllability. Schawlow and Townes emphasized that the most desirable features would be *"a high order of monochromaticity and tunability"*. However, it appeared unreasonable to them to expect *"more than a small fractional amount of tuning in an infrared or optical maser using discrete levels"* [2]. Obviously, this sentence was written before the invention of the laser diode [4, 5], which came about 4 years after their comment. The present state of the art, and especially of the diode lasers presented in this thesis, is clearly beyond what Schawlow and Townes had seen as impossible. In short, the monochromaticity of specific lasers can be much higher than that of masers, while diode lasers can be tuned within a vast spectral range from the far-infrared into the ultra-violet.

1.1   Laser applications

After building the first lasers, these light sources inspired the discovery of many new applications. The reason is that lasers are well-behaved compared to classic light sources in terms of the purity and controllability of the emitted light regarding wavelength, polarization, power, pulse duration, spatial distribution and spectral coherence. Lasers can emit monochromatic light with a high spectral purity, called spectral or temporal coherence, which means that the frequency and wavelength of the light are well-defined and stable. This property is often addressed as narrow linewidth, low frequency noise, or low phase noise. A high degree of coherence is beneficial for many applications, or even enables certain applications, such as when transmitting data in optical communications, or when retrieving data from the environment via optical sensing. In addition to coherence, it is often important that the laser wavelength is adjustable for a broad the range of applications. It turns out that attempting to realize a universal laser with all its properties optimized is not realistic. On the other hand, providing a universal laser is not essential because, usually, each individual application requires only some of the properties of the laser output to be optimized.

For instance, the ever growing demand for higher data rates and transmission bandwidths for fiber-optic links requires compact, robust, and electrically driven light sources that can be tuned to and frequency stabilized to specific infrared channels in a frequency grid as defined by the International Telecommunication Union (ITU). Optimizing additionally for ultra-low phase noise then enables the increase of data rates via advanced modulation formats [6] that use phase encoding in addition to amplitude encoding [7, 8, 9]. Such coherence-optimized diode lasers would find application in long-haul fiber networks and short-reach fiber links [10], supporting also high-capacity wireless communication between fixed antennas and mobile stations [11]. They would also be instrumental as an optical carrier in optical beam forming networks [12] and as on-chip oscillators for microwave photonics [13]. We note that these applications mostly make use of laser wavelengths around 1.55 μm, because the propagation loss in silica glass fibers is lowest [14]. The same reasoning applies to integrated silicon photonic circuits having their lowest optical loss in that wavelength range [15].

The mentioned examples make obvious how important the role of lasers is for communication in our society. However, there are many more applications where the use of lasers is more hidden and indirect, such as for ultra-high resolution and precision metrology. An example are optical clocks [16, 17], which are, due to their unprecedented accuracy, capable to determine tiny local changes in the gravity potential, such as between the middle of a mountain vs tens of kilometer away [18]. There are recent experiments that resolve even gravitational redshifts within millimeter-scales in atomic samples, thanks to a fractional frequency uncertainty smaller than 10^{-20} [19]. Stable clocks also enable accurate positioning via satellite navigation, because time and distance are linked to each other via the speed of light. Realizing state-of-the-art optical clocks requires tunability of the laser to a set of very specific wavelengths often including the visible and the ultra-violet. The same holds true for the preparation and interrogation of atomic quantum states, as this requires a combination of ultra-low phase noise and long-term frequency stability of the laser.

Traditional laser technology based on bulk optical components such as using mirrors or fibers has so far been a main approach to serve most of named applications. However, many more options open up if the required light sources can be integrated in their minimum format as integrated photonic devices on a chip. Next to the size advantage, a main benefit of integrating the laser is that this removes the instability that is often associated with bulk optical laser cavities, replacing it with the inherent stability of photonically integrated resonators. An example of metrology benefitting from laser integration are small sensors for autonomous traffic based on coherent optical ranging through frequency-modulated continuous-wave (FMCW) light detection and ranging (LiDAR) [20, 21, 22]. Similarly, devising chip-sized diode lasers for lowest phase noise can be used to detect motion, based on the optical laser Doppler vibrometry (LDV). Applications are found for instance in acoustic characterization in the car industry, or for quality screening in fabrication of micro-electromechanical systems (MEMS) that serve as inertial sensors, i.e., as accelerometers and gyroscopes. Actually, part of this thesis contributed to this field. Our team took part in a European research project (3PEAT) to devise low-linewidth chip-sized diode lasers to be embedded in subsequent photonic circuitry. The project provided a showcase example of how low-phase-noise diode lasers at infrared telecom wavelengths can be exploited to develop a fully integrated, 2D-scanning laser Doppler vibrometer (LDV) module [23, 24].

The embedding of integrated diode lasers with further waveguide circuity and components on the same chip is beneficial also for other sensing applications, e.g., for on-chip sensing of methane [25] and other gases [26], or as biosensors for lab-on-a-chip applications [27, 28, 29]. Integrating the laser on the same chip can make the overall system more robust and compact. However, sensing applications often require a broader range of optical frequencies. To access wider wavelength ranges, it is of interest to employ diode laser gain chips with different quarterny compositions, or to integrate frequency conversion on the same chip as the laser. Recent examples of broadband nonlinear conversion are pumping Kerr frequency combs with chip-integrated diode lasers [30, 31], enabling integrated dual-comb sources for spectroscopic sensing [32].

Nonlinear conversion of chip-integrated diode lasers may also involve small frequency shifts. For instance, Brillouin amplifiers provide frequency shifts of the order of 10 GHz which is of high interest to enable RF-quality information processing of microwaves with optical methods, specifically, when using mature photonic platforms [33]. Similarly, it should be possible to embed Brillouin lasers [34] with sub-Hz linewidths [35] driven by a narrowband diode laser on the same chip.

Embedding an increasing number of highly coherent diode lasers with further photonic components on the same chip, i.e., upscaling the number and density of light sources on chips, is likely of interest also for applications that still lie in the future. This is certainly the case for quantum information processing. The reason is that photonic integration can be the key for upscaling towards high-complexity systems as precondition for high functionality [36, 37, 38]. Specifically, chip-integration of ultra-low linewidth lasers at multiple visible and ultraviolet wavelengths is of relevance for upscaling atom and ion-based quantum processing [39, 40, 41]. The challenge is

that integration must maintain tunability and highest coherence as needed for optical cooling and trapping [42], and for warranting sufficient phase stability of quantum gates. Alternatively, diode lasers integrated in a hybrid photonic platform can serve as source of entangled quantum states [43] to be used to scale up chip-integrated photonic quantum processors.

To wrap up this overview, lasers assisted by integrated photonics have indeed developed into one of the key enabling technologies of our time. Looking back to the enormous impact that the laser already has made, with every new laser or laser concept often discovered out of pure curiosity, also chip-integrated lasers will bring tremendous inspiration and lead to yet undiscovered applications.

1.2   Chip-integrated lasers

In the following we describe the present state of the art with chip-integrated lasers that are of interest when requiring compactness, portability or usage in increasingly high numbers. A well known approach to meet this is the lithographic fabrication of lasers, which began already with the first developments of laser diodes. The first spectrally well-controlled and fully-integrated diode lasers were the so-called distributed Bragg reflector (DBR) and distributed feedback (DFB) lasers. However, for many applications the linewidth of such lasers turned out as too broad and the tuning ranges were too limited.

As described to more detail in the bulk of the thesis, this has inspired the development of hybrid and heterogeneously integrated diode lasers, where part of the laser resonator is located in an additional photonic circuit. Using strong and frequency-selective feedback in the form of an integrated extended cavity laser, the reduction in intrinsic linewidth became indeed remarkable, reaching below 100 Hz with heterogeneous integration [44] and down to 40 Hz with hybrid integration [45]. An alternative is enhancing the spectral stability by weak feedback from an external high-Q resonator at the predefined frequencies of a standard diode laser, referred to as self-injection locking. This technique had shown linewidths down to the 1-Hz-level [46, 47, 48] and even as low as 40 mHz [49]. Although these are impressive achievement, it needs to noted that there are also disadvantages, such as the requirement for careful adjustment of the optical feedback phase, or the restriction to the light frequencies given by the solitary laser before it is self-locked. In comparison, extended cavity diode lasers, either hybrid or heterogeneously integrated with ring resonators offer free and wide tunability across the entire gain bandwidth [50, 51], while the feedback phase setting can be used for fine-tuning.

Due to available technology and interest from telecom applications, the spectral evolution of hybrid and heterogeneously integrated lasers started in the optical communications band around 1.55 μm, based on feedback waveguide circuits made from silicon [52]. Only afterwards, progress toward narrower linewidth and wider spectral coverage began based on a closer understanding of wavelength and intensity limits with silicon, when also the fabrication technology for different waveguide platforms became more mature, such as involving silicon nitride [53]. The trends that

can be identified are that the spectral range became extended to longer wavelengths for applications of molecular detection, and to the range of shorter wavelengths, for targeting, e.g., atomic transitions. In recent years, the range has significantly expanded with lasers toward the mid-infrared [54, 55, 56, 57, 58, 59, 60] and near-infrared [61, 62, 63, 64, 65, 66, 67, 68, 69]. Regarding shorter wavelengths, hybrid and heterogeneously integrated lasers are about to conquer the visible range [70, 71]. The first visible laser of this kind is presented in this thesis [72], while the coverage is meanwhile reaching out towards the violet range [73, 74, 75].

To enable or support the solidification and widening of spectral coverage, several photonic platforms have matured over the last decades, making them compatible for integration with diode amplifiers or diode lasers. Each platform has its specific advantages, making it suitable for a certain range of wavelengths and functionalities. For example, for the telecom range, silicon on insulator (SoI) waveguides can be fabricated using standard CMOS processing and its high index contrast allows for integration of many components on small chips [50, 76, 77]. Alternatively, e.g., III-IV semiconductor platform excels in the integration of light sources with high-speed modulators and detectors on the same chip [78]. However, for the expansion towards the visible range, and for further reduction of losses, other materials with a wider electronic band gap than silicon or indium phosphide were required. Silicon nitride (Si_3N_4) embedded in silicon oxide (SiO_2) can extend the spectral transparency window for feedback circuits down to almost 400 nm [79, 80], in this range offering a good combination of a moderately tight confinement with very low propagation loss. These properties make the silicon nitride platform highly suitable for microring resonators for sharp spectral filtering [81, 82]. Other materials that might be of interest for cost reduction are polymers [83], whereas lithium niobate ($LiNbO_3$) with its strong second order nonlinearity offers non-linear conversion and fast modulation [22, 84].

Regarding the approach for integrating the waveguides of diode amplifiers with feedback circuits, there are various options available, of which we briefly review the main properties along the state-of-the-art. Presently, this integration is progressing along three main routes, known as heterogeneous integration, hybrid integration and micro-transfer printing. Heterogeneous integration appears promising for large-volume fabrication at the wafer-level [50, 76, 85, 77, 48]. This technique is based on growing or surface bonding dissimilar layers of different materials to each other, which is restricted by material compatibility, such as lattice size or thermal expansion coefficients. Micro-transfer printing uses a stamp to pick-up pre-fabricated components, such as amplifiers and detectors, to press them on a target substrate containing feedback circuits [86, 87]. This enables high fabrication throughput as well, but it introduces restrictions regarding materials and thermal management. A challenge common to heterogeneous integration and micro-transfer printing is that coupling between waveguide layers usually requires adiabatic couplers, which tend to suffer from coupling loss. Hybrid integration as the third approach is based on permanently edge-coupling the diode amplifier with a feedback chip, or coupling to output fibers. One important advantage of the approach is that it allows almost fully independent optimization of the individual components and thus may be applied even to elevated powers [88, 89, 90]. A second advantage is that edge coupling is less sensitive to
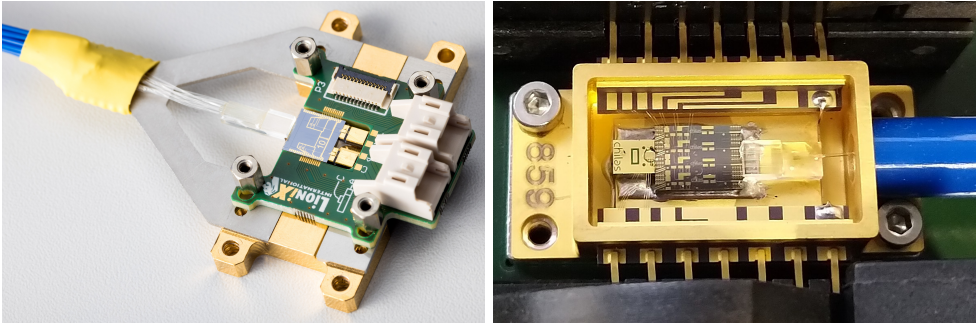
Figure 1.1: Photos of two different types of laser assemblies, with in both cases a semiconductor gain chip and a fiber array are coupled and fixed to a Si_3N_4 feedback circuit. (a) In this open assembly, two gain chips are attached to a single feedback chip. Photo by Gijs van Ouwerkerk, PHIX Photonics Assembly. (b) Here the laser assembly is mounted in a standard 14-pin butterfly package, and on-chip controls are wire bonded with the pins of this package.

coupling loss or undesired back-scattering, because tapering can be used for low-loss mode matching (0.2-dB level [91]) in combination with anti-reflection coatings and slightly angled waveguides vs the facet normal, all of which enhances the purity of laser emission. Also of interest for hybrid integration are the use of photonic wire bonds as coupling elements between different chips [92] and flip-chip integration [93, 94]. These methods are aiming on large volume production as well, but are still under investigation and development to reduce losses in mode matching. All of the named approaches ultimately require so-called packaging, which consists of electrical, thermal and optical interfacing to the environment via wire bonding, thermoelectric cooling and fiber arrays.

For the lasers described here, we decided to use hybrid integration followed by packaging to benefit from the named advantages with maximally independent optimization of components and relatively low coupling loss.

1.3 Thesis outline

In this thesis, we investigate widely-tunable and frequency-stable hybrid-integrated diode lasers using silicon nitride-based feedback circuits. At first thought, tunability and stability seem like directly opposing each other, and thus cannot be optimized simultaneously. However, having both properties simultaneously is often required since stability enables precision, while tunability is essential for making systematic use of precision. The tunability of a laser depends mainly on the design of the waveguide feedback circuit, while the stability of depends in addition on the mechanical and thermal and, also, on the stability of the various electrical currents that provide gain or induce phase changes in the laser circuitry. As a result, the type of lasers that are under investigation here cannot be brought to the intended stability and tunability without a sufficiently high degree of technical development regarding their mechanical,

thermal, and electrical environment and driving. To give an impression of the high degree of technical development, which introduces frequency stability and reliability, Fig. 1.1 shows two typical examples of the lasers investigated here.

The following parts of this thesis are arranged as follows. In chapter 2 we recall the theory for spectral filtering using waveguide circuits and the theory regarding spectral stability of hybrid integrated diode lasers using these waveguide circuits. In chapter 3 we present a theoretical analysis of wavelength tuning with emphasis on extending the continuous, i.e., mode-hop free tuning range of a narrow-linewidth hybrid integrated laser. The chapter also presents corresponding experimental results and a demonstration of recording absorption lines of acetylene near 1.54 μm wavelength via mode-hop free tuning. The first demonstration of a hybrid integrated laser operating in the visible spectrum is presented in the following chapter 4. The visible wavelength range around 685 nm is chosen to demonstrate that the wavelength coverage may include absorption lines of strontium. To investigate the options for long-term stability of hybrid integrated lasers, we describe in chapter 5 our results on locking the laser frequency to an acetylene absorption line and, alternatively, to a fiber-based optical frequency discriminator. We note that the central part of the thesis is written in a cumulative manner, i.e., chapters 3-5 are presented as already published in scientific journals. Therefore, each chapter is self-contained with its own introduction, conclusion and outlook. Finally, in chapter 6, we summarize the results and provide a broader perspective and outlook on the research field.

Chapter 2

Theoretical aspects

2.1 Introduction

Basic laser theory shows that the finite linewidth of a laser is determined by residual frequency fluctuations. The fundamental component of these fluctuations is caused by spontaneous emission, addressed as the Schawlow-Townes limit [2], which scales with the reciprocal of the laser cavity length squared. In addition to spontaneous emission, technical noise further broadens the laser linewidth. Reducing technical noise contributions to the linewidth is typically easier for lasers with a small Schawlow-Townes linewidth, by using feedback loops and, e.g., lock the laser frequency to an external reference.

Widely used diode lasers, capable of emitting a single wavelength, are distributed Bragg reflector (DBR) and distributed feedback (DFB) lasers. Due to a short cavity length, typically a few hundred micrometer, with an associated relatively broad linewidth in the MHz-range. To circumvent these limitations, and to obtain single mode lasing with a narrow Schawlow-Townes linewidth, it was already proposed in 2001 [95] to couple a diode laser with a microring resonator (MRR). The filtering mechanism of a microring resonator would provide a very sharp Lorentzian shaped transmission peak, to select a single laser mode, and to achieve a linewidth reduction below 100 kHz by effectively extending the on-chip optical cavity length of the laser.

Figure 2.1 shows schematically the realisation of this approach, as we use it here. The essential components comprise a semiconductor optical amplifier (SOA) with a high reflection coating on one facet, a phase section, two sequential microring resonators in a loop mirror to provide wavelength selective feedback, and a tunable coupler to direct part of the light to the output port of the laser. The output of the laser is available via a fiber that is coupled to the output port.

To provide a low-loss feedback circuit for the diode laser, bending losses will limit the workable ring radius, and thus limit the free spectral range of the filter to values smaller than the relatively broad gain bandwidth of diode lasers. Multiple ring resonances would fall within the gain bandwidth and feedback at those frequencies could
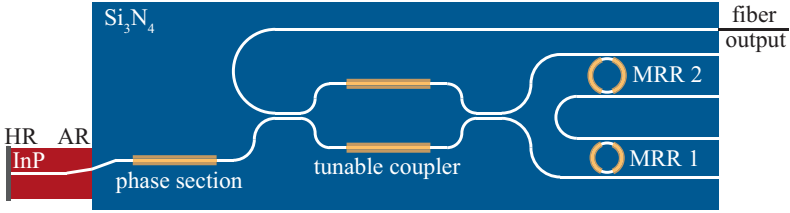
Figure 2.1: Schematic view of a typical hybrid-integrated laser, as investigated in this thesis, comprising an optical amplifier and a waveguide feedback circuit. The InP-based amplifier is coated with a high-reflection (HR) and an anti-reflection coating (AR). The Si_3N_4-based waveguide feedback chip contains a phase section and two microring ring resonators (MRR) in a loop mirror to provide frequency selective feedback. A balanced Mach-Zehnder interferometer, which functions as a tunable coupler, is used to extract part of the intracavity light and direct it to the output of the laser. Heaters for thermal tuning are indicated in yellow.

lead to multi-mode lasing. However, by using a combination of two or more microring resonators as filter, a free spectral range of the filter equal to or surpassing the gain bandwidth can be obtained via the so-called Vernier effect [96, 53], thereby allowing single mode and narrow linewidth operation over the complete gain bandwidth of the diode laser. For example, by integrating two ring resonators in a low loss circuit and coupling the circuit with a semiconductor optical amplifier, the linewidth can be reduced by several orders of magnitude with regard to standard DBR and DFB lasers, to the range of 10 kHz [53, 97, 98]. Further extension of the cavity length, e.g., by adding a third ring resonator, has enabled us to reach an extremely narrow linewidth of 40 Hz [45]. In addition, using ring resonators for spectral filtering has the advantage that a small change to the optical length of one of the rings, e.g., by using heater elements to increase the roundtrip phase, is enhanced with respect to a single roundtrip, because the lifetime of the light inside the ring is much larger than one roundtrip time. In chapter 3, we present a theoretical analysis for extending the mode-hop-free tuning range based on this effect and we confirm the analysis with experimental data. Here, we continue in section 2.2 with the theoretical description of spectral filtering using waveguide feedback circuits, and in section 2.3 with an analytical model for calculating the frequency stability of diode lasers using these feedback circuits.

2.2 Optical feedback circuits

Optical waveguides are used to guide the light within the photonics chips, as interconnect between different building blocks and as the the basic element to construct building blocks, such as resonators, couplers or loop mirrors. A waveguide comprises of a material of higher refractive index, which is surrounded by a material with lower refractive index, often labelled as core and cladding. The index contrast between core and cladding allows electromagnetic waves to be confined in the transverse plane, which can be seen in the picture of geometrical optics, as caused by total internal

reflection. Dependent on the size and shape of the waveguide, the wavelength and the index contrast, one or more transverse optical modes are guided for each polarization.

In this work, waveguides are typically optimized for two conditions. The first condition is that only one transverse mode is guided. The reason is that the functionality of building blocks depends on which mode is selected. A further problem is, even if only one mode is excited, the light from that mode can in principle couple to other modes at non-adiabatic transitions or at scattering interfaces. Thus, to prevent also such mode conversion, the waveguide should be designed to only support a single transverse mode, which is usually the lowest order (fundamental) mode. The second condition is that only a small fraction of light is lost in waveguide bends. Namely, bending a waveguide leads to radiation loss, also called bend loss, which depends on the bend radius and the mode confinement. If the mode is sufficiently confined, even sharply bent waveguides or ring resonators with tight bend radii can be used for low-loss guiding.

For finding an optimized waveguide cross section, via retrieving the mode field distribution, propagation constant and bend losses, typically, numerical mode solvers are used. The propagation constant for each mode is given by

$$\beta = \frac{2\pi n_{\text{eff}}}{\lambda} \tag{2.1}$$

where n_{eff} is called waveguide effective index and λ is the vacuum wavelength. The effective index is usually wavelength dependent due to chromatic dispersion of the core and cladding materials and due to the so-called form dispersion, which depends on the chosen cross section. The propagation constant of a selected transverse mode and the corresponding effective index are needed, e.g., for calculating the resonance condition in resonators. When the calculation involves a range of wavelengths, also the group index n_g is required, which is given by [99]

$$n_g = n_{\text{eff}} - \lambda \frac{\delta n_{\text{eff}}}{\delta \lambda} \tag{2.2}$$

which can be understood as the waveguide index to quantify the propagation delay of a pulse that travels through a dispersive waveguide.

During the last decades, the development of integrated optics has provided a large toolkit of building blocks that can be used to design a laser feedback circuit. For designing such circuit, several consideration need to be take into account. For this work, one goal is to provide tunable and narrowband feedback to select a single laser frequency and to narrow the laser linewidth. The problem to be solved is that solitary semiconductor lasers typically have a broad linewidth due to their short roundtrip length and high internal loss. As we discuss in section 2.3.2, a narrow linewidth can be achieved with extending the laser cavity length with a low-loss dielectric waveguide. However, when extending the cavity length, the cavity modes become closely spaced and laser oscillation might happen at multiple modes. Often, single mode oscillation is desired with a high side mode suppression ratio (SMSR). Therefore, in addition to extending the length, spectrally sharp filtering is required using tunable intracavity elements to select a single cavity mode.

Extending the laser cavity also requires to implement some reflective (mirror-like) element, which sends light back to the semiconductor amplifier. Such mirror element could be implemented in a feedback circuit using a Bragg grating, a multi-mode interferometer (MMI) or a looped waveguide in combination with a directional coupler (Sagnac mirror). It should be taken into account that other elements in or outside the laser cavity should not cause any undesired back reflections, as these, if too strong, would affect the linewidth and tunability of the laser. For example, MMI's and Y-junctions are known to cause noticeable back-reflections and thus should be avoided, except when employing them as mirror. As a frequency filter element in a feedback circuit, several building blocks could be considered, for example arrayed waveguide gratings (AWGs), Bragg waveguides, Mach-Zehnder interferometers (MZIs) or microring resonators (MRRs).

Using ring resonators has several advantages. As we show in the next section, properly chosen sets of ring resonators can provide both frequency filtering for single mode selection and extending the laser cavity length for linewidth reduction. An additional advantage of ring resonators is that they can be defined using the same standardized lithography as for other waveguides of the feedback circuit.

What finally requires consideration is where the light is coupled out from the circuit. Typically, advanced feedback circuits can be designed to have multiple outputs. Most advantageous is to couple the light out after a filter, to reduce the amount of broadband amplified spontaneous emission in the laser output.

2.2.1 Ring resonators

The hybrid lasers described have add-drop ring resonators [95] as a filter element. Such a resonator comprises a ring waveguide and two bus waveguides, as schematically shown in Fig. 2.2. The basic working principle of an add-drop ring resonator is as follows. Light is coupled into the input port of the bottom bus waveguide. Via a directional coupler, some fraction of the input light can be coupled to the ring waveguide. More specifically, only light which fulfills the resonance condition for the ring, i.e., for which the total roundtrip phase is an integer multiple of 2π, will be coupled to the other bus waveguide, towards the drop port. The remainder of the light, is transmitted to the through port.

The propagation of the electric field from the input port E_{in} to the drop port E_d can be described as [99]

$$E_d = \frac{-\kappa^2 \sqrt{a} e^{\frac{1}{2}j\theta_{rt}}}{1 - t^2 a e^{j\theta_{rt}}} E_{\text{in}} \tag{2.3}$$

and from the input port to the through port as

$$E_t = \frac{t - t a e^{j\theta_{rt}}}{1 - t^2 a e^{j\theta_{rt}}} E_{\text{in}} \tag{2.4}$$

where t and κ are the self-coupling and cross-coupling coefficients, respectively, of the directional couplers. Here, we assume identical, symmetric and loss-free couplers, such that t and κ are real quantities. In this case, the power splitting ratios t^2 and κ^2
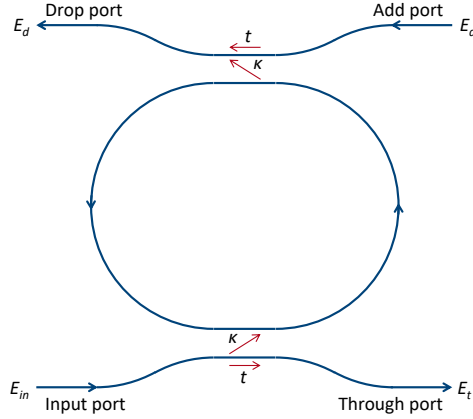
Figure 2.2: Schematic of an add-drop ring resonator with two bus waveguides and a ring waveguide. The central ring resonator waveguide is shaped as a so-called racetrack. The central straight coupling section between the bus and ring waveguides can be considered as a directional coupler, with self-coupling and cross-coupling field coefficients t and κ, respectively.
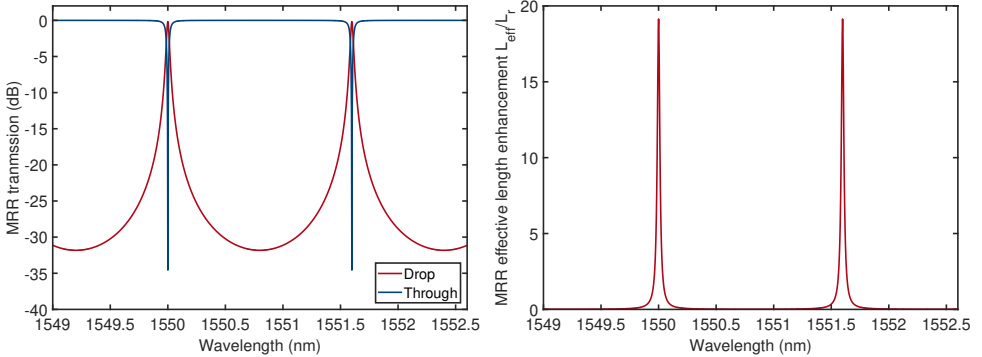
Figure 2.3: (a) Transmission to the drop (red) and through port (blue) of an add-drop ring resonator, displayed as function of wavelength. The ring parameters are chosen based on a typical ring as used in the hybrid integrated lasers described in this work, based on TriPleX ADS waveguides, with $n_g = 1.77$, $\gamma = 0.1$ dB/cm, $L_r = 850$ μm and $\kappa^2 = 0.05$. One resonance is centered around $\lambda = 1550$ nm by adding a small phase shift to the light propagating in the ring, as could be done using a thermal phase shifter. The corresponding effective length between input and drop port for this ring is shown in (b).

of the coupler satisfy the condition $\kappa^2 + t^2 = 1$. The single roundtrip field transmission coefficient a can be calculated from the waveguide propagation losses α_b [dB/m] and the roundtrip length of the ring L_r, using $a^2 = 10^{-\alpha_b L_r}$. The total roundtrip phase θ_{rt} is given by $\theta_{rt} = \beta L_r = \frac{2\pi n_{\text{eff}}}{\lambda} L_r$ where λ is the vacuum wavelength. The transmission T_d to the drop port can be calculated from Eq. 2.3 as $T_d = |\frac{E_d}{E_{\text{in}}}|^2$.

Figure 2.3(a) shows the ring transmission to the drop and through port for a typical ring as used in this work. The parameter values, as used for the plot are shown in table 2.2, can well be realized using the Si_3N_4 platform, specifically using a TriPleX asymmetric double stripe (ADS) waveguide core cross section [100]. In Fig. 2.3(a) two resonances are displayed, where the drop transmission is maximal and the through transmission is minimal. These resonances are found when the roundtrip phase fulfills the resonance condition $\theta_{rt} = 2\pi$. The frequency or wavelength distance between these ring resonances $\Delta\lambda_r$ is called the free-spectral range (FSR) of the ring resonator, and is given by

$$\Delta\lambda_r = \frac{\lambda^2}{n_g L_r} \tag{2.5}$$

where n_g is the group index of the waveguides on the feedback chip. The denominator $n_g L_r$ is a measure of the optical length of the resonator. The reason that the group index appears in this denominator is because the optical length is calculated at two frequencies, and the group index forms a first order correction of the dispersion of the waveguide effective index.

For laser operation, the effective length contribution of the ring resonator to the laser cavity is of particular interest. As we show in the next section, this effective length is relevant for the cavity mode spacing and for the laser linewidth. When a ring resonator is placed inside a laser cavity, the ring adds to the laser cavity a certain frequency-dependent effective length. The according enhancement of the effective length at resonance can most easily be understood as due to the large number of roundtrips that the light makes inside the ring resonator. In contrast with Mach-Zehnder interferometers and Bragg gratings, ring resonators can have an effective length that is much longer than the physical length of the device [95].

To determine the effective length, we first calculate the phase delay θ_d of the light passing from the input port to the drop port, which can be calculated from the phase of Eq. 2.3, namely $\arg(E_d/E_{in})$. The effective length is a measure of the delay at two closely spaced frequencies with respect to each other, which is also called the group delay, as given by [95]

$$L_{r,\text{eff}} = -\frac{1}{2\pi}\frac{\lambda^2}{n_g}\frac{\delta\theta_d}{\delta\lambda} \tag{2.6}$$

At resonance, the effective length is maximally increased, since the derivative of the phase versus wavelength $\frac{\delta\theta_d}{\delta\lambda}$ is steepest on resonance. When assuming that the waveguide propagation loss can be neglected with respect to the coupling coefficient κ, the effective length on resonance becomes

$$L_{r,\text{eff}} \cong \left(\frac{1}{2} + \frac{1-\kappa^2}{\kappa^2}\right) L_r \tag{2.7}$$

In this expression, the effective length comprises an additional term $\frac{1}{2}L_r$. This originates from the half-roundtrip between the input and drop port, whereas the term $\frac{1-\kappa^2}{\kappa^2}L_r$ is the resonant contribution, due to multiple roundtrips. Especially for a ring with low coupling coefficient κ, the effective length will be significantly extended.

Figure 2.3(b) shows the effective length enhancement factor $\frac{L_{\text{eff}}}{L_r}$ as function of wavelength, calculated using Eq. 2.6 for the same ring parameters used in Fig. 2.3(a).

	$\kappa^2 \gg 1 - a^2$ "overcoupled"	$\kappa^2 \approx 1 - a^2$ "critically coupled"	$\kappa^2 \ll 1 - a^2$ "undercoupled"	
κ^2	0.05	0.002	0.0001	
$L_{r,\text{eff}}$	16.3	285	782	mm
$T_{\max}$	-0.16	-3.5	-20.7	dB
FWHM	3.3	0.19	0.068	GHz
F	60	1054	2913	
Q_{loaded}	$5.8 \cdot 10^4$	$1.0 \cdot 10^6$	$2.8 \cdot 10^6$	
Q_{int}	$3.1 \cdot 10^6$	$3.1 \cdot 10^6$	$3.1 \cdot 10^6$	

Table 2.1: Comparison of various figures of merit for a ring resonator with different coupling coefficients. The coupling coefficients are chosen to be much larger, equal to and much lower than the ring internal losses. The ring parameters are based on a standard ring resonator fabricated from TriPleX ADS waveguides, with $n_g = 1.77$, γ = 0.1 dB/cm, and $L_r = 850$ μm.

Quantitatively in this example, the coupling with a coefficient of $\kappa^2 = 0.05$, Eq. 2.7 provides a maximum enhancement of 19.5. It can be noted that the maximum enhancement on resonance in Fig. 2.3(b) is slightly lower, namely only 19.1, because (unlike Eq. 2.7), we included also the propagation losses. Far from resonance, the effective length reduces to zero. However, the laser operates at a wavelength where the net gain is maximal, which means that the laser will not operate far from a ring resonance where the drop transmission is very low.

In section 2.3.2 we show that the linewidth of a hybrid laser becomes reduced approximately inverse to the square of the laser's resonator length. Following Eq. 2.7, it looks therefore straightforward to reduce the coupling coefficient. However, this also increases the losses for the light propagating from input port to the drop port of the ring, and therefore decrease the feedback to the laser amplifier. To calculate these losses, the drop port transmission on resonance is given by

$$T_{\max} = \left(\frac{\kappa^2 \sqrt{a}}{1 - t^2 a} \right)^2 \tag{2.8}$$

An evaluation of Eqs. 2.8 and 2.7 for certain values of the coupling coefficients is provided in Table 2.1, for the cases where the coupling coefficient is much lower, equal to or much larger than the ring roundtrip loss. For completeness, we also show figures of merit, that describe the filter characteristics of a ring resonator [101]. The full-width at half-maximum (FWHM) of the drop transmission is given by

$$\text{FWHM} = \frac{\lambda^2}{\pi n_g L_r} \frac{1 - t^2 a}{\sqrt{t^2 a}} \tag{2.9}$$

The quality or Q-factor of the ring resonator indicates the number of optical cycles of the field before losses cause a reduction to 1/e of the initial energy. The Q-factor can also be regarded as the stored energy divided by the power lost per optical cycle. The

so-called loaded Q-factor includes the losses due to coupling to the bus waveguides

$$Q_{\text{loaded}} = \frac{\lambda}{\text{FWHM}} = \frac{\pi n_g L_r}{\lambda} \frac{\sqrt{t^2 a}}{1 - t^2 a} \tag{2.10}$$

The intrinsic or unloaded Q-factor indicates the Q-factor when the ring would not be coupled to bus waveguides, and therefore the self-coupling coefficient t is set to 1.

$$Q_{\text{int}} = \frac{\pi n_g L_r}{\lambda} \frac{\sqrt{a}}{1 - a} \tag{2.11}$$

The Finesse F represents the number of roundtrips before the light energy is reduced to 1/e of the initial energy

$$F = \frac{\Delta \lambda_r}{\text{FWHM}} = \pi \frac{\sqrt{t^2 a}}{1 - t^2 a} \tag{2.12}$$

In Table 2.1 one can see that a smaller coupling coefficient increases the effective length, and reduces the FWHM, which is beneficial for a low linewidth and proper single mode selection, when such a ring is part of a laser feedback filter. However, the maximum drop port transmission is also reduced, which means that the cavity losses increase, which would reduce the laser output power and make the laser susceptible to spurious feedback, e.g., from backscattering and facet reflections.

2.2.2 Vernier filters

For single-frequency operation, a single ring resonator is often not sufficient. The reason is that typical laser diodes provide gain over a large bandwidth, from tens of nm up to more than 100 nm. To provide sufficient spectral selectivity, an extremely short resonator length would be required to provide a comparably sized FSR of more than 100 nm. Equation 2.5 describes quantitatively how the ring FSR can be increased by reducing the roundtrip length. For example, to achieve a FSR of 100 nm around 1550 nm, the ring radius needs to be reduced to about 2 μm. However, such small bend radii in waveguides would usually lead to excessive bending losses. A second limitation appears in case of a tunable ring resonator where a phase shifter is attached to the ring to provide up to 2π phase for tuning over the full ring FSR. A small ring radius also shortens the available tuning length of a phase shifter attached to the ring. If the phase shifter cannot be tuned over 2π phase shift, the laser tuning range would also be limited to a fraction of the ring FSR.

An interesting approach to increase the filter FSR, without reducing the size of the ring resonator, is to use two ring resonators with slightly different ring radii in series, in a so-called Vernier configuration, as was proposed by [96] and demonstrated by [52]. The FSR of such Vernier filter, $\Delta \lambda_v$, comprising two ring resonators with FSRs $\Delta \lambda_{r1}$ and $\Delta \lambda_{r2}$ is given by:

$$\Delta \lambda_v \equiv M_{r1} \Delta \lambda_{r1} = M_{r2} \Delta \lambda_{r2} \tag{2.13}$$

where M_{r1} and M_{r2} need to be co-prime numbers. Using co-prime numbers is essential to exploit the Vernier principle. The reason is that for a set of number with a common
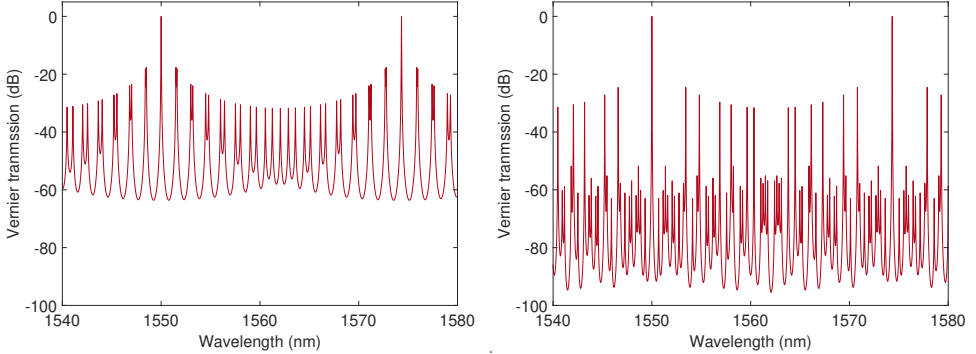
Figure 2.4: Transmission of a Vernier filter as function of wavelength for a Vernier filter comprising 2 ring resonators (a) and 3 ring resonators (b). The base ring in each filter has a roundtrip length of $L_{r1} = 850$ μm, and otherwise the same parameters as in Fig. 2.3. For the 2-rings filter, the second ring has a length of $L_{r2} = 16/15 L_{r1}$. For the 3-rings filter, the ring lengths are $L_{r2} = 7/5 L_{r1}$ and $L_{r3} = 7/3 L_{r1}$, where 3, 5 and 7 are a set of co-prime numbers. The ring resonances are all centered around the central wavelength of 1550 nm by adding the required extra phase.

divisor, the Vernier FSR will be increased only by a much smaller factor equal to that common divisor.

To evaluate the Vernier FSR, we rewrite Eq. 2.13 and obtain

$$\Delta\lambda_v = |M_{r2} - M_{r1}| \frac{\Delta\lambda_{r1}\Delta\lambda_{r2}}{|\Delta\lambda_{r1} - \Delta\lambda_{r2}|}. \tag{2.14}$$

A common choice for co-prime numbers is a pair of sequential integers, such that $|M_{r2} - M_{r1}| = 1$ [53]. In this case, Eq. 2.14 can be simplified to

$$\Delta\lambda_v = \frac{\Delta\lambda_{r1}\Delta\lambda_{r2}}{|\Delta\lambda_{r1} - \Delta\lambda_{r2}|} \tag{2.15}$$

An example of the transmission function of such a Vernier filter comprising two rings is shown in Fig. 2.4(a). Here, the first ring is the same one as described in Fig. 2.3, with a FSR of about 1.6 nm. For the size of the second ring, M_{r1} and M_{r2} are chosen as 15 and 16 respectively. The two rings in series then provide a Vernier FSR of 24 nm, and a transmission that is at least 17 dB higher than that of the intermediate transmission peaks, called Vernier side peaks. The Vernier FSR could be further increased by a taking larger numbers for M_{r1} and M_{r2}. However, this would also reduce the suppression of the side peaks next to the central Vernier peaks. To improve the side peak suppression, the coupling ratios to the ring could be reduced, but this would decrease the maximum transmission of the light propagating through the Vernier filter.

By using Vernier filters in a hybrid integrated laser, very large tuning ranges have been demonstrated, for example 139 nm [102] and 172 nm [51]. Although two ring resonators are typically sufficient for creating a large tuning range, there are

some benefits of further increasing the number of ring resonators. Indeed, Vernier filters with three [103, 104, 45, 76, 105, 44] or four ring resonators [50] have been demonstrated. Adding a third ring resonator with again a slightly deviating size from the first and second ring increases the tuning range, while maintaining a high SMSR [103, 76, 105, 44]. An alternative approach was taken in [104, 45] where the size of the third ring is a multiple of the first ring. This third ring mainly contributes to the cavity length extension for linewidth reduction, while the tuning range is given by the first two rings.

Properly optimizing a multi-ring filter for optimal SMSR, requires some extra considerations. For a Vernier filter that comprises more than 2 ring resonators, Eq. 2.13 can be extended. For example for 3 ring resonators we obtain

$$\Delta\lambda_v \equiv M_{r1}\Delta\lambda_{r1} = M_{r2}\Delta\lambda_{r2} = M_{r3}\Delta\lambda_{r3} \qquad (2.16)$$

where M_{r1}, M_{r2} and M_{r3} need to be co-prime. Unfortunately, with three or more ring resonators, there is no convenient formula available (such as Eq. 2.15 for two rings) to express the Vernier range as function of the ring FSRs. Nevertheless, to illustrate such a filter, Fig 2.4(b) shows the transmission response of a three ring filter where the first ring is again the same one as for Fig. 2.3. Next, M_{r1}, M_{r2} and M_{r3} are chosen as 3, 5 and 7 respectively, which forms a set of co-prime numbers. The total Vernier range of this ring filter is again 24 nm, which is the same as for the 2-ring filter shown in Fig 2.4(a). Clearly, the effect of the third ring is that the SMSR is improved, especially for a spectral band of a few nm width around the central Vernier peaks.

In Fig. 2.4 it can be seen that for the 3-ring filter especially in the frequency range of a few nm around the central wavelength (1550 nm) the selectivity of the filter has much improved in comparison with the 2-ring filter. As a direct illustration of the benefit of the resulting, high side mode suppression of a 3-ring Vernier filter, we name our collaboration work lead by Michael Kues in the Leibniz University Hannover [43]. We designed and had fabricated a hybrid integrated laser with a double-passed 3-ring and co-prime Vernier filter, originally intended for further linewidth narrowing and stronger side-mode suppression. The laser was then successfully applied for entangled photon pair generation. The detected photon pairs are generated by four wave mixing in the third ring of the Vernier filter. In order to distinguish these photon pairs from the amplified spontaneous emission (ASE), it is required that the first two rings between the gain section and the third ring provide sufficient filtering of the ASE at the frequencies where these photons are generated. For this laser, initially a side mode suppression ratio (SMSR) of >55 dB was measured of the ASE level with respect to the laser field, however, that measurement was limited by the dynamic range of the optical spectrum analyzer used. Using higher sensitivity photon counting measurements allowed determination of a much higher SMSR of ~112 dB at the frequency where the photon pairs are generated. The high ASE suppression through multiple co-prime microring resonators is what then made it possible to detect photon pairs with a high coincidence-to-accidental ratio of ~80 [43].

2.2.3 Laser cavity and longitudinal modes

In order to prepare the discussion of results on mode-hop free tuning, and the optimization of the lowest linewidth, it is important to illustrate the spectrum of the cold cavity modes (longitudinal modes) for lasers with ring resonator filtering. The frequency or vacuum wavelength of modes in the waveguide laser resonator can be calculated using the roundtrip condition $\theta_{rt} = n2\pi$ with n an integer number. The roundtrip phase θ_{rt} is given by

$$\theta_{rt} = \frac{2\pi}{\lambda}\left(2n_{\text{eff},a}L_a + 2n_{\text{eff},b}L_b\right) \tag{2.17}$$

where L_a is the geometrical length of the amplifier and L_b is the effective geometrical length of the feedback circuit.

Typically for the lasers described in this work, the feedback circuit includes the length of bus waveguides L_{bus} that are passed twice per laser cavity roundtrip and ring resonators with $L_{r,\text{eff}}$ that are passed once per cavity roundtrip. The designation "$_{\text{eff}}$" symbolizes that the effective length of an intracavity ring resonator strongly depends on the wavelength detuning with respect to a resonance (see Fig. 2.3(b)). The total length of the feedback circuit comprises the sum of all these contributions

$$L_b = L_{\text{bus}} + \frac{1}{2}\Sigma L_{r,\text{eff}} \tag{2.18}$$

Since the effective length of an intracavity ring resonator is strongly dependent on the wavelength, the effective length of the laser resonator is also strongly dependent on the wavelength. This is why also the spectral distance between laser cavity modes (free spectral range) is non-uniform. Therefore, a simple equation for the mode spacing, similar to Eq. 2.5 for a single ring resonator, is not valid for the laser cavity modes. Nevertheless, to find the distance between the cavity modes, Eq. 2.17 can be evaluated numerically. Fig. 2.5(a) illustrates the wavelengths of the laser cavity modes, together with the central Vernier transmission peak of the example of a 2-ring Vernier filter. In this case, the central cavity mode is tuned, via tuning the length of the bus waveguide, to coincide with the central Vernier peak. This is the optimal condition for single-mode operation of the laser, since it provides the highest SMSR for the neighbouring cavity modes. In Fig. 2.5(a) it can clearly be seen that the distance between the cavity modes is smallest around the central Vernier peak, where a higher number of ring resonator roundtrips extends the laser cavity maximally. The distance between laser cavity modes increases further away from the Vernier peak.

We note that the cavity modes can also be tuned to the situation as shown in Fig. 2.5(b). There, two adjacent cavity modes are tuned to experience equal feedback from the Vernier filter. In that situation, the laser would start to oscillate at two frequencies simultaneously, while four-wave mixing (FWM) and laser amplification generate further side bands to form a frequency comb. Details on our work towards comb generation and an explanation of the underlying dynamics can be found in references [106, 107] and [108], respectively.

If a laser is to be tuned mode-hop-free, as described in chapter 3, this can be achieved with proper synchronous tuning of the strongest-feedback cavity mode and
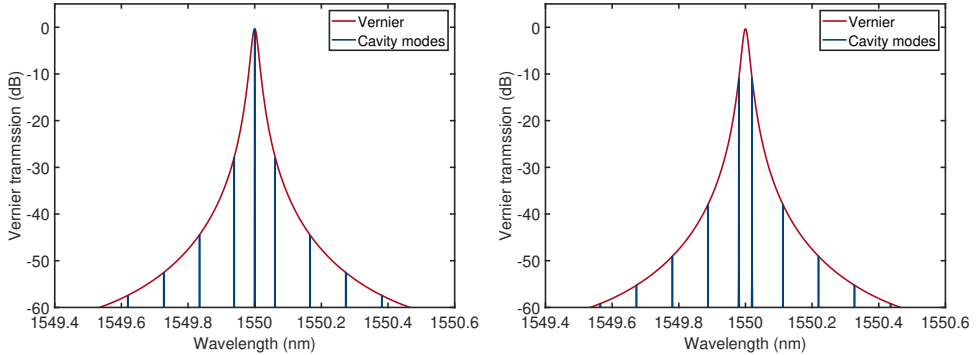
Figure 2.5: Vernier filter transmission (red curve) and cavity mode mode positions (blue) for a hybrid integrated laser with typical dimensions (Table 2.2) and a Vernier filter as in Fig. 2.4(a). The non-uniform distance between the cavity modes is due to steep phase dispersion of the ring resonators, meaning that a higher number of roundtrips increases their effective length contribution to the cavity. Therefore, the distance between the cavity modes is smallest close to the ring resonances. The relative alignment of the laser cavity modes with respect to the maximum Vernier transmission can be controlled with an intra-cavity phase tuning element in the bus waveguide. The two extreme options for tuning the laser cavity modes relative to the peak of the Vernier filter transmission are displayed here, namely perfect alignment (a) and maximum detuning (b).

ring resonators together. If a laser is to be tuned for minimum linewidth, as described in section 2.3.2, this can be achieved by a small detuning to the red wing of the Vernier filter.

2.3 Frequency stability

2.3.1 Noise sources

As was briefly mentioned in the introduction, the linewidth of a laser is a rather complex output property. In fact, stating a single number for a linewidth is far from describing the true degree of frequency stability. The residual frequency instability of lasers is best described by the so called power spectral density of frequency noise, because there the frequency deviations from average are quantified versus the timescale (Fourier frequency) at which they occur. This figure of merit then often allows to even discriminate the main physical processes from each other, that contribute to frequency noise at certain timescales. Figure 2.6 shows a schematic plot of the main noise components found in hybrid-integrated diode lasers with their power spectral density. The strongest noise typically occurs at long observation times (low Fourier frequencies) and is addressed as technical noise, often following a $1/f$ dependence. The underlying effects are, e.g., instabilities of the diode pump current, temperature variations and acoustic perturbations. The laser line shape due to $1/f$ noise can be approximated as a Gaussian, for which the linewidth can be calculated by integrating
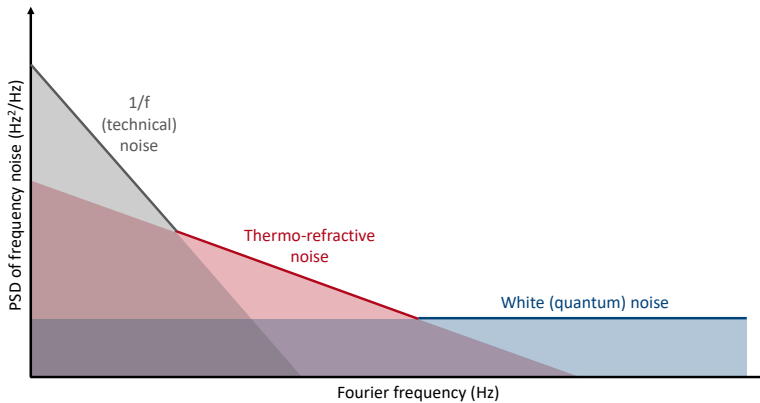
Figure 2.6: Schematic plot of the power spectral density (PSD) of frequency noise versus the Fourier frequency. The noise contributions that are typically found in hybrid-integrated diode lasers are shown in different colors.

the noise for frequencies above the so-called β-separation line [109]. A reduction of this noise typically requires technical countermeasures, such as a laser resonator with an intrinsically stable length, and, ultimately, an active stabilization of the laser frequency with regard to a natural reference, for example a molecular transition. This is described in chapter 5.

At the other extreme, at short timescales, laser frequency fluctuations are associated with the well-known Schawlow-Townes limit, also addressed as fundamental, intrinsic, and short-term stability, and quantum noise. The unique signature of this type of frequency noise is that it has a constant, finite value even toward highest noise frequencies, also called white noise. The line shape due to this noise can be approximated as a Lorentzian, for which the linewidth can be calculated by multiplying the white noise level with π or 2π, depending on whether the spectral density is specified as a single-sided or double-sided noise spectrum, respectively [109]. Reducing this quantum noise requires to control the relative amount of random spontaneous emission versus intended stimulated emission. It is important to apprehend that reducing the quantum noise is an important precondition for an effective frequency stabilization with active control methods. The reason is that the finite bandwidth of photodetection, electronics and delay in servo loops limit the frequency range over which noise can be actively reduced. A detailed physical description for the case of diode lasers and quantum noise reduction by cavity length extension by narrowband intracavity spectral filtering is described below.

Intermediate between technical and quantum noise lies noise of thermo-dynamic origin. The spectral shape of this noise depends on quite some details, specifically regarding the narrow spectral filters, named before. In integrated lasers, as investigated here, the thermo-dynamic noise shows as so-called thermo-refractive noise, that originates from small index fluctuations, even at constant temperature. Realizing an integrated diode laser with low frequency noise across the entire spectrum is a rather

challenging task. To face this challenge, ultimately with short and long-term stability, it is important to identify the parameters that determine the quantum noise and thermo-refractive noise.

2.3.2 Spectral linewidth

The spectral purity of laser light is one of the main benefits of laser light. Schawlow and Townes [2] suggested that the light generated in a resonator by stimulated emission has a much narrower linewidth than the linewidth of the resonator itself. Different from a maser, where noise is mainly of thermal origin, in an optical laser it is the spontaneous emission into the laser mode that causes random phase changes to the intracavity laser field. Therefore, spontaneous emission would form the fundamental limit to the laser linewidth. Since spontaneous emission is a random process with equal strength at all Fourier frequencies, the resulting linewidth has a Lorentzian shape [109]. Various names for this linewidth component can be found in literature, namely, the fundamental, intrinsic, Lorentzian, or Schawlow-Townes linewidth of the laser. To calculate its value for the lasers considered here, we use an adopted version of the expression introduced by Schawlow and Townes, that is adapted for such hybrid-integrated diode lasers using a separate feedback circuit with narrowband filtering. In Appendix A we start with the approach as described in the textbook by Milonni and Eberly [110], and we express the linewidth $\Delta\nu_{\mathrm{ST}}$ in terms of measurable quantities for a hybrid laser that comprises an optical amplifier and a feedback circuit.

Here, we consider the special case as schematically depicted in Fig. 2.7 and expressed in Eq. A.23, where a feedback circuit contains a spectral filter with transmission $T_b^{\rightarrow}$. The amplifier has a back facet mirror (1) with reflectivity $R_1 = |r_1|^2$, and the feedback circuit includes an end mirror with a reflectivity $R_2 = |r_2|^2$, where the main output power P_{out} is extracted from the laser cavity. In that case, the linewidth can be expressed as

$$\Delta\nu_{\mathrm{ST}} = \frac{1}{4\pi} \frac{v_{g,a}^2 h\nu \eta_{\mathrm{sp}} \alpha_m \alpha_t}{P_{\mathrm{out}}\left(1 + \frac{1-R_1}{1-R_2}\sqrt{\frac{R_2}{R_1}}\frac{1}{\sqrt{T_b^{\rightarrow}}}\right)} \tag{2.19}$$

The group velocity of the light in the amplifier waveguide is $v_g = \frac{c}{n_g}$ and $h\nu$ is the photon energy of the emitted light. The spontaneous emission factor n_{sp}, also called the population inversion factor [50] is given by $\eta_{\mathrm{sp}} = N_2/(N_2 - N_1)$, where N_2 and N_1 are the occupation densities of the upper (conduction band) and lower level (valence band) of the lasing transition in stationary state, respectively. The factor $\frac{1-R_1}{1-R_2}\sqrt{\frac{R_2}{R_1}}\frac{1}{\sqrt{T_b^{\rightarrow}}}$ accounts for additional output power emitted from the amplifier back facet, which is not measured since no fiber is attached there typically. The mirror loss coefficient per unit length, spatially averaged over the gain section is given by

$$\alpha_m = -\frac{1}{2L_a}\ln[R_1 R_2] \tag{2.20}$$

with L_a the length of the amplifier chip. The total roundtrip loss coefficient per unit
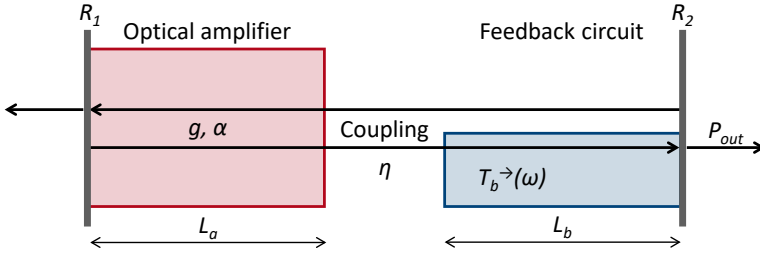
Figure 2.7: Schematic of a hybrid laser comprising an optical amplifier and a feedback circuit, having length L_a and L_b, respectively. Light propagates via waveguides on both chips that are coupled with coupling efficiency η. The gain and loss coefficients of the amplifier are defined as g and α, respectively. The transmission through the feedback chip is defined as $T_b^{\rightarrow}(\omega)$, the mirror reflectivities are defined as R_1 and R_2, and the light coupled out from the resonator through the mirror on the right side is the main output power P_{out}.

length, spatially averaged over the gain section, is

$$\alpha_t(\omega) = -\frac{1}{2L_a} \ln\left[R_1 T_a^2 \eta^2 T_b^{\rightarrow}(\omega) R_2\right], \tag{2.21}$$

where $T_a = e^{-\gamma_a L_a}$ is the power transmission of a single pass through the gain section, with γ_g the loss coefficient for passive loss in the gain section.

Although Eq. 2.19 predicts the inverse dependency of the laser linewidth vs. the output power correctly, for diode lasers with spectrally narrow feedback, several correction factors need to be applied. In the following we discuss several of these correction factors.

The first correction comes from a mechanism that is present in diode lasers, called gain-index coupling [111]. Spontaneous emission in any laser causes random intensity changes next to phase changes. These intensity changes cause changes in inversion and the gain coefficient, which changes the imaginary part of the refractive index. Different from other lasers, in a diode laser, any change of inversion (any change of the gain) is associated with a non-negligible change of the real part of the refractive index. This is caused by the gain profile having a strongly asymmetric spectral shape. In the high-frequency wing of the gain spectrum there is strong absorption, increasing with the light frequency. In contrast, in the low-frequency wing, the gain becomes less as well but there is no absorption below the band edge frequency. The Kramers–Kronig relations then yields a gain-dependent index, with the following consequence for the laser linewidth. A change in the real refractive index also causes a variation in the optical length of the laser cavity, which broadens the laser linewidth. This broadening effect is described by the Henry linewidth enhancement factor $\alpha_H = \frac{dn'/dN}{dn''/dN}$, which expresses the ratio between the change in real refractive index dn' versus the change of the imaginary index dn'' with a change of the carrier density dN. To account for this broadening effect, a correction factor of $\left(1 + \alpha_H^2\right)$ is added to the linewidth expression. In semiconductor lasers, this α_H can be between and 3 and 6 [110], so the linewidth is much increased by gain-index coupling.

For lossy cavities due to low mirror reflectivities, a second correction factor needs to be applied to describe excess spontaneous emission noise [110]. The consequence of large output coupling is that high gain is required to balance these high losses to enable laser operation. Due to the high gain, spontaneous emission will be amplified, and this must be taken into account for the laser linewidth. This spontaneous emission enhancement factor, also called the Peterman factor [88], is given [112] as:

$$\alpha_P = \left[\frac{(r_1 + r_2)(1 - r_1 r_2)}{2 r_1 r_2 \ln (r_1 r_2)} \right]^2 \tag{2.22}$$

The factor approaches unity, when the mirror reflectivities are close to 1. However, for lower mirror reflectivities α_P can be much higher.

Finally, for a laser with a spectrally narrowband feedback filter, the linewidth becomes much reduced [113, 88, 50], expressed using the third correction factor, namely the so-called chirp reduction factor F [114]

$$F(\omega) = 1 + A(\omega) + B(\omega) \tag{2.23}$$

In this expression, A is the reduction factor, equivalent to the effective length extension of the feedback circuit (see Eq. 2.18).

$$A(\omega) = \frac{1}{\tau_a} \frac{d}{d\omega} \phi_{\text{eff}}(\omega) \tag{2.24}$$

with $\tau_a = \frac{2 n_{g,a} L_a}{c}$ the photon roundtrip time in the amplifying laser section. The linewidth reduction factor B describes the additional linewidth reduction at the rising slope of the feedback filter.

$$B(\omega) = \frac{\alpha_H}{\tau_a} \frac{d}{d\omega} \ln |r_{\text{eff}}(\omega)| \tag{2.25}$$

The origin of this B-factor can be explained as an optical negative feedback effect that helps to stabilize the laser frequency (also called detuned loading) [50]. When the lasing frequency is at the rising slope of the feedback filter, and if some perturbation slightly increases the light frequency, this also increases the mirror reflectivity, which increases the photon density and reduces the carrier density. Due to the coupling between the carrier density and the refractive index, described by the Henry factor, the refractive index increases, which increases the optical cavity length and reduces the laser frequency. Essentially the initial perturbation becomes undone via detuned loading and gain-index coupling. In contrast to this stabilizing effect on the rising slope, the linewidth becomes increased at the descending slope. The increase can broaden the linewidth so much that it destabilizes the laser, such that it hops to a more stable adjacent cavity mode.

To obtain the frequency dependent reflectivity r_{eff} and phase delay ϕ_{eff} of the feedback filter, we define an effective mirror as

$$r_{\text{eff}}(\omega) = |r_{\text{eff}}(\omega)| e^{-i\phi_{\text{eff}}(\omega)} \tag{2.26}$$

Symbol	Value	Unit	Description	Ref
L_a	700	μm	Length SOA waveguide	[98]
n_g	3.6		Group index SOA waveguide	
α_a	1607	m^{-1}	Passive loss SOA waveguide	
R_1	0.9		Reflectivity of SOA back facet	
η	0.8		Coupling efficiency SOA and feedback circuit	
R_2	0.2		Reflectivity of feedback circuit end mirror	
n_{sp}	2		Spontaneous emission enhancement factor	
α_h	5		Henry linewidth enhancement factor	
P_a	10	mW	Output power at amplifier back facet	

Table 2.2: Laser parameters for evaluating the laser linewidth of a typical hybrid-integrated diode laser with two ring resonators.

with $R_{\text{eff}}(\omega) = |r_{\text{eff}}(\omega)|^2$ and with $\phi_{\text{eff}}(\omega)$ the frequency dependent phase shift of the feedback chip. The effective mirror reflectivity comprises the mode coupling loss η per transmission from the gain chip to the feedback chip and vice versa, the transmission trough the feedback chip $T_b^{\rightarrow}(\omega)$ and R_2 the reflectivity of the end mirror of the feedback circuit, and can be written as

$$R_{\text{eff}}(\omega) = \eta^2 T_b^{\rightarrow}(\omega) R_2. \tag{2.27}$$

Using all the described correction factors, the laser spectral linewidth can be as expressed as the following modified Schawlow-Townes linewidth

$$\Delta\nu_{\text{ST}} = \frac{1}{4\pi} \frac{v_{g,a}^2 h\nu\eta_{\text{sp}}\alpha_m\alpha_t}{P_{\text{out}}\left(1 + \frac{1-R_1}{1-R_2}\sqrt{\frac{R_2}{R_1}}\frac{1}{\sqrt{T_b^{\rightarrow}}}\right)} \left(1 + \alpha_H^2\right)\frac{\alpha_P}{F^2} \tag{2.28}$$

To illustrate Eq. 2.28 with a numerical example, we fill in the realistic laser parameters from Table 2.2 and the Vernier filter as shown in Fig. 2.4 and plot the results in Fig. 2.8. The mirror losses, linewidth reduction factors and laser linewidth are displayed as function of the frequency detuning between the main laser mode and the ring resonances, while both ring resonances are perfectly aligned to each other. Due to the strong variation of the total mirror loss (see Fig. 2.8(a)) and the linewidth reduction factors (see Fig. 2.8(b)), the laser linewidth also varies strongly with laser detuning (see Fig. 2.8(c)) The lowest linewidth is obtained for a slightly red-detuned laser frequency, due to the stabilizing detuned loading effect, underlying the linewidth reduction factor B.

Although Eq. 2.28 is the most complete linewidth expression for the lasers described here, it should not be mistaken as if it can exactly predict the fundamental linewidth of the laser. The mean-field approximation of a uniform optical field inside the laser cavity leaves an uncertainty that could be up to a factor of two [112]. Further uncertainties enter via several parameters of the laser. For instance the Henry linewidth enhancement factor is usually not a constant but depends on internal diode
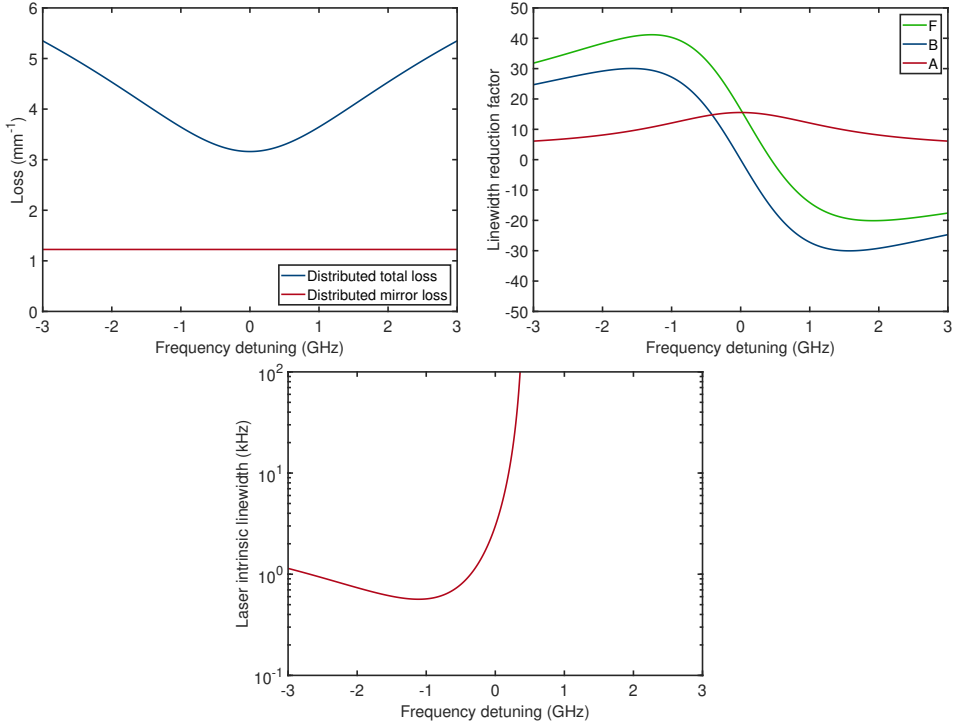
Figure 2.8: Numerical results of an analytical model to predict the laser's intrinsic linewidth as function of laser detuning, for a typical hybrid integrated laser. The frequency detuning is defined as the offset between the laser mode and the ring resonances. (a) Distributed mirror losses for only the cavity end mirrors (red) and the total laser cavity (blue). (b) Linewidth reduction factors for a narrow spectral filter A, B and F. (c) The laser's intrinsic linewidth. The lowest linewidth is obtained for a slightly red-detuned laser.

parameters that are difficult to access after fabrication, and also on the specific operation conditions [115]. If an agreement between experiment and model within an order of magnitude is achieved, we consider this successful.

2.3.3 Thermo-refractive noise (TRN)

Another main contributor to noise in hybrid lasers, especially in the kHz-to-MHz frequency range, is thermo-refractive noise (TRN). Therefore, we treat this noise source separately. Recently, it was demonstrated that thermo-refractive noise is a dominant noise source in silicon nitride based ring resonators [116]. Since the hybrid lasers described here are based on feedback from such ring resonators, any noise in the resonant frequency also affects the frequency stability of the laser. From thermodynamics it is well-known that the thermal energy of a medium in equilibrium at a nominally constant temperature is only a temporally and spatially averaged value. In analogy with the Brownian motion, the local thermal energy fluctuates on short

time scales, which can be regarded as local temperature fluctuations [117]. The effect of temperature fluctuations is that all temperature dependent material properties fluctuate as well, specifically, the refractive index and, thus, the optical path length of integrated waveguides.

The variance of the temperature fluctuation in a homogeneous medium is given by

$$\langle T^2 \rangle = \frac{k_\mathrm{B} T^2}{C \rho V} \tag{2.29}$$

where T is the temperature, k_B is the Boltzmann constant, C is the specific heat capacity, ρ is the material density and V the volume of the medium. The physical reason for the inverse volume dependence is simply that, over a larger volume, the fluctuations average out to a higher degree, as with all statistical effects. Within a feedback circuit, the components with the smallest volume are typically the microring resonators. It can be seen from Eq. 2.29 that decreasing the mode volume of waveguide resonators, and with it the size of photonic circuits, as desired in integrated optics, will come at the cost of an increase in temperature fluctuations. These temperature fluctuations are coupled to fluctuations of the device dimensions (thermo-elastic noise) and refractive index (thermo-refractive noise). Thermo-refractive noise is expected to be larger than thermo-elastic noise in silicon nitride ring resonators, since the dimensional variations are averaged out over the full chip, while the thermo-refractive noise is only averaged over the optical mode volume [116].

To model the amount of thermo-refractive noise as function of noise frequencies, an approximate expression was originally derived for whispering-gallery modes in microspheres [118], where the resonator is assumed to be surrounded by and in equilibrium with an infinite heat bath. The expression was shown to deliver good agreement with measurements of the thermo-refractive noise in whispering-gallery mode microresonators [117] and in silicon nitride ring resonators [116]. According to this model, the spectral density of the temperature fluctuations $S_{\delta T}$ in a microresonator is described with the following expressions

$$S_{\delta T} = \frac{k_\mathrm{B} T^2}{\sqrt{\pi^3 \kappa \rho C \omega}} \sqrt{\frac{1}{2p+1}} \frac{1}{R \sqrt{d_r^2 - d_z^2}} \frac{1}{\left[1 + (\omega \tau_d)^{3/4}\right]^2} \tag{2.30}$$

$$\tau_d = \frac{\pi^{1/3}}{4^{1/3}} \frac{\rho C}{\kappa} d_r^2 \tag{2.31}$$

where κ is the thermal conductivity and R is the resonator radius. The width d_r and height d_z of the fundamental mode are defined as half width at half maximum of the modal power distribution (in case that $d_z \geq d_r$, d_z and d_r should be swapped in Eqs. 2.30 and 2.31). Since this analytical model was derived for whispering-gallery modes in microspheres [118], the mode numbers are defined with p as the meridional mode number, given by

$$p = l - m \tag{2.32}$$

where l and m are the orbital and and azimuthal mode numbers, respectively. For the fundamental mode in a waveguide, $l = m$, so the meridional mode number p evaluates to 0.

Symbol	Value	Unit	Description	Ref
k_B	$1.38 \cdot 10^{-23}$	m^2 kg s^{-2} K^{-1}	Boltzmann constant	
κ	30	W m^{-1} K^{-1}	Thermal conductivity	[116]
ρ	$3.29 \cdot 10^3$	kg m^{-3}	Density	[116]
C	800	J kg^{-1} K^{-1}	Specific heat capacity	[116]
$\frac{dN}{dT}$	$2.45 \cdot 10^{-5}$	K^{-1}	Thermo-optic coefficient Si$_3$N$_4$	[119]
$\frac{dN}{dT}$	$0.95 \cdot 10^{-5}$	K^{-1}	Thermo-optic coefficient SiO$_2$	[119]
d_r	$0.75 \cdot 10^{-6}$	m	Mode half width	[100]
d_z	$0.6 \cdot 10^{-6}$	m	Mode half height	[100]
n_0	1.535		Mode effective index	[100]
f_0	$1.934 \cdot 10^{14}$	Hz	Resonance frequency	
R	$135 \cdot 10^{-6}$	m	Ring radius	
T	300	K	Temperature	

Table 2.3: Physical constants, material parameters and ring dimensions for evaluating thermo-refractive noise in a typical silicon-nitride ring resonator as used for the hybrid-integrated lasers.
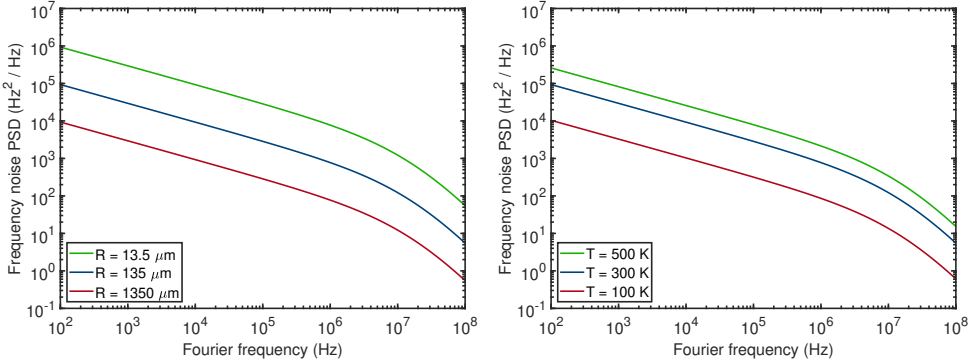
Figure 2.9: Calculated thermo-refractive noise in a silicon nitride ring resonator based on the TripleX ADS cross-section. For (a) the TRN is evaluated for a constant temperature of 300 K, while the ring radii are chosen as a standard radius of 135 μm (blue curve), 10-times larger (red curve) and 10-times smaller (green curve). For (b) the ring radius is set to 135 μm and temperature is set to a standard operation temperature of 300 K (blue curve), 500 K (green curve) and 100 K (red curve).

Finally, to convert the power spectral density of the temperate fluctuations $S_{\delta T}$ into that of the frequency fluctuations $S_{\delta f}$, we use

$$S_{\delta f} = \left(f_0 \frac{1}{n_0} \frac{dn}{dT} \right)^2 S_{\delta T} \tag{2.33}$$

where n_0 is the mode effective index for a ring resonator, and $\frac{dn}{dT}$ is the thermo-optic material coefficient.

To present typical numbers of thermo-refractive noise for a silicon-nitride ring

resonator as used for the hybrid-integrated lasers, we fill in the material constants as found in literature, which are shown in Table 2.3. For the thermo-optic coefficient we take a weighted average of the coefficients for Si_3N_4 and SiO_2. The weight factors of 15% and 85%, respectively, were found using a mode solver, and which are the fractions of the mode field powers in the respective materials.

Figure 2.9(a) shows the thermo-refractive noise PSD for a ring resonator with a standard radius of 135 μm, next to two examples with 10-times larger and 10-times smaller radius. The noise is plotted in a range from 10^2 and 10^8 Hz, because that frequency range is typically accessible in a standard noise measurement. For the ring with a radius of 135 μm, we calculate at high Fourier frequency (10^8 Hz) that the level of TRN is at 8 Hz^2/Hz. If a laser feedback circuit would be designed for quantum noise around this level (corresponding to an intrinsic linewidth $\nu_{ST} = 25$ Hz), the ring radius should be larger than 135 μm, to reveal the white noise level in a frequency noise measurement. For the ring with a 10 times larger radius, the TRN level also reduces by an order of magnitude. Therefore, in order to design a laser with an ultra-narrow linewidth, care should be taken that the ring radius is sufficiently large, such that the low white frequency noise floor can be revealed in a measurement. Alternatively, the ring resonator could be cooled down, for example to 100 K, as illustrated with the red line in Fig. 2.9(b), to reduce the TRN level. However, this is not a practical solution for standard room temperature operation of the laser. Moreover, when heater elements are used for thermal wavelength tuning, the TRN level will increase, depending on the applied heater power.

2.4 Conclusion

In this chapter we presented some central considerations regarding the design of feedback circuits and spectral filtering to reduce the frequency noise of hybrid-integrated lasers. Based on the described dependencies of quantum noise and thermodynamic noise on high contrast spectral filtering, it can be expected that tunable hybrid-integrated diode lasers can be brought to intrinsic linewidths at the kHz level in the infrared and even the visible spectral ranges. Such noise reduction using passive methods ten provides a strong base for active stabilization as well. The following three chapters present the according experimental results on record-wide mode-hop-free tuning with narrow linewidth (chapter 3), on the first hybrid-integrated laser in the visible (chapter 4), the realisation of a kHz level linewidth for such lasers (section 4.3), and the first demonstration of long-term active stabilization of a hybrid-integrated extended cavity diode laser (chapter 5).

Chapter 3

Ring resonator enhanced mode-hop-free wavelength tuning of an integrated extended-cavity laser

Extending the cavity length of diode lasers with feedback from Bragg structures and ring resonators is highly effective for obtaining ultra-narrow laser linewidths. However, cavity length extension also decreases the free-spectral range of the cavity. This reduces the wavelength range of continuous laser tuning that can be achieved with a given phase shift of an intracavity phase tuning element. We present a method that increases the range of continuous tuning to that of a short equivalent laser cavity, while maintaining the ultra-narrow linewidth of a long cavity. Using a single-frequency hybrid integrated InP-Si$_3$N$_4$ diode laser with 120 nm coverage around 1540 nm, with a maximum output of 24 mW and lowest intrinsic linewidth of 2.2 kHz, we demonstrate a six-fold increased continuous and mode-hop-free tuning range of 0.22 nm (28 GHz) as compared to the free-spectral range of the laser cavity. [1]

3.1 Introduction

Diode lasers with single-mode oscillation, mode-hop-free wavelength tunability and intrinsic low phase noise through a narrow Schawlow-Townes linewidth are instrumental in many applications. These include communication technology, for instance, to raise the data flow in fiber networks with advanced phase encoding [7], or as on-chip local oscillators for integrated microwave photonics [13]. Other applications include retrieval of information with highest precision, sensitivity, and speed, such as with spectroscopic detection, monitoring and sensing [120, 25, 121, 26], for ranging with diode-driven frequency combs [30, 122, 32], or to advance time keeping with chip-integrated, portable optical clocks [17].

In all these cases, mode-hop-free tunability is as important as a narrow linewidth. While the latter enables precision, tunability is essential to make systematic use of the precision. There might be cases where quasi-continuous or even random tuning is sufficient, provided that the data can be sorted and stitched afterwards. However, continuous tuning, without mode hops, remains essential to ensure that all possibly relevant frequencies are actually generated, so that no spectral feature can be overlooked [123]. The actual range across which mode-hop-free tunability is required, depends fully on the application. For instance, in wavelength division multiplexing tuning is required across one channel spacing of the ITU grid, which is typically a few tens of GHz. Similarly, electronic stabilization of lasers to absolute frequencies requires mode-hop-free tunability around the corresponding reference line [124].

At first sight, there appears to be conflicting optical requirements between obtaining ultra-narrow linewidth versus the spectral range across which mode-hop-free tuning is possible. The reason is that linewidth and tuning range both depend on the cavity length of the considered laser, however, in an opposing manner. When increasing the laser cavity length, L_c, this increases the cavity photon lifetime and the number of photons in the resonator, which yields an inversely quadratic reduction of the Schawlow-Townes or intrinsic linewidth, $\Delta\nu_{ST} \propto 1/L_c^2$ [2, 125, 111]. However, extending the cavity length also increases the longitudinal mode density, which, by itself, decreases the range of mode-hop-free tuning, $\delta\lambda_c \propto 1/L_c$, to the free-spectral range (FSR) of the laser, and can lead to multi-mode oscillation. This is typically resolved by inserting a tunable optical filter into the cavity. Narrow-linewidth, single-mode oscillation that can be mode-hop-free tuned over a large range is then obtained by tuning the lasing wavelength via moving one of the cavity mirrors and adjust the filter center wavelength accordingly [126, 127, 128, 129].

Such a solution cannot be pursued for fully integrated lasers, as the lasing wavelength cannot be controlled by moving parts, *i.e.*, by changing the geometric length of the laser cavity via displacement of a mirror. Instead, these lasers contain a phase section (PS) [130, 131] to change the phase of the recirculating light and, hence, its wavelength. Typically, the maximum phase tuning in integrated circuits is physically limited by the small values of material coefficients that facilitate the phase tuning, *e.g.*, the thermo-optic, strain-optic or electro-optic coefficients. To nevertheless obtain a large continuous tuning range, it is highly desirable to induce a large wavelength shift, $\delta\lambda_c$, per unit phase added by the phase section, $\delta\phi_{ps}$. Therefore, the tuning
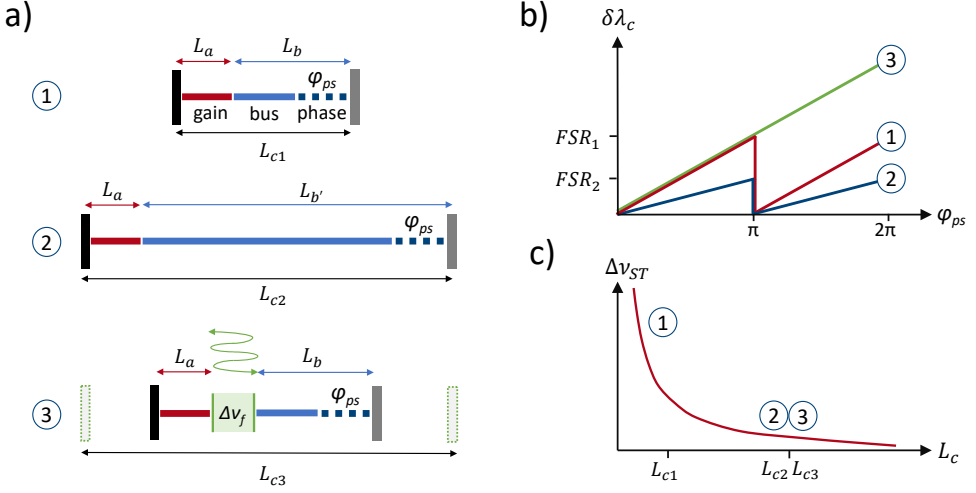
Figure 3.1: (a) Schematic view of three lasers having the same optical amplifier section but with different cavity configurations. Laser (1) has a short cavity of length L_{c1}, including a gain element of length L_a and a bus section of length L_b, which includes a phase tuning element ϕ_{ps}. The bus section length is increased for laser (2), resulting in a cavity length $L_{c2} \gg L_{c1}$. Laser (3), includes an optical filter with bandwidth $\Delta\nu_f$ that provides for both single-mode oscillation and significant enhancement of the cavity photon lifetime. The resulting effective cavity length L_{c3} is assumed to be equal to that of laser (2), while the bus waveguide is taken the same as that of laser (1). (b) The tuning behavior of the three lasers. (c) The corresponding Schawlow-Townes linewidth for the three lasers. See text for further details.

sensitivity, defined as $F_\lambda \equiv \partial\lambda_c/\partial\phi_{ps}$, should be maximized.

Figure 3.1 illustrates the tuning and linewidth limitations of integrated lasers and our strategy to obtain a large tuning sensitivity F_λ and at the same time maintain single-frequency oscillation with a narrow intrinsic linewidth. Laser 1 in Fig. 3.1(a) is a schematic representation of the simplest fully integrated laser which comprises a gain element of length L_a, and a bus section of length L_b that includes a phase section. The total cavity length $L_{c1} = L_a + L_b$ can be small and therefore the laser possesses a large tuning sensitivity $F_\lambda \propto 1/L_{c1}$. The corresponding laser cavity free-spectral range is large, enabling continuous tuning by the phase section over a range up to FSR_1, as is schematically shown in Fig. 3.1(b). On the other hand, such a configuration with a small cavity length results in a broad Schawlow-Townes linewidth, as is schematically shown in Fig. 3.1(c).

To obtain a small Schawlow-Townes linewidth, the bus waveguide can be extended to a length $L_{b'} \gg L_b$, as is schematically shown as laser 2 in Fig. 3.1(a). The total laser cavity length, L_{c2}, is now much larger than that of laser 1. Consequently, the tuning sensitivity $F_\lambda \propto 1/L_{c2}$ becomes smaller and the continuous tuning range is limited to the small FSR of the long laser cavity, as shown in Fig. 3.1(b). Nevertheless, laser 2 will have a narrow Schawlow-Townes linewidth as is shown in Fig. 3.1(c). Our

demonstration experiment of such a laser with a long cavity will confirm both the narrow Schawlow-Townes linewidth and the small tuning sensitivity F_λ, when only tuning the phase section.

In contrast to this, when a filter is added to the laser cavity that significantly increases the cavity photon lifetime, the bus waveguide can be kept short, *e.g.*, as short as the bus waveguide of laser 1. Such a laser is schematically shown as laser 3 in Fig. 3.1(a). The important difference with laser 2 is that here the cavity length is optically enlarged via enhancement of the photon lifetime by the filter, while the geometrical length remains small. Filters that enhance the photon cavity lifetime are typically resonator based [95, 53, 132, 97, 133, 134, 8, 55, 106, 45, 76] and rely on the light circulating multiple times within the resonator per roundtrip through the laser cavity. The multiple passes through the resonator effectively extend the cavity length, L_{c3} to beyond the physical mirror spacing, as is schematically indicated by the dashed mirrors. Maximizing the contribution of the optical filter to the cavity photon lifetime ensures that the laser provides single-frequency oscillation with a narrow Schawlow-Townes linewidth. Moreover, our demonstration experiment shows that the tuning sensitivity F_λ of laser 3 can be increased to that of laser 1, for the case of mode-hop-free tuning, which relies on synchronous tuning of the phase section with the resonant filter (see Fig. 3.1(b)). This mode-hop-free tuning in combination with the increased F_λ allows the continuous tuning range to extend far beyond the free-spectral range of the laser cavity.

Specifically, for the case of a filter based on two microring resonators as used in our demonstration experiment, mode-hop-free tuning requires phase shifters in both rings to keep the resonant wavelength of the rings in synchronization with the oscillating wavelength of the laser. Under this condition, the tuning sensitivity F_λ is given by (see Appendix for derivation)

$$F_\lambda \equiv \frac{\partial \lambda_c}{\partial \phi_{\mathrm{ps}}} = \frac{1}{\pi} \frac{\lambda_c^2}{2n_{g,a}L_a + 2n_{g,b}L_b}. \tag{3.1}$$

In Eq. (3.1), λ_c is the lasing wavelength, $n_{g,a}$ and L_a are the effective group index of the waveguide in the optical amplifier and its length, respectively, and $n_{g,b}$ and L_b are the according quantities for the silicon nitride bus waveguide.

Equation (3.1) summarizes our central finding: the tuning sensitivity F_λ is independent of the optical or physical length of the microring resonators that extend the overall cavity length. Therefore, Eq. (3.1) is also valid for any number of ring resonators. Essentially, this allows to extend the laser cavity length to huge values with many roundtrips through multiple ring resonators, to reduce the laser linewidth, without reducing the tuning sensitivity F_λ when the integrated laser is mode-hop-free tuned.

We note that synchronously tuning frequency-selective elements, specifically the cavity length, is well-known for mode-hop-free tuning of lasers [126, 127, 128, 129]. Our approach is novel because it goes beyond using high-finesse intracavity filters only for frequency selection. We employ also their significant multiple roundtrip length, and the variation of this length, to tune the laser cavity length and thereby increase the mode-hop-free tuning range. This approach is of particular importance
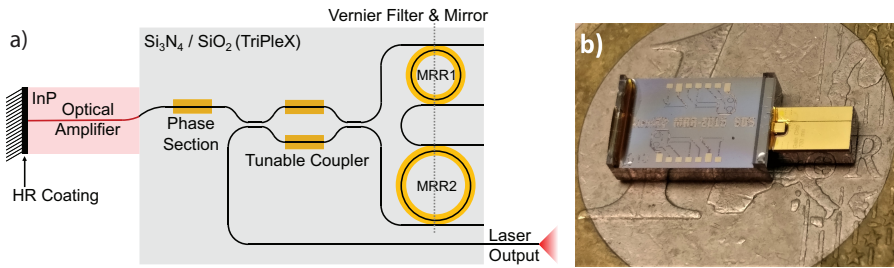
Figure 3.2: (a) Schematic view of the integrated laser. Shown are the semiconductor optical amplifier with a high reflectivity coating on one facet, the phase section, the two sequential microring resonators (MRR) in a loop mirror to provide wavelength selective feedback, and a tunable coupler to direct part of the light to the output port of the laser. The output of the laser is available via a fiber that is butt-coupled to the output port. (b) Photo of the assembled hybrid laser, on top of a one Euro coin. The left part is the dielectric feedback chip with the heaters for thermal tuning, and the right part is the semiconductor amplifier chip on top of a submount.

in integrated lasers, when there is no way of tuning the cavity length mechanically.

3.2   Hybrid integrated extended cavity laser

For an experimental demonstration, we use a hybrid integrated InP diode laser as shown in Fig. 3.2(a), with a waveguide circuit design similar to [53, 132, 97, 133, 134, 8, 55, 106]. For single-frequency operation, wide wavelength tuning, and for narrow linewidth oscillation through cavity length extension, we use a low-loss Si_3N_4 waveguide circuit, which provides frequency-selective feedback. Figure 3.2(b) shows the hybrid assembly on top of a one Euro coin to indicate its small size. Due to the presence of the microring resonators, the laser corresponds to laser 3 in Fig. 3.1(a).

The semiconductor chip [83] is fabricated by the Fraunhofer Heinrich Hertz Institute and contains a multi-quantum well active waveguide based on InP with a single-pass geometric length of 700 μm, an effective waveguide group index of 3.6, and a gain bandwidth of at least 120 nm around 1540 nm. One facet has a high reflectance coating of $\sim$ 90% against air, which forms one of the mirrors of the laser cavity. At the other facet, light is coupled to the dielectric chip, which forms the other feedback mirror. To reduce undesired reflections at the interface between the two chips, an anti-reflection coating is applied to the facet and the waveguide is tilted by 9° with respect to the facet normal.

The function of the dielectric chip is to provide frequency selective feedback and to increase the effective cavity length with very low loss. The feedback chip is based on a symmetric double-stripe waveguide geometry of two Si_3N_4 stripes buried in a SiO_2 cladding as described by Roeloffzen *et al* [100]. This single-mode waveguide has an effective waveguide group index of 1.72, exhibits a low propagation loss of about 0.1 dB/cm and enables small bending radii down to 100 μm. We fully exploit the

two-dimensional tapering capability of the Si_3N_4 platform for optimal matching of the optical mode to the mode of the gain chip and to the mode of the output optical fiber. At the facet for coupling with the InP gain chip, the waveguide is tapered two-dimensionally and angled down with 19.85° with respect to the facet normal to match the InP waveguide optical mode and angle at the interface. This mode and angle matching allows efficient coupling and reduces spurious reflections to a minimum.

A frequency selective filter is implemented on the feedback chip using two sequential race-track-shaped microring resonators, MRR_1 and MRR_2, in a Vernier configuration and placed inside a loop mirror (see Fig. 3.2(a)). The purpose of this filter is to impose single mode operation, tuning over the gain bandwidth and to increase the effective cavity length, which narrows the intrinsic linewidth [95]. The microrings have a circumference of 885.1 μm and 857.4 μm, respectively. These are the smallest lengths possible, based on the chosen implementation of racetrack resonators with adiabatic bends, the requirement of bend radii of at least 100 μm and the filter specifications. The total free-spectral range of the Vernier filter is 50.5 nm around the nominal wavelength. Although the bandwidth of the InP gain chip is larger, this free-spectral range is sufficient to obtain single mode lasing over a large part of the gain bandwidth. Both rings are symmetric and are designed for a power coupling coefficient to the bus waveguides of $\kappa^2 = 0.1$. We determined this value experimentally as $\kappa^2 = 0.071 \pm 0.003$, resulting in a length enhancement by a factor of 13.7 at resonance (*cf.* Eq. (3.7)). The length of the connecting bus waveguides and other elements adds up to 6.7 mm. By taking into account that both rings are passed once in every cavity roundtrip, the single pass effective optical cavity length is calculated as 3.5 cm.

Further, a so-called phase section of the bus waveguide is added to control the phase of the circulating light and to compensate phase changes when tuning any other element. Typically, the phase section is set to provide maximum feedback for a single longitudinal mode of the laser cavity, which restricts laser oscillation to a single wavelength and provides maximum output power. However, the phase section can also be tuned to provide equal feedback for two wavelengths and with this setting the laser can generate a multi-frequency comb [106].

A tunable coupler, implemented as a balanced Mach-Zehnder interferometer, is used to couple the circulating light out of the laser cavity. The extracted light is then directed to a single-mode polarization-maintaining output fiber. To prevent undesired external back reflections, the output fiber is terminated with an FC/APC connector and connected to a fiber isolator (Thorlabs IO-G-1550-APC).

Thermal tuning is implemented via resistive heaters placed above the rings, the phase section and the output coupler. The length of the phase section and output coupler heaters is 1 mm and both heaters require an electrical power of 290 mW to achieve a π phase shift and can induce a change in the optical phase of at least 2.5π. The slightly shorter heaters on top of the ring resonators require about 380 mW for π phase shift and were tuned up to 1.6π phase shift during the experiments.

The amplifier, feedback chip and output fiber were all aligned for optimum coupling and fixed permanently. This hybrid assembly was mounted on a thermoelectric cooler in a 14-pin butterfly package. The cooler, amplifier and heaters are wire-bonded
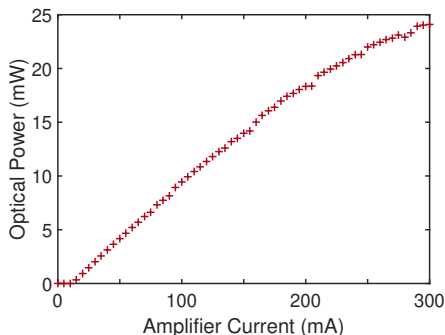
Figure 3.3: Measured fiber-coupled output power of the laser as function of the amplifier current. The thermoelectric cooler was set at 20 °C and the Vernier filter to a wavelength of 1576 nm.

to the pins and connected to external drivers. This assembly of the hybrid laser enables stable laser operation, which is a prerequisite for accurate and reproducible wavelength tuning.

During the measurements presented here, the laser was operated with the following parameters, unless otherwise specified. The temperature of the thermoelectric cooler was set at 25 °C. Although this temperature is slightly above the temperature for maximum performance, it keeps the diode just above ambient temperature to avoid condensation and it reduces the optical output power only with a few percent. Furthermore, the output coupler was set to 80% power outcoupling as this provides the best operating point for single-mode operation with high output power. Finally, after changing a laser parameter, the phase induced by the phase section was optimized for maximum output power, *e.g.*, to compensate for changes in the roundtrip phase when the pump current is changed [123].

3.3 Results

3.3.1 Basic laser properties

The fiber-coupled output power as a function of the pump current is shown in Fig. 3.3 with the Vernier filter set to a wavelength of 1576 nm and the temperature of the thermoelectric cooler to 20 °C, which are near optimum settings for this laser. A maximum of 24 mW was obtained at a pump current of 300 mA and the threshold current was 14 mA.

To illustrate the broad spectral coverage of the laser, we show in Fig. 3.4(a) superimposed laser spectra, as measured with an ANDO AQ6317 optical spectrum analyzer (OSA1), when the Vernier filter is tuned in steps of approximately 5 nm. The pump current was increased to its maximum of 300 mA in order to obtain the broadest spectral coverage. Figure 3.4(a) shows a spectral coverage of 120 nm, *i.e.*, extending the full gain bandwidth of the laser. The spectral coverage larger than
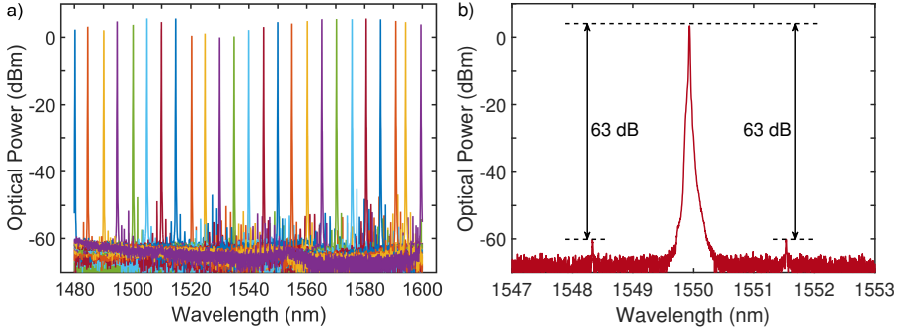
Figure 3.4: Superimposed laser spectra (a) showing the optical power in a 0.1 nm resolution bandwidth when the Vernier filter is tuned in steps of 5 nm, and measured laser power in a 0.01 nm resolution bandwidth (b), showing a high SMSR of 63 dB. The spectrum shown in (b) is an average over 10 measurements to reduce the background noise level and increase the visibility of the side modes. The amplifier current is set to 300 mA.

the Vernier free-spectral range ($\sim$ 50 nm) was obtained because the tunable output coupler, which becomes wavelength dependent for less than 100% outcoupling, was set to produce a higher loss at the undesired Vernier resonances, which was sufficient to prevent oscillation at these wavelengths. Optimum side mode suppression was found for a wavelength of 1550 nm. Figure 3.4(b) shows the optical power in a resolution bandwidth of 0.01 nm as a function of wavelength around 1550 nm, averaged over 10 measurements to bring the side modes above the noise level, again measured with OSA1. Note, Fig. 3.4(b) shows a higher side mode suppression ratio than shown in Fig. 3.4(a) where the laser settings were not optimized for highest side mode suppression. Figure 3.4(b) reveals two side modes with 63 dB suppression that are 1.61 nm away from the main mode, which agrees well with the first side peak of the Vernier filter. We used the high-resolution Finisar WaveAnalyzer 1500S optical spectrum analyzer (OSA2) to verify that only a single cavity mode was present. We expected to find the highest side-mode suppression for wavelengths around 1570 nm, where the output power is maximum. However, with the Vernier filter tuned to that wavelength, another mode at one Vernier free-spectral range away ($\sim$ 50 nm), builds up as well, lowering the side-mode suppression to 60 dB. When the laser is tuned to 1550 nm, modes at $\sim$ 50 nm distance are not detectable with OSA1, possibly because these modes are suppressed by lower gain or higher losses.

3.3.2   Intrinsic linewidth and mode-hop-free tuning

To demonstrate that the effective optical cavity length of 3.5 cm of the hybrid laser results in a high phase stability, we determined the intrinsic linewidth by measuring the power spectral density (PSD) of the frequency noise with a linewidth analyzer (HighFinesse LWA-1k 1550). This device was connected to the laser via the 10% port of a 90:10 fiber optic coupler. The remaining 90% was distributed over OSA1 and a photodiode. To obtain the lowest white noise level, we applied the maximum pump
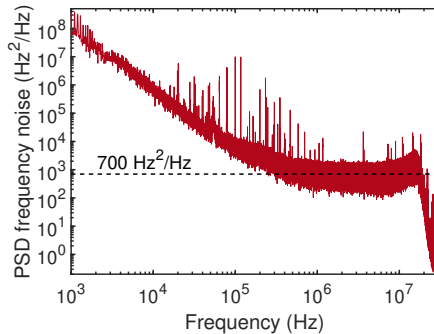
Figure 3.5: Single-sided power spectral density of the laser frequency noise, measured with a HighFinesse linewidth analyzer (maximum bandwidth 10 MHz). The dashed line at 700 Hz^2/Hz indicates the average noise for the noise frequency range between 1.3 and 3.5 MHz, excluding any spurious noise frequencies.

current of 300 mA from a battery-powered current source (ILX Lightwave LDX-3620) to the gain section. The laser wavelength was set to 1550 nm by the Vernier filter. Figure 3.5 shows the measured PSD of the laser frequency noise, as function of the noise frequency. The frequency noise shown in Fig. 3.5 has the characteristics of $1/f$-noise for noise frequencies below approximately 1 MHz and becomes white noise at higher frequencies. A dip of the noise signal can be seen beyond 10 MHz, but this is outside of the maximum bandwidth of the measurement device. The narrow peaks in the spectral power density that can be observed at specific noise frequencies originate likely from either electronic sources or RF-pickup in cables. The intrinsic linewidth is determined from the average white noise level, excluding spurious peaks, for noise frequencies between 1.3 and 3.5 MHz. Multiplying the single-sided PSD noise level of 700 ± 230 Hz^2/Hz with π results in an intrinsic linewidth of 2.2 ± 0.7 kHz. This value is 4.5 times smaller than the previously reported value of 10 kHz for a similar InP-Si_3N_4 hybrid laser based on Vernier filters comprising two microring resonators [8]. We attribute this improvement mainly to a 4.6 times higher factor of pump current above threshold current in our measurement.

To verify continuous tuning and the increased mod-hop-free tuning sensitivity of the hybrid laser (see Eq. (3.1)), we measured the laser wavelength and output power as a function of the electrical power applied to heater of the phase section with appropriate heater powers applied to the microring resonators (see Eq. (3.12)). For these measurements, the laser was connected via a fiber optic coupler to OSA2, in order to resolve the small step size in wavelength, and to a photodiode (Thorlabs S144C) to monitor the output power. To avoid the appearance of any competing modes during continuous tuning, the amplifier current was reduced to 70 mA. We note that the continuous tuning range does not depend on a specific amplifier current. For zero applied heater power to the phase section, we optimized the ring heaters to align the Vernier filter transmission with the lasing wavelength using minimum heater power. This resulted in an initial wavelength of 1534.25 nm and ensured having the full range of the phase section available for continuous tuning.
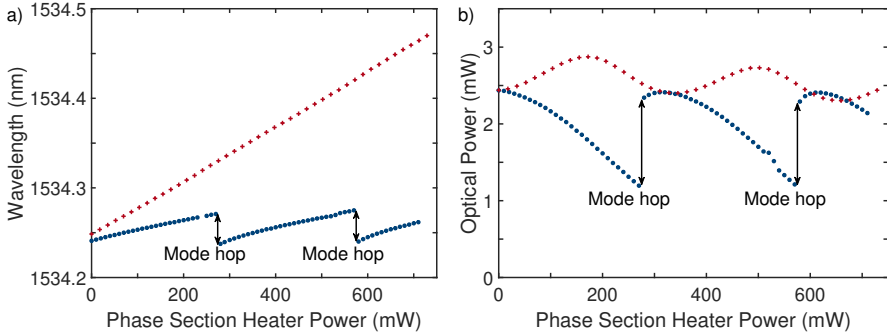
Figure 3.6: Measured laser wavelength (a) and output power (b) as function of the phase section heater power. Synchronous tuning of the phase section with the Vernier filter is shown by the red crosses, while tuning only the phase section is shown by the blue circles for comparison. Mode hops are indicated with arrows.

For continuous tuning, we experimentally determined the optimum tuning ratios for the phase section versus the ring resonators by maximizing the laser output power as $\partial\phi_1/\partial\phi_{\mathrm{ps}} = 0.107$ and $\partial\phi_2/\partial\phi_{\mathrm{ps}} = 0.103$ for ring resonators 1 and 2, respectively. This agrees well with the values given by Eq. (3.12) of 0.108 and 0.105, respectively, especially when considering the uncertainty in some of the laser parameters. Using these ratios, the heater power for the phase section was increased in steps corresponding to a change in lasing wavelength of 5 pm. The corresponding wavelength and output power are shown as red crosses in Figs. 3.6(a) and 3.6(b), respectively. For comparison, Fig. 3.6 also shows the same measurements when only the heater of the phase section is varied while the heaters for the microrings are kept constant (blue circles).

Figure 3.6(a) clearly shows that, when only the phase section is tuned, modes hops occur that limit the continuous tuning range to 0.034 nm, which is the free-spectral range of the laser cavity, corresponding to its optical cavity length of 3.5 cm. In this case, the optical cavity length used to calculate the free-spectral range needs to include the effective optical lengths of the microring resonators. Furthermore, the optical power varies strongly and discontinuously during the tuning (see Fig. 3.6(b)). The reason is that even a small detuning between the lasing wavelength and the fixed position of the sharp Vernier filter transmission peak leads to a strong change in the cavity losses and thus to a change in output power. Further tuning of the phase section, beyond integer multiples of π phase shift, leads to mode hops, which can be observed as discontinuities in the wavelength and output power of the laser.

On the other hand, when we tune the rings synchronously with the phase section, the mode hops are removed and tuning becomes continuous, as can be seen in Fig. 3.6 (red crosses). This shows that the lasing wavelength stays aligned with the resonant wavelength of the rings. It can be noted however from Fig. 3.6(b), that the alignment is not perfect, because the output power still shows a residual variation with a period that corresponds with the distance between mode hops.

The most apparent difference in Fig. 3.6(a) is that the tuning sensitivity $\partial\lambda_c/\partial\phi_{\mathrm{ps}}$

is indeed much larger for synchronous tuning compared to only tuning the phase section. We find that $\partial\lambda_c/\partial\phi_{\text{ps}} = 0.31$ pm/mW for synchronous tuning, while it is 0.11 pm/mW when only tuning the phase section. The tuning sensitivity of 0.31 pm/mW agrees well with the value of 0.29 pm/mW predicted by Eq. (3.1), given the uncertainty in some of the experimentally determined laser parameters. In addition, the synchronous tuning allows for a larger than π phase shift induced by the phase section without invoking a mode hop. These effects together result in a total mode-hop-free tuning range of 0.22 nm, which is a six-fold increase over the free-spectral range of the laser cavity and only limited limit by the available phase shift of the phase section. For comparison, we are not aware of any synchronous tuning in any hybrid integrated lasers. The examples we find are restricted to only tuning the phase section, where the tuning range remains a single FSR [55].

3.3.3 Acetylene absorption spectroscopy with mode-hop-free tuning

In demonstrating the continuous tuning of the hybrid laser, we have applied wavelength increments of 5 pm that can easily be resolved using OSA2. However, it should be possible to tune the lasing wavelength in much smaller steps. Current resolution of the electronics used to power the heaters allows mode-hop-free laser wavelength tuning in steps below 0.1 pm, well beyond that what can be resolved by the available optical spectrum analyzers. We demonstrate this small step size by recording the shape of an acetylene absorption line in high resolution. Acetylene ($^{12}\text{C}_2\text{H}_2$) is chosen because it has several well-known sharp absorption lines in the wavelength range of interest, which can be modelled with high accuracy [135, 136]. For this experiment, we choose the P19 ro-vibrational absorption line of acetylene with a center wavelength of 1536.713 nm.

To measure the acetylene absorption line shape, we divided the laser output equally by a fiber optic coupler over two outputs. One part was sent through an absorption cell to a first photodiode (PD1, Thorlabs S144C), while the other part was split again and divided over a second photodiode of the same model (PD2) and OSA1 for calibration of the laser wavelength. The absorption cell is a standard sealed fiber-coupled acetylene gas cell from Wavelength Reference Inc., with a 5.5 cm path length and 50 ± 5 Torr pressure at 295 K temperature.

The normalized transmission through the absorption cell was determined by dividing the signal of PD1 by the signal of PD2 to compensate for any changes in output power of the laser and then normalize it to the maximum transmission measured in the total tuning range of ~ 0.23 nm. Using the total tuning range, OSA1 was used to calibrate the increment in wavelength of the laser as 0.12 pm per 0.37 mW heater power applied to the phase section. However, the resolution of the OSA was insufficient to determine an accurate starting wavelength. This starting wavelength was calibrated by having the center wavelength of the measured P19 absorption line coincide with the value obtained from the calculated transmission. The required offset of -1.8 pm applied to the wavelength of the laser falls well within the resolution of OSA1.
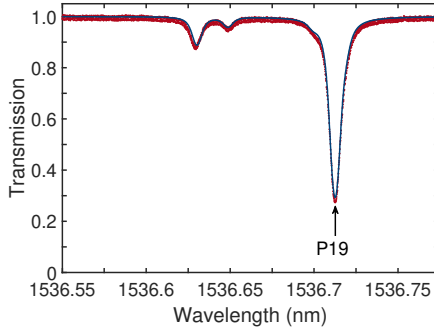
Figure 3.7: Measured (red dots) and calculated (blue line) transmission through an acetylene gas cell as function of wavelength for absorption line P19 at 1536.713 nm.

Figure 3.7 shows the measured normalized transmission through the gas cell as function of the calibrated wavelength of the laser (red dots). The calculated transmission, as obtained by a HITRAN-based simulation [135] for the specified absorption cell length, pressure and temperature, is shown as a blue line. We observe in Fig. 3.7 an overall good match between the measured and calculated transmission. The slightly broader measured transmission can be explained by the uncertainty in gas cell pressure. By recording the P19 acetylene absorption line and comparing it with an accurately calculated spectrum, we show that, once calibrated, the hybrid extended cavity laser can be accurately tuned to any wavelength within the continuous tuning range of ~ 0.23 nm (~ 29 GHz) with a resolution as small as ~ 0.12 pm (~ 15 MHz), which is well below the resolution of both optical spectrum analyzers used.

3.4 Discussion and conclusions

We have presented a novel method for increasing the continuous tuning range of integrated single-frequency lasers with an ultra-narrow linewidth by increasing the tuning sensitivity F_λ. Ultra-narrow linewidth is provided by extending the cavity length with a multi-pass resonator-based filter, as schematically shown as laser 3 in Fig. 3.1(a). In our demonstration experiment, the filter consists of two tunable microring resonators that not only enable single-mode oscillation, but also contribute to the optical length of the laser with multiple passes of the light through the rings per roundtrip in the laser cavity. When only tuning the phase section, the laser behaves like laser 2 in Fig. 3.1(a) and a small tuning sensitivity is found, corresponding to the long external laser cavity. However, when the intracavity filter is synchronously tuned with the phase section, the tuning sensitivity is significantly increased, corresponding to that of an equivalent laser with a short cavity without the effective length of the filter, *i.e.* to laser 1 in Fig. 3.1(a).

We experimentally demonstrated the extended continuous tuning with a hybrid integrated semiconductor laser. The laser comprises a 700 μm long InP gain section,

while the effective optical cavity length is extended to 3.5 cm, using a low-loss Si_3N_4 waveguide circuit, which narrows the intrinsic linewidth to 2.2 kHz. The circuit comprises a phase section for continuous tuning and a highly frequency selective Vernier filter with two tunable microring resonators. When only tuning the phase section, the tuning range per phase shift, $\partial\lambda_c/\partial\phi_{ps}$ is only 10 pm/rad. If the Vernier filter frequency is synchronously tuned with the oscillation frequency of the laser, the tuning sensitivity is enhanced by a factor of 2.8, to 28 pm/rad.

The observed enhancement in tuning sensitivity agrees very well with the continuous tuning model we developed. This model shows that the enhanced tuning sensitivity relies on the sum of the optical length of the amplifier and the optical length of the bus waveguide. Since the tuning sensitivity is independent of the length of the microring resonators, this allows independent optimization of intrinsic phase stability and continuous tuning sensitivity. For further linewidth narrowing, the cavity length of a laser can be increased without a penalty in the range of continuous tuning, *e.g.*, by increasing the ring diameter, lowering the bus to ring waveguide coupling constants or by adding extra rings [45, 76]. The tuning sensitivity and hence the range of continuous tuning can be increased by shortening the length of bus waveguides not used as phase section. Alternatively, increasing the relative length of the bus waveguides used as phase section extends the continuous tuning range as well. For instance, the continuous tuning range of the laser investigated is limited by the maximum phase delivered by the phase section, since $\frac{\partial\phi_i}{\partial\phi_{ps}} \approx 0.1$ (*cf.* Eq. (3.12)), while the 1 mm long phase section heater and the ring heaters can provide an approximately equal phase shift. If the heaters were extended to cover all the 6.7 mm of connecting bus waveguides, this would increase the continuous tuning range by a factor of 6.7 to approximately 1.6 nm, while maintaining a 2.2-kHz linewidth. Once all bus waveguides are phase-tunable, a further increase of tuning range requires a more effective phase tuning material to be selected. Phase shifters that are more effective than the current 2.5π phase shift per mm length, *e.g.*, ITO-based electro-optical phase shifters that provide π phase shift over 32 μm length [137], would allow for laser designs with continuous tuning over a much larger range, *i.e,* up to 20 nm. Ultimately, the limit is the free-spectral range of the Vernier filter, in our case 50 nm.

An additional advantage of the synchronous phase-and-filter tuning is that it can mitigate technological limitations in laser wavelength tuning, wavelength modulation, or frequency locking to references. The reason is that the available phase shift of a tunable phase section in integrated photonic circuits is often limited by material constants, *e.g.*, the thermo-optic, strain-optic, or electro-optic coefficients of the involved materials. Our approach increases the tuning sensitivity F_λ, which means that less phase shift becomes sufficient for a given tuning range. This is an advantage in many respects, such as to reduce power consumption in thermal phase shifters and to increase the speed in laser tuning and frequency modulation, for facilitating, *e.g.*, spectroscopic and metrologic applications.

The option of faster modulation and frequency control is specifically important for stabilizing lasers to reference frequencies, for instance to absolute standards [124]. We experimentally demonstrated fine-tuning of the laser in steps of 0.12 pm over a full P19 ro-vibrational absorption line of acetylene. Because the recording revealed

the known line shape [136, 135] very accurately, we conclude that the laser can be continuously and linearly tuned with steps smaller than the resolution of the available optical spectrum analyzers. Furthermore, such tuning is essential for stabilization of hybrid integrated InP-Si$_3$N$_4$ lasers to an absolute reference.

We expect that the demonstrated tuning method based on resonant intracavity filtering can be applied to other types of lasers as well. Possible examples are photonic crystal lasers [138, 139], Bragg waveguides [140, 141], other gain materials [142, 143] or nonlinear gain. The expected advantages are linewidth narrowing without obstructing continuous tuning, increasing the tuning range without obstructing linewidth narrowing, and reduced power consumption or higher speed in continuous tuning or stabilization of single-frequency lasers.

Appendix - Mode-hop-free tuning

The hybrid laser produces maximum output power when each of the ring resonators has a resonant wavelength λ_i ($i = 1, 2$) that coincides with the lasing wavelength λ_c. Mode-hop-free tuning requires that the shift in each of the wavelengths is the same, i.e., $\delta\lambda_c = \delta\lambda_1 = \delta\lambda_2$. Tuning of the resonant wavelengths is realized via resistive heaters on top of the phase section and the microring resonators. Heating of the phase section changes only the lasing wavelength, while heating a microring resonator will concurrently change the resonant wavelength of the ring and the lasing wavelength. As we will demonstrate, it is the latter property that causes the mode-hop-free tuning sensitivity, $\frac{\partial\lambda_c}{\phi_{\text{ps}}}$, of this hybrid laser with resonantly enhanced optical cavity length to be larger than that of a standard semiconductor Fabry-Pérot laser of equivalent optical length.

In order to model the action of the heaters, we assume that their sole action is to add a phase, ϕ_j, to the light propagating through the waveguide section j below the heating element. As the free-spectral range of a resonator is defined as an increase in roundtrip phase of the light with 2π it is intuitive and straightforward to show that the change in resonant wavelength, λ_i, for microring resonator, i, with phase added by the heater on top of the ring, ϕ_i, is given by

$$\frac{\partial\lambda_i}{\partial\phi_i} = \frac{\Delta\lambda_i}{2\pi}, \tag{3.2}$$

where $\Delta\lambda_i$ is the free-spectral range of ring i. This free-spectral range is given by [99]

$$\Delta\lambda_i(\lambda) = \frac{\lambda^2}{n_{g,i}(\lambda)L_i}, \tag{3.3}$$

where λ is the wavelength in vacuum, $n_{g,i}$ is the effective group index of the Si$_3$N$_4$ ring waveguide and L_i is the circumference of the ring resonator. In a similar way, the change of lasing wavelength, λ_c, with phase added by the phase section, ϕ_{ps}, is given by

$$\frac{\partial\lambda_c}{\partial\phi_{\text{ps}}} = \frac{\Delta\lambda_c}{\pi}, \tag{3.4}$$

as the light passes through the phase section twice per roundtrip. In Eq. (3.4), $\Delta\lambda_c$ is the free-spectral range of the laser cavity given by

$$\Delta\lambda_c(\lambda) = \frac{\lambda^2}{2n_{g,a}(\lambda)L_a + 2n_{g,b}(\lambda)L_b + \sum_i n_{g,i}(\lambda)L_{e,i}(\lambda)}, \tag{3.5}$$

where $n_{g,j}$ is the effective group velocity of the light in the semiconductor waveguide ($j = a$), the Si_3N_4 bus waveguide ($j = b$) or the Si_3N_4 rings ($j = i$), L_j is the geometric length of section a or b and $L_{e,i}$ is the effective length of ring i given by [95]

$$L_{e,i}(\lambda) = -\frac{1}{2\pi}\frac{\lambda^2}{n_{g,i}(\lambda)}\frac{\partial\theta_i}{\partial\lambda}, \tag{3.6}$$

with θ_i the phase added to the light when it propagates through the ring from input to drop port. For a symmetric microring resonator at resonance, $L_{e,i}$ reduces to [95]

$$L_{e,i} = L_i\left(\frac{1}{2} + \frac{1 - \kappa^2}{\kappa^2}\right), \tag{3.7}$$

where κ^2 is the power coupling from the input waveguide to the ring and from the ring to the output waveguide. The effective length is equal to the geometric length $L_i/2$ from input to drop port to which a length is added, equal to the distance travelled by the light in the time it effectively remains within the ring, which corresponds to the maximum attainable effective length of the ring.

The laser wavelength is not only shifted by the phase induced by the phase section (Eq. (3.4)), but also by the phase induced by the heaters on top of the rings. At resonance, the total phase added to the light in the laser cavity by ring i is just $\phi_{c,i} = \frac{L_{e,i}}{L_i}\phi_i$, which results in a change in lasing wavelength of

$$\frac{\partial\lambda_{c,i}}{\partial\phi_i} = \frac{\Delta\lambda_c}{2\pi}\frac{L_{e,i}}{L_i}. \tag{3.8}$$

For the total change in lasing wavelength, $\delta\lambda_c$, we then have

$$\delta\lambda_c = \frac{\partial\lambda_c}{\partial\phi_{ps}}\delta\phi_{ps} + \sum_i \frac{\partial\lambda_{c,i}}{\partial\phi_i}\delta\phi_i. \tag{3.9}$$

The mode-hop-free condition $\delta\lambda_c = \delta\lambda_i$ requires that the phase added to the light in the rings is proportional to the phase added by the phase section. Using this and substituting Eqs. (3.2), (3.3), (3.4) and (3.8) in Eq. (3.9) gives

$$\delta\lambda_c = \frac{\Delta\lambda_c}{\pi}\delta\phi_{ps} + \sum_i n_{g,i}L_{e,i}\frac{\Delta\lambda_c}{\lambda_c^2}\delta\lambda_c. \tag{3.10}$$

Using Eq. (3.5) in Eq. (3.10) gives the mode-hop-free change in lasing wavelength with phase induced by the phase section, which we have introduced as the tuning sensitivity F_λ in the main text, as

$$F_\lambda \equiv \frac{\partial\lambda_c}{\partial\phi_{ps}} = \frac{1}{\pi}\frac{\lambda_c^2}{2n_{g,a}L_a + 2n_{g,b}L_b}. \tag{3.11}$$

Equation (3.11) shows our central finding, namely the increased tuning sensitivity for synchronous tuning of the phase section with the microring resonators. In essence, the synchronous tuning of the ring resonances with the phase section removes the contribution of the effective ring lengths to the cavity length, which helps to expand the tuning range. Equation (3.11) shows indeed that the mode-hop-free tuning sensitivity does not include the effective length of the microring resonators that are part of the laser cavity, and the tuning sensitivity corresponds to that of a laser with a short cavity length.

To satisfy the mode-hop-free tuning condition, the phase added by the ring resonator heaters must be set with a fixed ratio to the phase added by phase section heater. Using Eqs. (3.2), (3.3) and (3.11) gives this ratio as

$$\frac{\partial \phi_i}{\partial \phi_{\text{ps}}} = \frac{n_{g,i} L_i}{n_{g,a} L_a + n_{g,b} L_b}.$$ (3.12)

Equation (3.12) provides the phase tuning ratio, which needs to be fulfilled to achieve the tuning sensitivity given in Eq. (3.11). The fulfillment can be limited for technological reasons, *e.g.*, as the right-hand-side of Eq. (3.12) is typically less than 1 for most laser designs, the phase added by the ring resonator heaters is usually less than that by the phase section heater. Consequently, the total continuous tuning range is often limited by the phase section heater.

Chapter 4

A hybrid-integrated diode laser in the visible spectral range

Generating visible light with wide tunability and high coherence based on photonic integrated circuits is of high interest for applications in biophotonics, precision metrology and quantum technology. Here we present the first demonstration of a hybrid-integrated diode laser in the visible spectral range. Using an AlGaInP optical amplifier coupled to a low-loss Si_3N_4 feedback circuit based on microring resonators, we obtain a spectral coverage of 10.8 nm around 684.4 nm wavelength with up to 4.8 mW output power. The measured intrinsic linewidth is 2.3 ± 0.2 kHz. [1]

4.1 Introduction

Integration of diode amplifiers in low-loss passive photonic platforms enables highly coherent light sources in the infrared range [45], where the integrated chip-sized format provides superior stability, portability and scalability for optical systems. Extending photonic integration into the visible has begun [79, 80] due to its high potential specifically for applications in biophotonics, metrology and quantum technology. Various optical systems for operation with visible coherent light have already been integrated using the Si_3N_4 platform [79, 80], such as for microscopy [144], neurophotonic probing [29], fluorescence biosensing [145] or trapping of ions [41]. Nevertheless, all photonic integrated systems in the visible have so far required external laser sources for their operation, which is due to the lack of hybrid-integrated lasers in this spectral range.

Integrating visible, widely tunable and narrowband lasers would provide several important benefits. Having the laser integrated on chip removes the instability associated with coupling light into photonic circuits. Using low-loss and spectrally-selective feedback circuits as integrated extended cavity enhances the laser's spectral stability by narrowing the Schawlow-Townes linewidth on chip [2, 88]. These advantages carry over to, *e.g.*, refractive index biosensors, which require stable lasers in the visible [28]. Biosensors based on optical resonance techniques particularly benefit from a narrow linewidth source, because this enhances the spectral resolution of the sensor, and, hence, lowers the detection limit [146]. Similarly, on-chip operation of multiple-wavelength, highly-coherent visible lasers is important for all-integrated optical cooling and trapping [42] for portable optical clocks [16] or for quantum information processing [41].

In the infrared range, integration of semiconductor amplifiers with spectrally-selective feedback circuits has made various kinds of widely tunable lasers available that can be seamlessly integrated into photonic integrated circuits. These hybrid and heterogeneously integrated diode lasers have been demonstrated at 2.6 μm [58], 1.65 μm [57], 1.55 μm [88, 45], 1.27 μm [62], 1.06 μm [61], 1.0 μm [64] and at 0.85 μm [63]. For reaching into the blue spectral range, an InGaN-based laser had been epitaxially grown on a Si wafer [147], however, the integration into a photonic circuit has not been demonstrated yet. To avoid two-photon absorption for high photon energies in the visible, photonic circuits require dielectric waveguides with a high band gap, *e.g.*, based on TiO_2 or Si_3N_4. In addition, suitable waveguides with reduced scattering loss are required, as scattering due to roughness of the core-to-cladding interface strongly increases towards shorter wavelengths ($\sim 1/\lambda^3$) [148]. Heterogeneous integration, using vertical tapers for evanescent coupling between an InGaN laser and passive TiO_2 waveguides, was investigated, but successful bonding would require reduced surface roughness [149]. To date, no successful realization of a hybrid or heterogeneously integrated diode laser for the visible spectral range has been reported.

In this work we demonstrate the first operation of a hybrid-integrated diode laser in the visible. Using Si_3N_4 waveguides, we provide a feedback circuit with negligible absorption loss and low scattering loss via a weakly confined optical mode. This hybrid
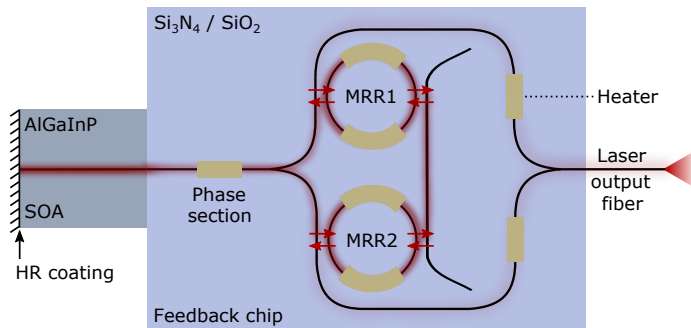

Figure 4.1: Schematic overview of the hybrid laser comprising an AlGaInP optical amplifier butt-coupled to a Si_3N_4/SiO_2 feedback chip. The chip contains two sequential microring resonators (MRR1, MRR2) that form a Vernier filter within a loop mirror. Directional couplers are indicated by red arrows. Heaters (yellow) are placed on the MRRs, on the intracavity phase section and near the output Y-junction.

integration enables on-chip narrow-linewidth lasers in the visible spectral range.

4.2 Laser design and hybrid integration

The design of the hybrid laser is shown schematically in Fig. 4.1. The laser cavity is formed by a semiconductor chip coupled to a Si_3N_4/SiO_2 based feedback chip. The multiple quantum well AlGaInP semiconductor optical amplifier (SOA, Sacher SAL-0690-25) is 600 μm long and provides a gain bandwidth of approximately 10 nm around 685 nm, with up to 25 mW output power in Littrow configuration. Its back facet has a high reflectivity (HR) coating of 95%, which forms one mirror of the laser cavity. The other mirror is a reflective Vernier filter formed by a y-junction and two cascaded microring resonators (MRRs) to provide highly frequency-selective feedback.

To minimize propagation losses and to support only single-mode propagation, the feedback circuit is implemented using a high aspect ratio Si_3N_4 core that is 2 μm wide and 25 nm thick. This core is centered in a 16 μm thick SiO_2 cladding to guide the TE_{00} mode [100, 80]. The smallest bending radius for this waveguide geometry is chosen as 1200 μm to ensure that bend radiation loss is small compared to the straight propagation loss. Key to low propagation loss is the small height of the sidewalls to minimize the scattering loss, as the sidewall etching produces a larger interface roughness than the layer deposition process, which defines the top and bottom surface of the waveguide. To characterize the straight-waveguide propagation loss, we measured the light transmission through 1-cm and 4-cm long straight waveguides and 58-cm long low-curvature spirals. The measured propagation loss is 0.07±0.02 dB/cm at the wavelength of 685 nm. To obtain the overall propagation loss of the rings, we scanned a tunable laser across several ring resonances. This resonator loss is 0.13±0.02 dB/cm, based on fitting the calculated ring responses to the measured transmission. The excess resonator loss is probably due to bending loss and parasitic

loss in the symmetric coupler section [150]. In order to optimize the mode matching with a single-mode, polarization-maintaining output fiber (Nufern PM460-HP), the waveguide width is tapered down to 0.8 μm at the fiber side to obtain a simulated coupling efficiency of 85%. The waveguide is not tapered at the gain side, as calculations predicted a comparably high overlap of 89% with the estimated mode of the SOA (MFD$_{hor}$ = 3.6 μm, MFD$_{vert}$ = 1.5 μm).

The functionality of the feedback circuit is twofold. Frequency filtering is realized using two high-quality MRRs with slightly different radii. These rings have radii of 1200 and 1205 μm and an estimated loaded Q-factor of $9.5 \cdot 10^5$. The measured Vernier free spectral range (FSR) is 9.90±0.05 nm at the nominal wavelength of 685 nm [88]. This FSR is approximately equal to the gain bandwidth of the SOA, to avoid multiple wavelength oscillation. The second function is to lower the intrinsic laser linewidth with a long effective length of the feedback circuit. At resonance, the effective length of each ring is enhanced by a factor of 18 to 14 cm, which is calculated by the group delay [95], using the ring radius, the measured resonator loss and the power coupling between bus waveguide and ring. This power coupling $\kappa^2 = 0.043 \pm 0.011$ is measured using a separate directional coupler, identical to the ones in the rings.

Summing the optical lengths of all elements gives a maximum effective roundtrip length of 49 cm for the laser cavity. As the length of the laser cavity is strongly frequency-dependent [95], the cavity modes are non-equidistant with a calculated minimum mode spacing of 1.0 pm (0.67 GHz). Single longitudinal mode oscillation is expected, because this mode spacing is larger than the calculated 0.46 pm (0.30 GHz) full-width-at-half-maximum (FWHM) of the Vernier resonance.

Thermo-optic phase tuning of the feedback circuit is realised via chromium-based resistive heaters [100]. Tuning the ring heaters is used for wavelength selection, while tuning the intracavity phase section is used to align a cavity resonance with the ring resonances. The light extracted from the cavity is combined using a Y-junction before coupling it into the output fiber. To balance the phase in both extraction paths with minimal thermal tuning for maximum output coupling, one of both heaters placed near this Y-junction can be tuned. Introducing a phase shift of 2π with the resistive heaters requires approximately 400 mW of dissipated electrical power.

To enable stable laser operation via hybrid integration, the amplifier, feedback chip and output fiber were all aligned for optimum coupling and bonded with an adhesive. The SOA and heaters were wire bonded to an adapter board for electrical connections. The SOA pump current and heater currents were supplied with a Thorlabs LDC205B current source and a Nicslab XPOW-8AX-CCvCV multi-channel power controller, respectively. To remove the generated heat, the hybrid assembly was placed on a common subcarrier with a heat sink, which was temperature-controlled using an adequately dimensioned Peltier element. For all measurements, the temperature was set at 20 ° C.
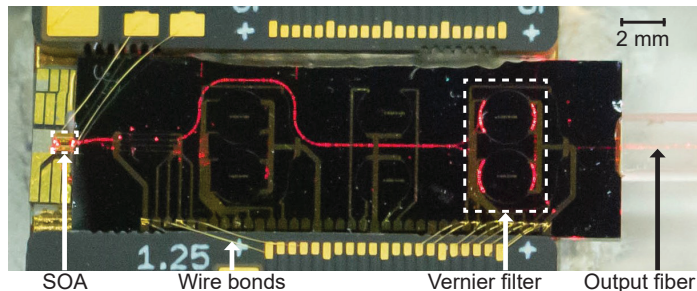
Figure 4.2: Photograph of the hybrid laser pumped at 90 mA. Bright scattered light from both rings indicates that a cavity mode is tuned to be aligned with both ring resonances. This light is partly blocked by heaters on top of the rings.

4.3   Experimental results

When pumping the SOA above treshold, scattered red light from the feedback chip can be observed. Figure 4.2 shows a photograph of the assembled laser when pumped at the maximum allowed pump current of 90 mA. This photo demonstrates the first operation of a hybrid-integrated diode laser in the visible spectral range. We tuned the phase section to align a cavity resonance with a Vernier resonance of the two rings, which is confirmed by the bright scattered light from both rings.

To measure the laser output power and spectral characteristics, the laser was connected via a fiber coupler (Thorlabs TW670R5A2) to a power sensor and an optical spectrum analyzer (OSA, ANDO AQ6317). Figure 4.3(a) shows the measured fiber-coupled output power as function of pump current, corrected for the 50:50 splitting ratio of the fiber coupler. For each measurement, the heater on the phase section was optimized for maximum output power, while other heaters were not activated. Figure 4.3(a) indicates a threshold current of 46 mA. Above threshold, the output power increases approximately linearly with a slope efficiency of 0.11 mW/mA, indicated with the linear fit line through all points except the four low outliers. These outliers were likely caused by spectral mode hops, since current-induced refractive index changes of the SOA caused the laser to hop to modes that were less efficiently coupled out. We measured a maximum output power of 4.8 mW at the maximum specified current of 90 mA. For this setting, we also measured the laser's output spectrum with the OSA using a 0.01 nm resolution bandwidth (RBW). This spectrum, as shown in Fig. 4.3(b), reveals a resolution-limited single-wavelength peak at 683.9 nm with a high signal-to-noise ratio of 40 dB. As the resolution bandwidth of the OSA is insufficient to distinguish adjacent cavity modes, additional measurements are described below to confirm single-mode oscillation.

To determine the spectral coverage of the laser, we varied the electrical power to the heater on MRR1. This shifts the resonant frequency of the underlying ring, thereby changing the Vernier feedback frequency. Fig. 4.4(a) shows several super-imposed laser spectra as measured with the OSA. The pump current was reduced to 50 mA to record the spectral coverage already obtainable with a few mA above
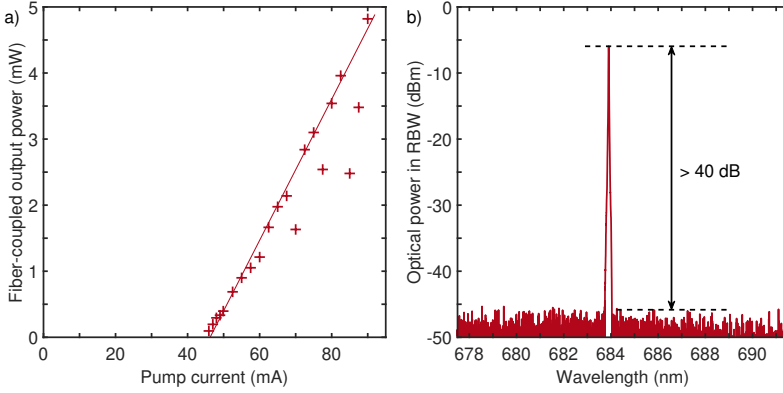
Figure 4.3: a) Fiber-coupled output power versus pump current, with optimization of the phase section heater. b) Optical power spectrum measured for a pump current of 90 mA.
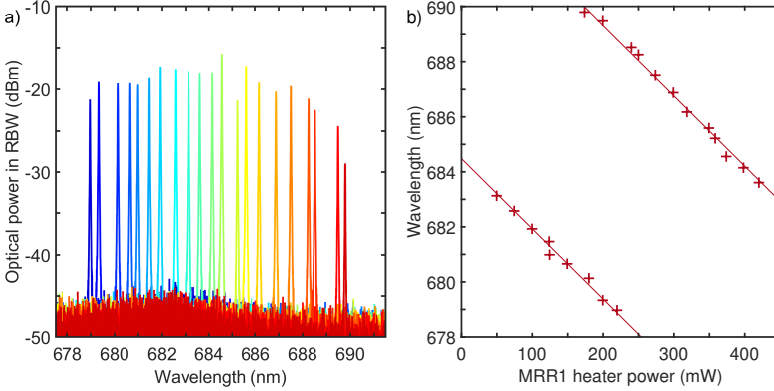
Figure 4.4: a) Superimposed laser spectra, as measured with an OSA set to 0.01 nm resolution bandwidth and obtained by varying the heater power to MRR1. The pump current was set to 50 mA. b) Peak laser wavelength extracted from the laser spectra in a) as function of heater power.

threshold. The phase section and a heater near the output Y-junction were coarsely optimized for each measurement to obtain single-wavelength laser emission with optimum output power. We observe that the laser wavelength can be tuned, in discrete steps, over a range of 10.8 nm around 684.4 nm, which covers the entire gain bandwidth of the amplifier. The highest output power was measured near the peak of the gain spectrum, as expected. Further variation in power can be explained by the nonuniform gain spectrum and by nonoptimal heater settings, since the outcoupling ratio strongly depends on the fine-tuning of the ring resonances. For a better qualification of laser tuning, Fig. 4.4(b) shows the extracted peak wavelengths as function of the heater power at MRR1. The laser wavelength decreases approximately linearly with increasing heater power, except for large hops when the laser is operated near

Figure 4.5: Optical spectrum (a) and RF spectrum (b) of the laser output with the laser optimized for single longitudinal mode oscillation. The pump current was set to 90 mA.

the edge of the gain bandwidth. We fitted two parallel lines through the data points to retrieve the hop distance. The wavelength spacing between these lines is 9.9 nm, which agrees well with the separately measured FSR of the solitary Vernier filter.

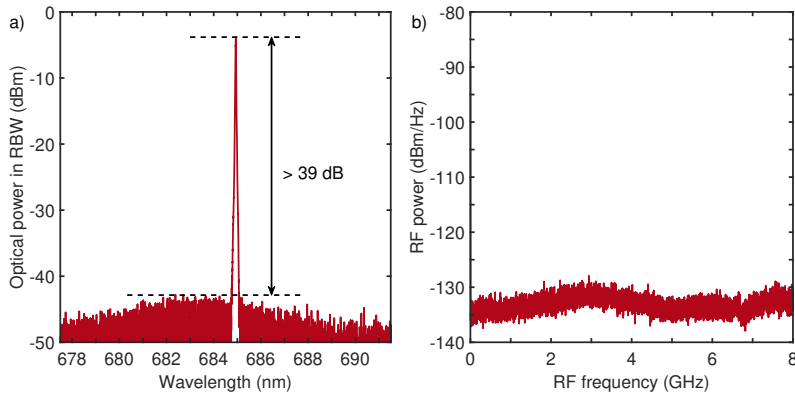To verify that optimized heater settings provide oscillation in a single longitudinal mode, *i.e.*, to spectrally resolve also adjacent longitudinal modes, we used a setup to detect the beating of laser modes in the radio frequency (RF) domain. For this purpose, the laser output was sent through an isolator (Thorlabs IO-F-690APC) directly to the OSA and directly to a fast photodiode (Thorlabs DXM12CF) connected to an RF spectrum analyzer (RFSA, Agilent E4405B). The RFSA was set to a resolution bandwidth of 1 MHz, and swept over a range up to 8 GHz, which would be sufficient to detect the beating between multiple longitudinal modes within a single Vernier resonance. We emphasize that the RF range is wider than the 0.01 nm (6 GHz) resolution bandwidth of the OSA, which ensures that multiple mode oscillations would be noticed. Figure 4.5 shows an example of the recorded (a) optical and (b) RF spectra, when the laser was optimized for single longitudinal mode oscillation. This optical spectrum shows a single wavelength, while corresponding RF spectra, recorded before and after this OSA measurement, show no indication of the presence of any beat frequencies. We note that several beat frequencies showed up in the RF spectrum with non-optimized settings of the laser. The RF and optical spectra combined let us conclude that, with proper settings, the laser oscillates in a single longitudinal mode with a side mode suppression ratio of at least 39 dB.

To determine the intrinsic linewidth of the laser, the output was sent through an isolator to a delayed self-heterodyne detection setup. The setup uses a fiber-based Mach-Zehnder interferometer, where one arm contains a 200 MHz acousto-optic modulator, while the other arm contains a 1-km long single-mode fiber as a delay (Thorlabs SM600), limited in length because of 6 dB/km propagation loss. The beat signal was recorded using the fast photodiode connected to the RFSA, set to a radio and video bandwidth of 10 kHz, and averaged over 50 sweeps. Fig. 4.6 shows the measured power spectrum as the blue trace. To reduce current noise for this measurement,
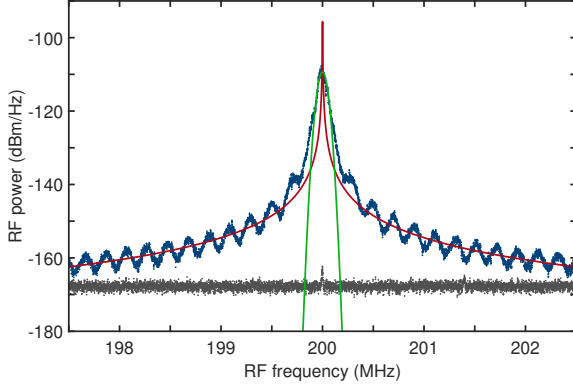
Figure 4.6: Recorded beat signal (blue trace) and background (grey trace) from the delayed self-heterodyne measurement setup, together with a fitted Gaussian profile (green curve) and a fitted Lorentz profile (red curve).

the pump current was supplied by a battery-operated current source (ILX Lightwave LDX-3620), set to 90 mA. We tuned MRR2 to set the laser's wavelength near maximum gain at 685.6 nm and fine-tuned the phase section to minimize the intrinsic linewidth. The recorded RF signal is well above the noise floor of the setup, displayed as the grey trace. In the blue trace, periodic modulations of approximately 200 kHz can be observed, consistent with the 1-km fiber delay and an even longer coherence length of the laser [151]. By fitting this trace to a Gaussian profile, as shown with the green curve, we find that the central peak has a predominantly Gaussian line shape with a FWHM of 56.3±0.4 kHz. This line shape of the free-running laser, which is associated with $1/f$ frequency noise [152] caused by technical noise sources, can be narrowed by locking the laser frequency to a high-finesse cavity or a Sr transition [42]. To estimate the intrinsic linewidth, which arises from white frequency noise, we fit the wings of the recorded signal to a Lorentz function, as shown with the red curve. The fitted Lorentzian linewidth is 2.3±0.2 kHz, which confirms that the laser has a very narrow intrinsic linewidth.

4.4   Conclusion

To conclude, we demonstrate the realization of the first hybrid-integrated diode laser in the visible spectral range. The maximum output power is 4.8 mW for a pump current of 90 mA and the spectral coverage amounts to 10.8 nm around 684.4 nm. The hybrid integration of an AlGaInP optical amplifier with a Si_3N_4 feedback chip, used for sharp Vernier filtering with high-quality microring resonators, enables single longitudinal mode laser oscillation. The long effective optical cavity roundtrip length of up to 49 cm provides a narrow intrinsic linewidth of down to 2.3±0.2 kHz. Improving the laser design, *e.g.*, by increasing the core thickness, would enable a smaller bend radius and a thinner top cladding for more efficient heaters. Second, adding an intracavity

tunable coupler for the extraction of the output power independent from the frequency filtering [88], would improve the overall performance of the laser, including more spectrally uniform and higher output power and lower intrinsic linewidth. The concept of hybrid-integrated diode lasers with very small intrinsic linewidth could possibly cover the whole visible spectral range. Realization of a fully integrated multi-color visible laser engine [153] would then become feasible for numerous applications.

56

Chapter 5

Long-term absolute frequency stabilization of a hybrid-integrated InP-Si3N4 diode laser

Hybrid integrated diode lasers based on combining semiconductor optical amplifiers with low-loss Si_3N_4-based feedback circuits enable great laser performance for advanced photonic circuits. In particular, using high-Q Si_3N_4 ring resonators for frequency-selective feedback provides wide spectral coverage, mode-hop free tuning, and high frequency stability on short timescales, showing as ultra-narrow intrinsic linewidths. However, many applications also require long-term stability, which can be provided by locking the laser frequency to a suitable reference. We present the stabilization of a hybrid-integrated laser, which is widely tunable around the central wavelength of 1550 nm, to a fiber-based optical frequency discriminator (OFD) and to an acetylene absorption line. By locking the laser to the OFD, the laser's fractional frequency stability is improved down to $1.5 \cdot 10^{-12}$ over an averaging time of 0.5 ms. For absolute stability over longer times of several days, we successfully lock the laser frequency to an acetylene absorption line. This limits the frequency deviations of the laser to a range of less than 12 MHz over 5 days. [1]

5.1   Introduction

Chip-integrated and frequency-stable diode lasers tunable to various wavelengths in the infrared or visible range are central for a wide range of applications, such as scalable quantum technology [40, 41, 43], integrated optical atomic clocks [17], signal processing [13, 33] and data transmission [8, 9, 11]. A high short-term stability, also expressed as a low intrinsic linewidth, can routinely be achieved with diode lasers in a chip-integrated format, by extending the cavity length with a low-loss waveguide feedback circuit [50, 76, 88, 45]. An alternative is using laser-external high-Q resonators for line-narrowing at the predefined frequencies of standard Fabry-Perot, DFB and DBR diode lasers through self-injection locking [46, 49, 73, 70]. To also achieve high long-term frequency stability, active stabilization to highly stable frequency references is required.

When considering bulk lasers, gas lasers such as helium-neon lasers are traditionally well-suited for long-term stability, allowing frequency stabilization with drifts of only around $2 \cdot 10^{-8}$ over several months [154, 155]. More recently, enormous progress has been achieved with frequency stabilization of diode lasers, enabling similar performance [156, 157, 158]. Furthermore, the lowest fractional frequency instabilities have been achieved using state-of-the-art bulk extended cavity diode lasers (ECDLs) [159] and fiber lasers [160]. Notably, a stability of $4 \cdot 10^{-17}$ up to 10 s was reached by stabilizing a fiber laser to an ultra-stable Fabry-Perot cavity [160]. On the other hand, a waveguide-based diode laser has recently exceeded the short-term frequency stability of high-performance fiber lasers, due to feedback from an ultra-high-Q integrated resonator [49]. Such chip-sized lasers enable seamless integration into mass-produced photonic circuits. Long-term active stabilization of these integrated diode lasers would be key for repeatability and reliability for a wide range of photonic applications.

To enable long-term stability over multiple hours or even longer, integrated diode lasers require additional properties. First, the laser should not make any mode hops in the required time frame, as they are challenging to correct for by electronic stabilization. While operation with individual chips aligned on stages is sufficient for investigating the short-term stability [46, 49], temperature drifts or acoustic perturbations are prone to cause mode-hops in such a configuration. To avoid this, the passive stability of the entire waveguide circuit needs to be improved through integration of the feedback chip with the diode laser. Second, to provide electronic feedback for stabilization, the laser must have a wavelength tuning mechanism with sufficient bandwidth and range. For also accessing any target wavelength within the laser's gain bandwidth, specifically single lines of absolute reference absorbers [161, 162, 158], a suitable diode laser concept has to be chosen. Diode lasers that use feedback from Bragg waveguides for spectral selection [140, 163, 47] offer only very limited tunability. Lasers where frequency noise reduction is based on self-injection locking from microring resonators [46, 49, 73, 70] offer wider tuning, however, this linewidth narrowing method requires careful adjustment of the feedback phase for constructive interference inside the laser cavity [70]. On the other hand, diode lasers employing Vernier-filter based extended cavities provide wide tuning over the entire gain bandwidth [51] and enable wide mode-hop free tuning over absorption lines [98].

Active stabilization of such a widely-tunable laser based on semiconductor integrated photonics has recently been demonstrated with a best frequency stability of $2.5 \cdot 10^{-13}$ at 1 s integration time [164]. An even better frequency instability of 10^{-14} below 1 s was achieved with a heterogeneously integrated DBR-laser, self-injection locked to a spiral resonator, and actively stabilized to a lithographically fabricated Fabry-Perot cavity [47]. However, such stabilization schemes have only been demonstrated over intermediate time scales up to several minutes.

Here we demonstrate the absolute frequency stabilization of a hybrid-integrated, widely tunable diode laser over several days. The laser is formed by hybrid integration of an InP diode amplifier and a Si_3N_4 feedback circuit. For the free-running laser, we observe mode-hop free operation over several days, achieved by electronic, thermal and optical packaging of the laser in a standard diode laser housing. To access reference lines for long-term absolute stabilization, the laser is widely tunable using two microring resonators in Vernier configuration. Active stabilization of the laser frequency to the acetylene P11 absorption line at 1531 nm provides a best stability of $2.0 \cdot 10^{-10}$. This scheme enables the desired long-term stability, demonstrated by continuous frequency stabilization for over 5 days with a residual drift below 12 MHz. For completeness, we also present short-term stabilization of our laser. This is realized by locking to a fiber-based optical frequency discriminator (OFD), which provides a best relative frequency stability of $1.5 \cdot 10^{-12}$ over an averaging time of 0.5 ms.

5.2 Hybrid-integrated diode laser

5.2.1 Laser design

For the experiments, we use a narrow-linewidth hybrid-integrated tunable laser (Chilas CT3, similar to [98]) as schematically shown in Fig. 5.1(a). The laser comprises a semiconductor chip, which is hybrid-integrated with a waveguide-based feedback circuit [97]. The semiconductor chip contains an InP-based multi-quantum well optical amplifier, fabricated by the Fraunhofer Heinrich Hertz Institute. The feedback circuit is based on low-loss Si_3N_4 waveguides with a TriPleX asymmetric double-stripe cross section [100]. One mirror of the laser cavity is formed by a high-reflectivity (90%) coating on the back facet of the optical amplifier. The other mirror is a frequency-selective loop mirror, formed by two sequential microring resonators (MRRs) on the feedback circuit. The circumferences of these resonators are 787 μm and 806 μm for MRR1 and MRR2, respectively. According to the Vernier principle, this enables wavelength selection for single-frequency laser operation over 70.4 nm around the central wavelength of 1.55 μm.

In addition, these rings provide a low intrinsic linewidth by extending the effective cavity length with multiple passes through the MRRs. The power coupling coefficient to the rings is designed as $\kappa^2 = 0.05$, which increases the optical effective length on resonance [95] to 23 and 24 mm for MRR1 and MRR2, respectively. In total, the effective cavity roundtrip length is increased to approximately 7 cm when the cavity resonance and ring resonances are aligned. To couple light out of the cavity to the output port, an 80% directional coupler is part of the feedback circuit. The output
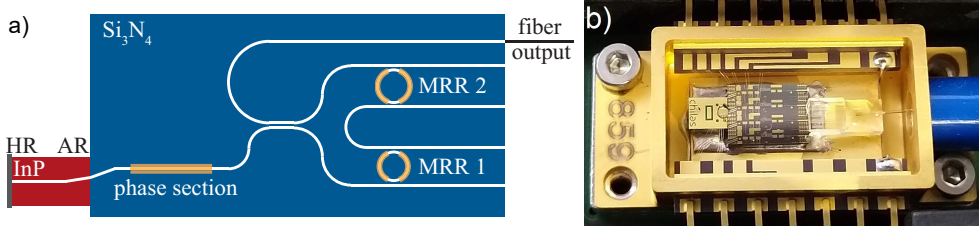
Figure 5.1: (a) Schematic view of the hybrid-integrated laser. The InP-based amplifier is coated with a high-reflection (HR) and an anti-reflection coating (AR). The Si$_3$N$_4$-based feedback chip contains two microring ring resonators (MRR). Heaters for thermal tuning are indicated in yellow. (b) Photograph of the hybrid laser assembly comprising the the amplifier, feedback chip and output fiber fixed together in a 14-pin butterfly package.

port is connected to a polarization-maintaining single-mode fiber, that is terminated with an FC/APC connector. Since extensive lengths of fibers may generate additional spectral broadening [165], the output and connected fibers are short, up to a few meters, such that fiber broadening can be safely neglected.

For thermal tuning, resistive heaters are located on top of the rings and a phase section. The phase section enables tuning a cavity resonance to align with a common resonance of the MRRs. All heaters can provide at least 2π phase shift by applying an electrical power of up to 1.0 W per heater.

For long-term optical path length stability, the laser is hybrid integrated. This is done by permanently edge-coupling the diode, feedback chip and output fiber by bonding the facets with transparent adhesive. The diode and feedback chip are placed on a thermoelectric cooler (TEC) element in a 14-pin butterfly package, shown in Fig. 5.1(b). The heaters and amplifier are wire bonded to separate pins. For computer controlled heater tuning and low-noise laser operation, we use the internal heater driver of a Chilas tunable laser controller and external TEC and laser diode drivers.

5.2.2 Laser characterization

We characterized the laser in terms of output power and wavelength tuning. For this purpose, we connected the laser via an optical isolator (Thorlabs IO-G-1550-APC) and a 90:10 fiber coupler to a photodiode power sensor (Thorlabs S144C) and an optical spectrum analyzer (OSA, ANDO AQ6317).

The fiber-coupled output power as function of the pump current and the corresponding amplifier voltages are plotted in Fig. 5.2(a). The plotted output power is corrected for the measured transmission loss through the isolator and fiber coupler. For exploring the maximum output power that can be generated with the laser, we provided a pump current of up to 500 mA using an external current source (ILX Lightwave LDX-3620). For all other measurements we do not exceed the maximum specified current for the laser of 300 mA. To obtain maximum output power and single-frequency operation, the phase section and rings were fine-tuned for each measurement. The Vernier filter and the TEC element were set to 1569.9 nm and 20 °C,
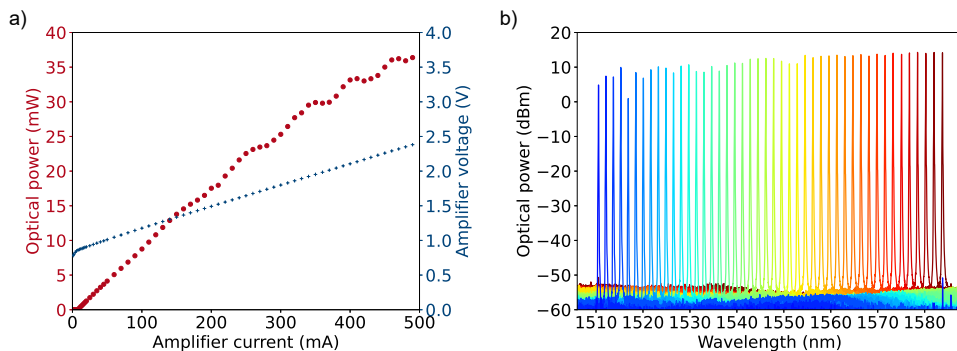
Figure 5.2: (a) Fiber-coupled output power (red dots) and amplifier voltage (blue crosses) versus amplifier current. The threshold current is 7.5 mA and the maximum measured fiber-coupled output power is 36.4 mW. (b) Superimposed laser spectra, as measured with an OSA set to 0.1 nm resolution bandwidth. The spectra are obtained by varying the heater power on MRR1 in steps of approximately 23 mW and then fine-tuning MRR1 and the phase section heater for maximum output power. The laser's wavelength coverage reaches from 1510.5 to 1583.8 nm. The side mode suppression ratio (SMSR) extracted from these spectra varies between 55 and 66 dB.

respectively. Figure 5.2(a) indicates a threshold current of 7.5 mA and a maximum measured fiber-coupled output power of 36.4 mW. Above threshold, the output power increases approximately linearly until power roll-off can be observed, which we address to local self-heating of the lasing region. The small oscillation in output power at high pump currents can be attributed to non-optimal settings of the heaters due to thermal and electrical crosstalk and the finite voltage step size of the heater driver.

To characterize the wavelength tuning of the laser, we varied the heater power on ring resonator MRR1 and measured the laser spectra with the OSA set to 0.1 nm resolution bandwidth. The diode pump current was set to the specified maximum of 300 mA for all measurements. The measured power level of the OSA was calibrated using a separate power meter. Figure 5.2(b) shows the superimposed spectra, when the heater power on MRR1 is changed in steps of approximately 23 mW and then fine-tuned together with the phase section for maximum output power. As a result, the laser wavelength changes in steps of about 1.7 nm, which corresponds to the free spectral range of the other ring resonator (MRR2). The wavelength coverage as shown in Fig. 5.2(b) spans from 1510.5 up to 1583.8 nm. This range of 73.3 nm agrees well with the calculated Vernier tuning range. The measured spectra display a high side mode suppression ratio (SMSR) between 61 and 66 dB throughout the tuning range of the laser, except for one outlier at the lower edge of the tuning range with a SMSR of 55 dB. We have also verified single-mode operation using a high-resolution OSA (Finisar 1500S, spectral resolution 180 MHz). The high SMSR confirms excellent single-mode operation over the full tuning range.

5.3 Frequency stabilization

For active frequency stabilization, laser frequency deviations from a set target have to be detected using a frequency discriminator. Next, a feedback loop is required to set the laser frequency back to its target value. To adjust the laser frequency, this laser offers multiple tuning mechanisms, which differ in tuning sensitivity and bandwidth. In an earlier measurement using a similar laser, we found that the bandwidth for thermal tuning by the phase section is limited to approximately 50 kHz, while tuning the diode laser frequency by the amplifier current provides a higher bandwidth of at least 0.33 MHz, which was limited by the equipment used for that measurement [166]. To reduce noise up to MHz Fourier frequencies, we apply a feedback signal to the amplifier current.

We investigate two different fiber-coupled frequency discriminators that can be conveniently coupled to the laser's fiber output. For stabilization on sub-second timescales, we use a commercial ultra-stable fiber-based frequency discriminator, which provides many closely spaced reference lines with a steep discriminator slope. The availability of many reference lines, that are much closer spaced than the laser's cavity modes, enables locking for any Vernier heater setting. An additional advantage of a fiber-based interferometer is that large path imbalances can be achieved to increase the frequency discriminator slope [167]. Maximizing this slope is important, since the highest achievable frequency stability is determined by the discriminator slope and its noise contribution, in the limit of large servo gain [168]. However, providing absolute stability is not possible, because long-term drift of the reference lines cannot be avoided completely, even with excellent thermal shielding.

To investigate long-term absolute frequency stabilization over multiple days, we use an acetylene absorption line as the second frequency reference. In this case, locking requires tuning the laser wavelength to a single, selected absorption line. The success of long-term stabilization critically depends on the absence of mode hops. Therefore, we also characterize the frequency stability of the free-running laser, and demonstrate mode-hop free operation over multiple days.

5.3.1 Sub-second frequency stabilization by locking to a fiber-based OFD

The setup to stabilize the laser frequency on sub-second time scale, using a fiber-based optical frequency discriminator (Silentsys OFD), is shown in Fig. 5.3. To show typical stabilization behavior, the laser current and TEC were set to 100 mA and 25 °C, respectively for these measurements. For optimum free-running operation, all heaters were turned off to remove any noise that might be added by the heater driver. The fiber-coupled laser output first passes an optical isolator and then a 90/10 fiber-optic coupler. 90% of the light is directed to a delayed self-heterodyne setup for analysis and 10% is directed to the OFD for stabilization. The OFD is an ultra-low noise optical frequency discriminator based on a fiber-interferometric process with a free spectral range of 2 MHz. To improve its thermal stability, the OFD is placed in a thermally insulated enclosure with active temperature control. The error signal
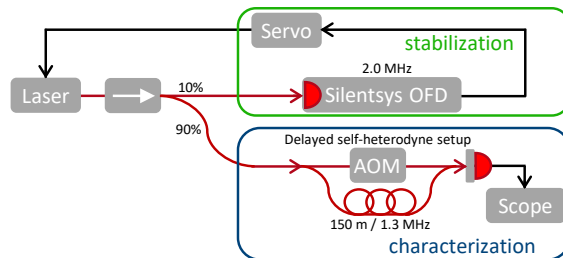
Figure 5.3: Frequency stabilization setup using a fiber-based optical frequency discriminator (OFD) and a setup for frequency noise characterization. The laser's output light first passes a fiber-optic isolator ($\rightarrow$) and a 90/10 fiber coupler, which directs 90% of the input light to the characterization setup and 10% to the stabilization setup. Here the OFD, which serves as a frequency reference for stabilization, generates an error signal, which is fed into a servo controller for feedback to the laser. This feedback signal is added to the laser drive current. For frequency noise characterization, a delayed self-heterodyne setup is used, which consists of an acousto-optic modulator (AOM) and a 150-m long fiber delay. The photodiode beat signal from this setup is recorded on an oscilloscope and processed to retrieve the frequency stability.

from the OFD is fed to a servo controller equipped with double integrators (Liquid Instruments Moku:Lab, PID), which generates a feedback signal. This feedback signal is added to the laser's amplifier current through the modulation input of the diode current driver (Koheron DRV200).

We characterize the frequency stability of the laser with out-of-loop delayed self-heterodyne measurements, using a similar setup as described in [34]. The setup comprises a fiber delay of 150 m and an acousto-optic modulator (AOM, Opto-Electronic MT80-IIR30-Fio-PM0.5-J1-A-Ic2) driven at 80 MHz. The resulting beat signal is recorded for 100 ms using a balanced photodetector (Thorlabs PDB450C set to 150 MHz bandwidth) connected to an oscilloscope (PicoScope 5444D) and processed to retrieve the frequency-noise power spectral density (PSD) of the laser. The recording time window distorts the PSD calculation at low noise frequencies, thus the data points below 40 Hz are discarded. To retrieve the PSD at high noise frequencies more accurately [169], the PSD for multiple time segments is averaged, after dividing the original time trace in 2^n non-overlapping segments, where $n = 0$ for the lowest Fourier frequencies up to $n = 10$ at the highest frequencies. Measurements of the PSD were carried out for the free running laser and for the locked laser. When the laser was locked to the OFD, we optimized the settings of the servo controller to reduce the PSD in the frequency range below 100 kHz.

Figure 5.4(a) shows the recorded frequency noise PSD of the free-running laser and the stabilized laser, as well as the noise floor of the measurement setup. For the free-running laser, the PSD decreases with Fourier frequency, which is typical for thermo-refractive noise and noise stemming from thermal drifts, acoustic vibrations and flicker noise from electronics. At high Fourier frequencies, beyond 2 MHz, the noise appears to reach a white noise level of 0.7 kHz^2/Hz. Multiplying this level with π yields an upper limit of 2 kHz for the intrinsic linewidth. Noise occurring at a
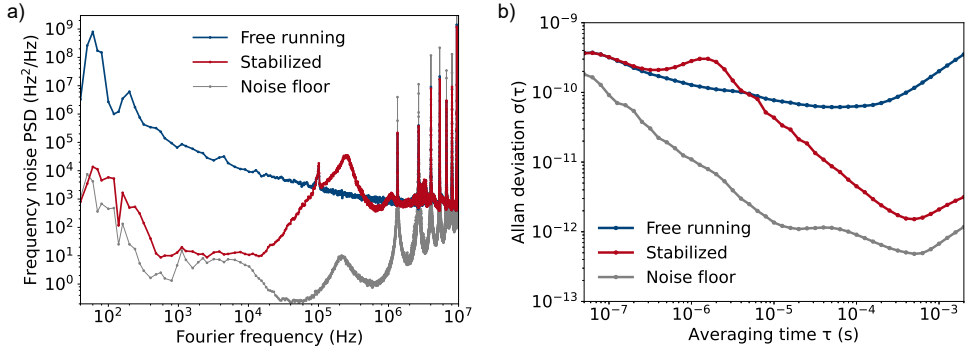
Figure 5.4: (a) The single-sided frequency-noise power spectral density (PSD) retrieved for the free running laser (blue trace) in comparison with the frequency stabilized laser (red trace) and the setup noise floor (gray trace). Frequency stabilization strongly reduces noise for Fourier frequencies up to 10^5 Hz. Toward higher Fourier frequencies, the measured noise reaches approaches a white noise level of approximately 0.7 kHz^2/Hz, which corresponds to an intrinsic linewidth of 2 kHz. (b) Allan deviation for the free running laser (blue trace) in comparison with the frequency stabilized laser (red trace) and the noise floor of the system (gray trace). The Allan deviation of the free-running laser indicates a best stability of $6.2 \cdot 10^{-11}$ for an averaging time of 50 μs. Locking the laser frequency to the OFD improves the stability for averaging times > 7 μs, reaching a minimum of $1.5 \cdot 10^{-12}$ over 0.5 ms.

frequency of 1.3 MHz and its multiples cannot be resolved due to fringes, which is inherent to self-heterodyning with a 150 m fiber delay length.

Next, we measured the frequency noise when the laser frequency was stabilized to the OFD, also shown in Fig. 5.4(a). Stabilizing the laser frequency to the OFD strongly reduces the noise, especially for Fourier frequencies between 0.5 and 18 kHz, where an average noise level of 12 Hz^2/Hz is reached. At Fourier frequencies around 250 KHz, a servo bump is clearly visible. Due to the finite bandwidth of the control loop, for these Fourier frequencies, the feedback signal lags behind and is out of phase with the frequency deviations, so the deviations are amplified rather than suppressed.

To investigate whether the measured frequency noise is limited by the characterization setup, we estimated the noise floor of the setup by removing the delay line to balance the path lengths in both arms of the delayed self-heterodyne setup. Note, by removing the delay line, we may also have removed acoustic or thermal fluctuations in this long fiber from the noise floor measurement. A small contribution of the laser noise is still present in the measured noise floor, which can be seen in Fig. 5.4(a) by the servo bump at 250 kHz, indicating that the path lengths were not exactly balanced. From this estimation of the noise floor, we find that the noise floor is sufficiently low for noise measurements at Fourier frequencies between 60 Hz and 1 kHz, and above 10 kHz. Between Fourier frequencies of 1 and 10 kHz, the measured noise PSD of 13 Hz^2/Hz is close to the noise floor of the measurement setup. To investigate whether the noise PSD was here limited by the oscilloscope, we used a different oscilloscope (Rohde & Schwarz RTE1024) and indeed found a slightly lower noise

PSD of 5 Hz^2/Hz, while the noise floor in this frequency range was reduced to about 0.2 Hz^2/Hz.

To display the frequency stability for different averaging times, Fig. 5.4(b) shows the Allan deviation for the free-running and the stabilized laser. Both traces are calculated from the recorded PSD, using Eq. 5.12 from [170]. The fringes at 1.3 MHz and its multiples were excluded as they are an artifact of the measurement method. For the free-running laser, the Allan deviation reaches a minimum of $6.2 \cdot 10^{-11}$ for an averaging time of 50 μs. Stabilization to the OFD improves the laser's frequency stability by up to two orders of magnitude, reaching a best value of $1.5 \cdot 10^{-12}$ for an averaging time of 500 μs.

5.3.2 Long-term absolute frequency stabilization by locking to acetylene

For all applications using lasers for measurements, stability over the entire duration of the measurement is required. Since many applications require long-term absolute stability, we also investigate the frequency stability over longer times, up to several days. For this purpose, we require an absolute frequency reference within the laser's spectral coverage. A suitable reference is an acetylene gas cell, as the influence of changes in environmental conditions, such as temperature, pressure and electromagnetic fields, on the absorption lines is negligible [171] compared to the measurement accuracy here.

A central prerequisite for successful long-term stabilization is that the laser emission does not hop to other cavity modes, as mode hops are hard to correct for in any stabilization scheme. Even a mode hop to a neighboring mode would shift the laser frequency outside the capture range of the frequency reference, since the calculated 4.6 GHz minimum mode distance for this laser is larger than the sub-GHz linewidth of an acetylene reference line. To avoid mode hops, a high passive stability of the laser cavity length is required. Hybrid integration of the diode amplifier with the feedback chip aims on providing this stability with permanent and robust fixation of the aligned waveguide circuits. To detect any mode hops and, to more detail, record the laser's emission frequency over several days, we use a broadband and ultra-precise wavelength meter.

Figure 5.5 shows the setup used for long-term stabilization. The laser current and TEC were again set to 100 mA and 25 °C, respectively. The fiber-coupled laser output first passes an optical isolator and then a 90/10 fiber-optic coupler. To maximize the photodetector signal, the largest fraction of the laser output is used for frequency stabilization. The stabilization scheme is based on top-of-fringe locking using the principle of frequency modulation (FM) spectroscopy [172]. The light passes an electro-optic phase modulator (EOM, Thorlabs LN65-10-P-A-A-BNL) driven at a modulation frequency of 12.5 MHz. The modulated light then propagates through a fiber-coupled gas cell (Wavelength References C2H2-12-H(16.5)-4-FCAPC), filled with acetylene ($^{12}C_2H_2$), which serves as the frequency reference. Although a Doppler-free measurement of a saturated acetylene absorption line would provide the narrowest reference [124], this also requires a gas pressure that is lower than available for stan-
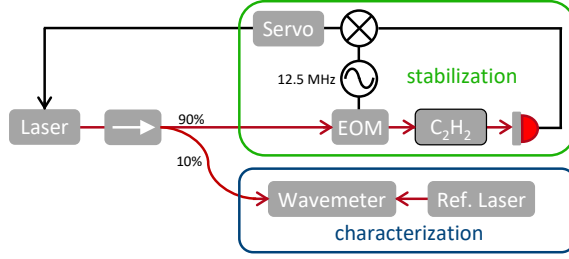
Figure 5.5: Frequency stabilization setup using a fiber-coupled acetylene (C_2H_2) gas cell. Behind the isolator ($\rightarrow$), the laser light passes through a 90/10 fiber coupler, which directs 90% of the input light to the stabilization setup. This setup for top-of-fringe locking comprises an electro-optic modulator (EOM), a fiber-coupled acetylene ($^{12}C_2H_2$) gas cell, a fast photodiode and an electronic servo controller. The controller generates a 12.5 MHz signal for modulating the light and for demodulating the photodiode signal. Feedback from the servo controller is added to the laser's amplifier current. To characterize the frequency stability of the laser, 10% of the output light is directed to a wavelength meter, which is hourly calibrated using a reference diode laser stabilized to a Doppler-free rubidium line.

dard fiber-coupled reference cells. We used a fiber-coupled gas cell with a path length of 16.5 cm and a pressure of 4 Torr, that provides a narrow line of approximately 600 MHz width and 74% peak absorption, as predicted with a HITRAN-based simulation [135]. The power transmitted through the gas cell is measured using an amplified photodetector (Thorlabs PDB450C). The detector signal is fed into a locking module (Toptica DigiLock 110), which demodulates the signal and provides feedback to the laser current using a proportional integral differential (PID) controller.

To measure the long-term stability of the laser, 10% of the laser output is directed to a Fitzeau-interferometer based wavelength meter (HighFinesse Ångstrom WS Ultimate 30 IR). The specified relative accuracy is $3 \cdot 10^{-7}$ and the absolute accuracy is 30 MHz, however, we suspect that the measurement accuracy is well below this specification [173, 174]. The sampling time of the wavelength meter was set automatically with typical sampling times between 50 and 200 ms. To counteract the long-term drift of the wavelength meter, it was calibrated every hour using a reference diode laser stabilized to a Doppler-free rubidium line (^{85}Rb, D_2, crossover $F = 3 \rightarrow F' = 3, 4$) at 780.2 nm. For increasing the accuracy also between calibrations, all measured data points are corrected by assuming a linear drift of the wavelength meter between these hourly calibration points.

To characterize the frequency stability of the free-running laser, we first tuned the laser wavelength to 1531.5879 nm by setting the heaters on the MRRs and the phase section accordingly. This wavelength is at the P11 absorption line, to which we later locked the laser. Figure 5.6(a) shows, as the blue trace, the recorded frequency deviations of the free-running laser over a measurement time of 66 hours. We note that, if any mode hop had occurred during that time, the laser's frequency would deviate by a discontinuous step at least ten times the 400 MHz vertical range chosen for this plot. However, the trace remaining continuously within the displayed vertical range proves that no mode hop occurred for the entire duration of the measurement.
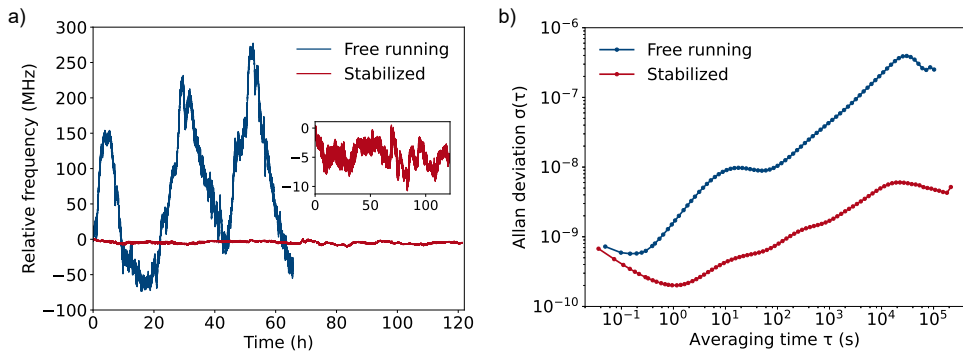
Figure 5.6: (a) Recorded emission frequency, relative to the initial value, of the free-running laser over 65 hours (blue trace) and of the stabilized laser over 121 hours (red trace). A zoom-in of the stabilized laser's relative frequency is displayed in the inset. The frequency of the free-running laser does not show any discontinuities, which confirms the absence of mode hops. The frequency drift remains within a range of 352 MHz, which is small compared to the free spectral range of the laser cavity. The frequency variations follow the 24-hour rhythm of the room temperature. Frequency stabilization to an acetylene absorption line greatly reduces the drift to a range of less than 12 MHz. (b) The overlapping Allan deviation of the free-running laser, as shown with the blue trace, indicates a best frequency stability of $5.7 \cdot 10^{-10}$ for an averaging time of 0.15 seconds. Locking the laser frequency to the acetylene absorption line, as shown in red, improves the long-term stability, reaching a minimum of $2.0 \cdot 10^{-10}$ over 1.2 seconds.

This high passive stability is obtained by the robust hybrid integration of the diode amplifier with the feedback circuit and makes this laser well suited for long-term frequency stabilization.

In free-running operation, the laser frequency drifts within a frequency range of 352 MHz over three days. We found that the frequency drift is strongly correlated with the variation in lab temperature of 1.9 K over 24-hour intervals. This is expected, as the waveguide effective index and therefore the effective length of the laser cavity, are temperature dependent. Although the temperature of the laser submount is stabilized by a TEC controller, the local temperatures in the waveguide circuit can vary due to lab temperature variations. The observed frequency drift is of the same order of magnitude as described in [175] for a similar laser with several different heater settings, which drifted no more than 120 MHz in 90 minutes.

To counteract the drift, we lock the laser's emission frequency to the center of the acetylene absorption line by providing feedback to the diode current. The recorded frequency deviations for the stabilized laser are shown in red in Fig. 5.6(a) for a recording time of over 5 days. It can be seen that the laser remains locked to the absorption line over the 121-hour duration of the measurement. The frequency deviations are within a range of 12 MHz, which is a great reduction of more than one order of magnitude compared to the free running laser. The residual variations in frequency displayed by the wavelength meter can be partly addressed to the thermal sensitivity of the wavelength meter [173], because we observe a remaining correlation

with room temperature.

To further analyze the frequency stability on different time scales, Fig. 5.6(b) displays the overlapping Allan deviation of the frequency deviations of the free-running and the stabilized laser. On short timescales below 0.1 s, we find that the measured stability is only slightly improved. We suspect the limit here is given by the wavelength meter, since [176] reports a measurement of an ultra-stable laser using a higher resolution variant of the wavelength meter used here, where only a slightly lower level of stability is measured. Over longer averaging times, we observe that the frequency of the locked laser is more stable than for the free-running laser, since drifts over longer times can be very well detected and corrected with this locking scheme. The best frequency stability for the free-running laser is $5.7 \cdot 10^{-10}$ over an averaging time of 0.15 seconds. For the locked laser, the frequency stability is improved on all timescales, reaching a minimum of $2.0 \cdot 10^{-10}$ over an averaging time of 1.2 seconds.

5.4 Conclusion and outlook

We have demonstrated the frequency stabilization of a widely-tunable hybrid-integrated diode laser, both on short and long time scales. To provide a steep error signal for short-term stability, we used a fiber-based optical frequency discriminator (OFD) as a reference. By locking the laser to the OFD, the laser's fractional frequency stability reaches a relative stability of $1.5 \cdot 10^{-12}$ over an averaging time of 0.5 ms. For absolute long-term stability, we locked the laser frequency to an acetylene absorption line, which limits the frequency deviations of the laser to a range of less than 12 MHz over 5 days. To further improve the frequency stability, one could use a Doppler-free absorption line [124] which provides a steeper error signal than the pressure-broadened acetylene line used here. Similarly to the approach described in [177], the two references could also be combined by stabilizing the laser to the OFD which in turn could be stabilized to an acetylene absorption line to avoid long-term drifts. As a next step, a fully integrated laser system with reduced frequency noise or absolute stability could be realized by combining a hybrid-integrated laser with an on-chip reference, for example using a spiral resonator [178, 163], a thermally-insensitive ring-resonator readout [179] or a full spectroscopic unit [180, 181].

Long-term stable, low-noise lasers in the telecom range are of great importance for data transmission, where the carrier frequency must comply to a predefined grid [175]. Such chip-integrated lasers will also be of great interest for precision metrology, optical clocks and quantum technology. Typically, these applications require tuning and stabilizing a laser's emission frequency to address particular atomic or molecular transitions, many of them in the visible spectral region. Recently, the wavelength coverage of widely-tunable chip-integrated lasers has been greatly expanded. Heterogeneous integration of III-V materials with Si_3N_4 waveguides has increased its wavelength coverage from the telecom wavelength range toward the 1.0 µm range [61, 66]. On the other hand, hybrid integration with Si_3N_4 and Al_2O_3 waveguides poses less restrictions on material properties and fabrication technologies, which has enabled hybrid integrated ECDLs to enter also the visible spectral range [72, 182, 75]. Such lasers,

stabilized to according references, e.g., to iodine, strontium and rubidium lines, will open up new possibilities for advanced photonics circuits in terms of portability, scalability and stability.

Chapter 6

Conclusion and outlook

6.1 Conclusion

For this thesis, we investigated hybrid-integrated diode lasers, bringing them to more advanced performance. Such lasers, via integration of semiconductor optical amplifiers with low-loss and frequency-selective waveguide feedback circuits, enable robust chip-sized lasers with unique spectral output properties. Specifically, deploying high-Q Si_3N_4 microring resonators as feedback filters, to form extended cavity diode lasers in chip format, provides single-mode operation with wavelength coverage over widest ranges. In addition, the named feedback from high-Q ring resonators resonantly enhances the laser cavity length, from the the millimeter regime to tens of centimeters. Such extension of the laser cavity length results in high frequency stability on short timescales, showing as an ultra-narrow intrinsic (Schawlow-Townes) linewidth. This thesis demonstrates i) that these lasers are also continuously tunable, ii) that the laser concept and thus the spectral coverage can be extended into the visible spectral range, iii) and that these lasers can be long-term frequency stabilized.

In chapter 3 we presented a novel method to increase the range of continuous tuning to that of a short equivalent laser cavity, while maintaining the ultra-narrow linewidth of a long cavity. The combination of broad spectral coverage and wide continuous tunability is of importance for spectroscopic applications and is a pre-condition for electronic frequency stabilization to optical transitions of reference absorbers. We presented an analytical model for extended continuous tuning, confirmed with an experimental demonstration of the extended mode-hop free tuning. Using a single-frequency hybrid integrated InP-Si_3N_4 diode laser with 120 nm coverage around 1540 nm, with a maximum output of 24 mW and lowest intrinsic linewidth of 2.2 kHz, we show a six-fold increased continuous tuning range of 0.22 nm (28 GHz) as compared to the free-spectral range of the laser cavity. Laser tuning was also used to record several Doppler broadened absorption lines of acetylene (C_2H_2) molecules.

In chapter 4 we presented the first realization of a hybrid integrated laser operating in the visible spectral range, while all previous such lasers had been restricted to the

infrared. Providing chip-sized diode lasers in the visible that offer wide coverage and high coherence is of interest for applications in biophotonics, precision metrology and quantum technology. Our laser is based on an AlGaInP optical amplifier for the 685 nm range, coupled to a low-loss Si_3N_4 feedback ring resonator circuit. The laser showed a spectral coverage of 10.8 nm around 684.4 nm wavelength with up to 4.8 mW output power and a measured intrinsic linewidth of 2.3 ± 0.2 kHz.

For long-term stability, we described in chapter 5 our results on the first frequency locking (electronic stabilization) of an extended cavity hybrid-integrated laser to two optical references, namely an acetylene absorption line and a fiber-based optical frequency discriminator (OFD). By locking the laser to the OFD, the laser's frequency stability was improved to a residual fractional instability as low as $1.5 \cdot 10^{-12}$, measured at an averaging time of 0.5 ms. For extending the stability over longer times of several days, we demonstrated locking the laser frequency to an acetylene absorption line, which limited the residual frequency deviations of the laser to a range of less than 12 MHz within 5 days.

We note that during the course of this thesis, my colleagues have demonstrated important progress with hybrid integrated lasers in various other aspects, which is listed as co-authored publications. These comprise a widely tunable diode laser with an ultra-low intrinsic linewidth of 40 Hz, achieved with a long cavity length of 0.5 m on a chip [45], the generation of frequency combs with close to 20 equidistant lines around 1.55 μm and record-low intrinsic optical linewidth of 34 kHz [106], and the first hybrid-integrated laser using the Al_2O_3 waveguide platform, covering a violet range from 403.7 to 408.1 nm with up to 0.74 mW fiber coupled output [75]. Using a laser designed and fabricated in Twente, with a special feedback circuit comprising three (co-prime) ring resonators as described in section 2.2.2, colleagues in the University of Hannover have employed the hybrid integrated laser as fully on-chip quantum light source for the generation of optical entangled quantum states [43].

6.2 Outlook

Based on the described technological developments, it is important to ask in what directions the field of integrated lasers would move. On the one hand, research into these lasers, especially for telecom wavelengths, appears to have been completed to the point where these lasers are developed as a products to be marketed. Next to hybrid integration, such developments can be supported by alternative fabrication and integration techniques, such as heterogeneous integration [85, 77], micro-transfer printing [86, 87], flip-chip bonding techniques [93, 94] or photonic wire bonding [92]. For product development, additional aspects will come into focus, such as environmental robustness [183], calibration, reproducibility, long-term performance and upscaling of production.

Other directions of technological development should focus on higher speed phase actuators with lower power consumption. So far, all feedback circuits described here made use of thermal phase shifters as tuning elements. While straightforward to implement, these phase shifters also have a limited tuning speed (a low bandwidth in

the kHz range). Another problem of thermal phase shifters is their elevated electrical power dissipation, which can be as high as 1 W for a 2π phase shift. To increase the bandwidth into the MHz range and also reduce power consumption, the development of PZT phase shifters on silicon nitride looks very promising [184, 24]. Even faster electro-optic modulation, to reach GHz bandwidths, might require integration with an electro-optic waveguide platform such as based on lithium niobate [185, 22]. The option of faster modulation and frequency control is specifically important for coherent laser ranging and for laser frequency stabilization to external references. Reducing the power requirement of phase shifters is instrumental for upscaling towards many components or devices.

On the other hand, there are fundamental limits that need to be further explored. Specifically, there is the observation of the last years that a different approach to spectral control, so-called self-injection locking, has caught up and meanwhile reached even narrower short-term linewidths than the extended cavity lasers presented here. So far, there are approximate expressions for the linewidth of either approach, for extended cavity lasers such as in section 2.3.2, and for self-injection locking as in [186, 187] and either approach would ultimately be limited by the fundamental Schawlow-Townes limit. However, other properties need to be compared as well, specifically, spectral coverage and mode-hop free tuning. For instance, external feedback to diode lasers, such as is the case in self-injection locking, can cause chaotic behaviour, depending on the phase of feedback and its delay time [188]. Such comparison should comprise experiments, in order to explore also potential technological advantages of either method.

A related fundamental obstacle regarding further narrowing of the intrinsic linewidth was not explicitly mentioned in the bulk of the thesis, namely that we have aimed to reach the sub-Hertz range with feedback circuits comprising high-Q ring resonators. Although theoretically possible with sufficiently high Q-values, we found that thermo-refractive noise was dominating in the RF range that was accessible to us in measurements, masking a fundamental Hertz-level linewidth, especially because of using small ring resonators (radius $\sim 100~\mu$m). Furthermore, reducing the coupling coefficients ($\kappa^2 \sim 0.001$) to increase the Q-value of the feedback resonators was found to lead to a buildup of undesired back-scattering from the resonators, which competes with the transmission signal through the Vernier filter. Improving the design of the Vernier filter, using much larger ring resonators with a high mode volume based on thin and high aspect ratio waveguides, might reduce thermo-refractive noise and undesired back-scattering. This route appears quite promising to pursue, because it would provide a great combination of ultra-low linewidth with high tunability, which does not seem to be present in lasers based on self-injection locking.

Besides linewidth, mode-hop free tuning and wavelength coverage, central issues to explore are the laser output power and the relative intensity noise. While the intensity noise of hybrid integrated lasers can be brought close to the shot noise limit [88], applications benefit from a high signal-to-noise ratio via increasing the output power. This might be achievable with several intracavity amplifiers, or with external diode amplifiers [189], such as tapered amplifiers. Intermediate solutions might be more practical and cost-effective, e.g., using erbium doped fiber amplifiers to amplify the

laser output power, such as was used for the investigation of an integrated Brillouin dynamic grating [190].

Regarding the wavelength coverage, we presented the first hybrid integrated diode laser for the visible spectral range, and several other demonstrations have been following. These examples [70, 73, 74, 75] include also work of our group colleagues addressing red-visible color centers [71], suggesting that numerous further color centers, quantum dots, atomic, ionic, and molecular transitions throughout the visible to near-infrared range can now be considered as well. We expect that present visible sources will stimulate these developments, although moving to much shorter wavelengths will have to involve different waveguide platforms. These will pose new challenges in many respects including design and fabrication of low loss components. A significant challenge will form expansion towards the UV, requiring deep-UV transparent materials, while also the transverse mode size scales down with the wavelength, making mode-coupling between chips more sensitive to misalignment.

The exploration of widely-tunable and ultra-stable diode lasers has just begun. It will be followed by the implementation of on-chip applications, where many exciting developments are to be seen.

Appendix A

As was described by Schawlow and Townes [2], spontaneous emission into the laser mode adds a random phase to the intracavity field, which leads to a finite value of the laser linewidth. Various expressions for the Schawlow Townes linewidth can be found in textbooks, since both the derivation and notation are often tailored for a specific laser type. To derive an expression of this linewidth, one could for example start with the increase of the cold cavity lifetime due to gain [191] or with the definition of the coherence function of the laser output field [110]. Here, our goal is to find the expression for the linewidth of a hybrid integrated lasers as described in this thesis, using measurable quantities. [1]

We follow the approach as described in section 15.4 of the textbook by Milonni and Eberly [110], where a laser is considered that comprises of a resonator based on two mirrors and a gain medium filling the entire resonator. When the auto-correlation of the laser field is calculated, a finite coherence time τ_{coh} is found as as a consequence of spontaneous emission into the laser mode. The Fourier transform of this coherence function yield's the laser's spectrum with a Lorentzian line shape, where the full-width at half-maximum linewidth is given by (see Eq. 15.4.5 from [110])

$$\Delta\nu_{\mathrm{FWHM}} = \frac{1}{\pi\tau_{\mathrm{coh}}} = \frac{1}{2\pi}\frac{\eta_{\mathrm{sp}}\gamma_t}{q_\infty} \tag{A.1}$$

where q_∞ is the number of intracavity photons when the laser is in steady state. Since the number of photons can become very large, the laser output becomes spectrally very narrow. The factor η_{sp} is called the spontaneous emission factor or the population inversion factor [50], which is given by $\eta_{\mathrm{sp}} = N_2/\left(N_2 - N_1\right)$, where N_2 and N_1 are the occupation densities of the upper (conduction band) and lower level (valence band) of the lasing transition, respectively. γ_t is the total loss rate of photons leaving the resonator per unit time and is related to the cavity photon lifetime τ_p and the cold cavity linewidth $\Delta\nu_c$ by

$$\gamma_t = \frac{1}{\tau_p} = 2\pi\Delta\nu_c \tag{A.2}$$

The temporal loss rate γ_t can also be expressed as the spatially averaged total loss coefficient (per roundtrip cavity length) α_t multiplied by the group velocity v_g

$$\gamma_t = v_g\alpha_t \tag{A.3}$$

---

[1]The derivation as presented here is a continuation of initial work by dr. Peter van der Slot.

For deriving Eq. A.1 it was assumed that both amplitude and phase fluctuations of the intracavity laser field contribute to the laser linewidth. However, above laser threshold, the amplitude fluctuations are stabilized due to gain clamping. As a consequence, for above threshold operation, only the phase fluctuations contribute to the linewidth, which results in a factor of 2 reduction of the laser linewidth. The linewidth expression including this reduction factor is also called the modified Schawlow-Townes linewidth [191]

$$\Delta\nu_{\mathrm{ST}} = \frac{1}{4\pi}\frac{\eta_{\mathrm{sp}}\gamma_t}{q_\infty} \tag{A.4}$$

To express this laser linewidth $\Delta\nu_{\mathrm{ST}}$ via the cold cavity linewidth $\Delta\nu_c$, we insert Eq. A.2 in Eq. A.4 and find

$$\Delta\nu_{\mathrm{ST}} = \frac{1}{2}\frac{\eta_{\mathrm{sp}}\Delta\nu_c}{q_\infty} \tag{A.5}$$

The hybrid lasers as described in more detail here are different as they consist of two separate components. These are an optical amplifier and a feedback circuit, which are referred to using subscript 'a' and 'b', respectively. Consider such a laser, as schematically shown in Fig. A.1, where the optical amplifier has a back facet mirror with reflectivity $R_1 = |r_1|^2$ and the optical power that leaves the resonator through this mirror is defined as P_1. Light from the amplifier is coupled to the feedback circuit, and vice versa, with a coupling efficiency of η. The feedback circuit includes an end mirror with reflectivity $R_2 = |r_2|^2$. The optical power P_2 is that is extracted through this mirror is the main output power of the laser, which is measured using an optical power sensor. Note, this is different from the situation as assumed in [88] for simplification where the main output power P_1 is extracted from the back facet of the optical amplifier. For the lasers described in this thesis, it is more convenient to attach a fiber to the feedback circuit, and therefore we consider that the main output power P_2 is extracted there. The feedback circuit also contains a spectral filter for the selection of a single resonator mode. Integrated feedback circuits can be designed such that the filter transmission function between amplifier and end mirror is different from the filter function in the other direction. Therefore, we distinguish between the spectral filter transmission $T_b^{\rightarrow}(\omega)$ and $T_b^{\leftarrow}(\omega)$ for both directions. The length of the gain chip is designated as L_a. The length and corresponding phase delay through the feedback chip are disregarded at this point, since these are included later on as a separate linewidth reduction factor.

To express the internal cavity photon number q_∞ in terms of externally measured powers, we follow the changes of the photon number along a laser cavity roundtrip. This allows to calculate the number of photons at the mirror positions, and relate it with the reflectivity of both mirrors and the measurable output power. Let $q_1^{\rightarrow}$ be the number of photons at the location of mirror 1 travelling towards mirror 2. The number of photons incident on mirror 2 is

$$q_2^{\rightarrow} = e^{(g-\alpha_a)L_a}\eta T_b^{\rightarrow}q_1^{\rightarrow} \tag{A.6}$$

with g and α_a the gain and absorption coefficients per length unit of the optical
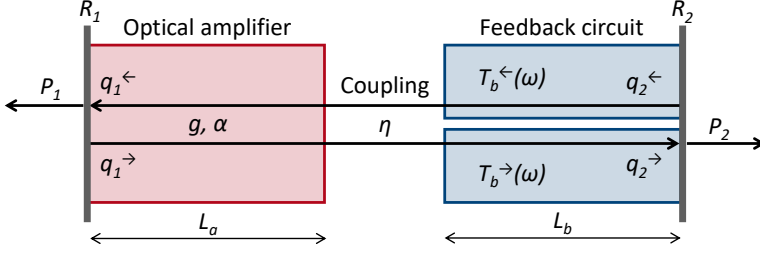
Figure A.1: Schematic of a hybrid laser comprising an optical amplifier and a feedback circuit, having length L_a and L_b, respectively. Light propagates via waveguides on both chips that are coupled with coupling efficiency η. The gain and loss coefficients of the amplifier are defined as g and α, respectively. The transmission through the feedback chip depends on the transmission direction as $T_b^{\rightarrow}(\omega)$ and $T_b^{\leftarrow}(\omega)$. The mirror reflectivities are defined as R_1 and R_2, while the corresponding optical powers coupled out from the resonator at these mirrors are defined as P_1 and P_2. The photon numbers $q_1^{\leftarrow}$, $q_1^{\rightarrow}$, $q_2^{\leftarrow}$ and $q_2^{\leftarrow}$ close to the mirrors 1 and 2 are dependent propagation direction, as indicated with the arrows.

amplifier. The output power, measured at mirror 2, becomes

$$P_2 = \frac{h\nu}{\tau_r} \left(1 - R_2\right) e^{(g-\alpha_a)L_a} \eta T_b^{\rightarrow} q_1^{\rightarrow} \tag{A.7}$$

where $h\nu$ is the photon energy of the emitted light and τ_r is the resonator roundtrip time. The number of photons reflected at mirror 2 is $q_2^{\leftarrow} = R_2 q_2^{\rightarrow}$. Continuation of the resonator roundtrip towards mirror 1 gives the number of photons incident on mirror 1 as

$$q_1^{\leftarrow} = R_2 e^{2(g-\alpha_a)L_a} \eta^2 T_b^{\rightarrow} T_b^{\leftarrow} q_1^{\rightarrow} \tag{A.8}$$

The optical power of the light coupled out from the cavity through mirror 1 is then

$$P_1 = \frac{h\nu}{\tau_r} \left(1 - R_1\right) R_2 e^{2(g-\alpha_a)L} \eta^2 T_b^{\rightarrow} T_b^{\leftarrow} q_1^{\rightarrow} \tag{A.9}$$

To complete the roundtrip, the photons incident on mirror 1 are reflected again described as $q_1^{\rightarrow} = R_1 q_1^{\leftarrow}$, i.e.,

$$q_1^{\rightarrow} = R_1 R_2 e^{2(g-\alpha_a)L_a} \eta^2 T_b^{\rightarrow} T_b^{\leftarrow} q_1^{\rightarrow} \tag{A.10}$$

After completing one roundtrip, we can conclude using Eq. A.10 that the laser is in steady state if the gain g is depleted to a value such that it compensates all the losses and output coupling

$$R_1 R_2 e^{2(g-\alpha_a)L_a} \eta^2 T_b^{\rightarrow} T_b^{\leftarrow} = 1 \tag{A.11}$$

To simplify Eq. A.11, we introduce the so-called distributed mirror loss coefficient α_m as

$$\alpha_m \equiv -\frac{1}{2L_a} \ln\left[R_1 R_2\right] \tag{A.12}$$

Using this, the steady state condition Eq. A.11, can be simplified to

$$e^{2(g-\alpha_a-\alpha_m)L_a}\eta^2 T_b^{\rightarrow}T_b^{\leftarrow} = 1 \tag{A.13}$$

To find the relation between the optical powers P_1 and P_2 emitted from the cavity mirrors, we first rewrite the steady state condition Eq. A.11 as

$$e^{2(g-\alpha_a)L_a} = \frac{1}{R_1 R_2 \eta^2 T_b^{\rightarrow}T_b^{\leftarrow}} \tag{A.14}$$

Next, we use this expression to eliminate $e^{(g-\alpha_a)L_a}$ and $e^{2(g-\alpha_a)L_a}$ from Eqs. A.7 and A.9

$$P_2 = \frac{h\nu}{\tau_r} \frac{1-R_2}{\sqrt{R_1 R_2}} \frac{T_b^{\rightarrow}}{\sqrt{T_b^{\rightarrow}T_b^{\leftarrow}}} q_1^{\rightarrow} \tag{A.15}$$

and

$$P_1 = \frac{h\nu}{\tau_r} \frac{(1-R_1)}{R_1} q_1^{\rightarrow} \tag{A.16}$$

Combining Eqs. A.15 and A.16 gives

$$P_1 = \frac{1-R_1}{1-R_2}\sqrt{\frac{R_2}{R_1}} \frac{\sqrt{T_b^{\rightarrow}T_b^{\leftarrow}}}{T_b^{\rightarrow}} P_2 \tag{A.17}$$

as the relation between the optical powers P_1 and P_2.

To rewrite the Schawlow-Townes linewidth expression, which depends on the number of intracavity photons, we need to relate the number of intracavity photons q_∞ with the measured output power P_2. However, from the derivation above, it can be concluded that the number of intracavity photons in steady state varies spatially, due to losses in the amplifier and filter, and outcoupling at the mirrors. If these losses are low, the optical field inside the cavity can be assumed to be uniform, and the mean value of the intracavity photons can be considered. This assumption is also called the mean-field approximation. For hybrid lasers, which typically have high intracavity losses, numerical modelling is required to obtain a fully realistic linewidth value [112]. For the ease of deriving an analytic expression, we proceed with the the mean-field approximation as an estimate. We retrieve the number of intracavity photons travelling in the both directions through the cavity, by relating these photons with the total power leaving the resonator and the temporal mirror loss rate γ_m, i.e.,

$$P_1 + P_2 = h\nu\gamma_m q_\infty \tag{A.18}$$

The temporal mirror loss rate is defined as

$$\gamma_m = v_g \alpha_m \tag{A.19}$$

where we use the distributed mirror loss α_m as defined in Eq. A.12, to convert the temporal loss to a spatially distributed loss, similar as in Eq. A.3. Using Eqs. A.17 and A.19 we can rewrite Eq. A.18 as

$$q_\infty = \frac{1}{v_g h\nu\alpha_m}\left(1 + \frac{1-R_1}{1-R_2}\sqrt{\frac{R_2}{R_1}}\frac{\sqrt{T_b^{\rightarrow}T_b^{\leftarrow}}}{T_b^{\rightarrow}}\right) P_2 \tag{A.20}$$

Finally, filling Eqs. A.20 and A.3 into Eq. A.4 gives an expression for the Schawlow-Townes linewidth for the hybrid laser as schematically introduced in Fig. A.1

$$\Delta\nu_{\text{ST}} = \frac{1}{4\pi} \frac{v_g^2 h\nu\eta_{\text{sp}}\alpha_m\alpha_t}{P_2 \left(1 + \frac{1-R_1}{1-R_2}\sqrt{\frac{R_2}{R_1}}\frac{\sqrt{T_b^\rightarrow T_b^\leftarrow}}{T_b^\rightarrow}\right)} \tag{A.21}$$

In case the filter transmission function is symmetric for a cavity roundtrip, i.e. $T_b^\rightarrow(\omega) = T_b^\leftarrow(\omega)$, this can be simplified to

$$\Delta\nu_{\text{ST}} = \frac{1}{4\pi} \frac{v_g^2 h\nu\eta_{\text{sp}}\alpha_m\alpha_t}{P_2 \left(1 + \frac{1-R_1}{1-R_2}\sqrt{\frac{R_2}{R_1}}\right)} \tag{A.22}$$

A comparison of Eq. A.22 with the expression Eq. (1) provided in [88] reveals that exchanging P_1 and P_2 as the main output power requires that also R_1 and R_2 are exchanged in the linewidth expression. For the laser feedback circuits as schematically shown in Figs. 3.2(a) and 5.1(a), a filter is placed only between the amplifier and the end mirror R_2. In that case, the transmission function $T_b^\leftarrow(\omega)$ equals unity and A.21 reduces to

$$\Delta\nu_{\text{ST}} = \frac{1}{4\pi} \frac{v_g^2 h\nu\eta_{\text{sp}}\alpha_m\alpha_t}{P_2 \left(1 + \frac{1-R_1}{1-R_2}\sqrt{\frac{R_2}{R_1}}\frac{1}{\sqrt{T_b^\rightarrow}}\right)} \tag{A.23}$$

The Schawlow-Townes linewidth expressed in the form of Eq. A.23 is used as the starting point in section 2.3.2, before introducing several extra linewidth enhancement factors that are required to incorporate additional physical effects in semiconductor lasers and hybrid-integrated lasers.

Bibliography

[1] J. Hecht, "The First Half-Century of Laser Development," Laser Tech. J. **7**, 20–25 (2010).

[2] A. L. Schawlow and C. H. Townes, "Infrared and Optical Masers," Phys. Rev. **112**, 1940–1949 (1958).

[3] T. Maiman, "Stimulated Optical Radiation in Ruby," Nature. **187**, 493–494 (1960).

[4] R. N. Hall, G. E. Fenner, J. D. Kingsley, T. J. Soltys, and R. O. Carlson, "Coherent Light Emission From GaAs Junctions," Phys. Rev. Lett. **9**, 366–368 (1962).

[5] M. I. Nathan, W. P. Dumke, G. Burns, F. H. Dill, and G. Lasher, "Stimulated emission of radiation from GaAs p-n junctions," Appl. Phys. Lett. **1**, 62–64 (1962).

[6] P. Winzer and R.-J. Essiambre, "Advanced Optical Modulation Formats," Proc. IEEE **94**, 952–985 (2006).

[7] S. L. Olsson, J. Cho, S. Chandrasekhar, X. Chen, P. J. Winzer, and S. Makovejs, "Probabilistically shaped PDM 4096-QAM transmission over up to 200 km of fiber using standard intradyne detection," Opt. Express **26**, 4522–4530 (2018).

[8] Y. Lin, C. Browning, R. B. Timens, D. H. Geuzebroek, C. G. H. Roeloffzen, M. Hoekman, D. Geskus, R. M. Oldenbeuving, R. G. Heideman, Y. Fan, K.-J. Boller, and L. P. Barry, "Characterization of Hybrid InP-TriPleX Photonic Integrated Tunable Lasers Based on Silicon Nitride (Si_3N_4/SiO_2) Microring Resonators for Optical Coherent System," IEEE Photonics J. **10**, 1400108 (2018).

[9] K. Zou, Z. Zhang, P. Liao, H. Wang, Y. Cao, A. Almaiman, A. Fallahpour, F. Alishahi, N. Satyan, G. Rakuljic, M. Tur, A. Yariv, and A. E. Willner, "Higher-order QAM data transmission using a high-coherence hybrid Si/III–V semiconductor laser," Opt. Lett. **45**, 1499–1502 (2020).

[10] L. N. Venkatasubramani, D. Dass, C. Browning, C. G. Roeloffzen, D. Geuzebroek, and L. Barry, "Bandwidth Re-Configurable Wideband QAM-OFDM With Hybrid Integrated InP-Si_3N_4 Tunable Laser Source for Short-Reach Systems," J. Light. Technol. **41**, 3612–3619 (2023).

[11] D. Dass, A. Delmade, L. Barry, C. G. H. Roeloffzen, D. Geuzebroek, and C. Browning, "Wavelength & mm-Wave Flexible Converged Optical Fronthaul With a Low Noise Si-Based Integrated Dual Laser Source," J. Light. Technol. **40**, 3307–3315 (2022).

[12] M. Burla, D. Marpaung, L. Zhuang, A. Leinse, M. Hoekman, R. Heideman, and C. Roeloffzen, "Integrated Photonic Ku-Band Beamformer Chip With Continuous Amplitude and Delay Control," IEEE Photonics Technol. Lett. **25**, 1145–1148 (2013).

[13] D. Marpaung and J. Yao, "Integrated microwave photonics," Nat. Photonics **13**, 80–90 (2019).

[14] T. Miya, Y. Terunuma, T. Hosaka, and T. Miyashita, "Ultimate low-loss single-mode fibre at 1.55 μm," Electron. Lett. **15**, 106–108 (1979).

[15] J. F. Bauters, M. J. R. Heck, D. D. John, J. S. Barton, C. M. Bruinink, A. Leinse, R. G. Heideman, D. J. Blumenthal, and J. E. Bowers, "Planar waveguides with less than 0.1 dB/m propagation loss fabricated with wafer bonding," Opt. Express **19**, 24090–24101 (2011).

[16] N. Poli, M. Schioppo, S. Vogt, S. Falke, U. Sterr, C. Lisdat, and G. M. Tino, "A transportable strontium optical lattice clock," Appl. Phys. B **117**, 1107–1116 (2014).

[17] Z. L. Newman, V. Maurice, T. Drake, J. R. Stone, T. C. Briles, D. T. Spencer, C. Fredrick, Q. Li, D. Westly, B. R. Ilic, B. Shen, M.-G. Suh, K. Y. Yang, C. Johnson, D. M. S. Johnson, L. Hollberg, K. J. Vahala, K. Srinivasan, S. A. Diddams, J. Kitching, S. B. Papp, and M. T. Hummon, "Architecture for the photonic integration of an optical atomic clock," Optica **6**, 680–685 (2019).

[18] J. Grotti, S. Koller, S. Vogt, S. Häfner, U. Sterr, C. Lisdat, H. Denker, C. Voigt, L. Timmen, A. Rolland, F. N. Baynes, H. S. Margolis, M. Zampaolo, P. Thoumany, M. Pizzocaro, B. Rauf, F. Bregolin, A. Tampellini, P. Barbieri, M. Zucco, G. A. Costanzo, C. Clivati, F. Levi, and D. Calonico, "Geodesy and metrology with a transportable optical clock," Nat. Phys. **14**, 437–441 (2018).

[19] T. Bothwell, C. J. Kennedy, A. Aeppli, D. Kedar, J. M. Robinson, E. Oelker, A. Staron, and J. Ye, "Resolving the gravitational redshift across a millimetre-scale atomic sample," Nature. **602**, 420–424 (2022).

[20] C. Liu, L. Lu, Y. Guo, X. Li, J. Chen, and L. Zhou, "Hybrid Integrated Frequency-Modulated Continuous-Wave Laser With Synchronous Tuning," J. Light. Technol. **40**, 5636–5645 (2022).

[21] G. Lihachev, J. Riemensberger, W. Weng, J. Liu, H. Tian, A. Siddharth, V. Snigirev, V. Shadymov, A. Voloshin, R. N. Wang, J. He, S. A. Bhave, and T. J. Kippenberg, "Low-noise frequency-agile photonic integrated lasers for coherent ranging," Nat. Commun. **13**, 3522 (2022).

[22] V. Snigirev, A. Riedhauser, G. Lihachev, M. Churaev, J. Riemensberger, R. N. Wang, A. Siddharth, G. Huang, C. Möhl, Y. Popoff, U. Drechsler, D. Caimi, S. Hönl, J. Liu, P. Seidler, and T. J. Kippenberg, "Ultrafast tunable lasers using lithium niobate integrated photonics," Nature. **615**, 411–417 (2023).

[23] A. Raptakis, L. Gounaridis, M. Weigel, M. Kleinert, M. Georgiopoulos, E. Mylonas, P. Groumas, C. Tsokos, N. Keil, H. Avramopoulos, and C. Kouloumentas, "2D Optical Phased Arrays for Laser Beam Steering Based on 3D Polymer Photonic Integrated Circuits," J. Light. Technol. **39**, 6509–6523 (2021).

[24] A. Raptakis, L. Gounaridis, J. P. Epping, T. L. A. Tran, T. Aukes, M. Kleinert, M. Weigel, M. Wolfer, A. Draebenstedt, C. Tsokos, P. Groumas, E. Andrianopoulos, N. Lyras, D. Nikolaidis, E. Mylonas, N. Baxevanakis, R. Pessina, E. Schreuder, M. Dekkers, V. Seyfried, N. Keil, R. G. Heideman, H. Avramopoulos, and C. Kouloumentas, "Integrated heterodyne laser Doppler vibrometer based on stress-optic frequency shift in silicon nitride," PhotoniX. **4**, 30 (2023).

[25] L. Tombez, E. J. Zhang, J. S. Orcutt, S. Kamlapurkar, and W. M. J. Green, "Methane absorption spectroscopy on a silicon photonic chip," Optica. **4**, 1322–1325 (2017).

[26] M. G. Allen, "Diode laser absorption sensors for gas-dynamic and combustion flows," Meas. Sci. Technol. **9**, 545–562 (1998).

[27] D. Kohler, G. Schindler, L. Hahn, J. Milvich, A. Hofmann, K. Länge, W. Freude, and C. Koos, "Biophotonic sensors with integrated Si_3N_4-organic hybrid (SiNOH) lasers for point-of-care diagnostics," Light. Sci. & Appl. **10**, 64 (2021).

[28] K. E. Zinoviev, A. B. Gonzalez-Guerrero, C. Dominguez, and L. M. Lechuga, "Integrated Bimodal Waveguide Interferometric Biosensor for Label-Free Analysis," J. Light. Technol. **29**, 1926–1930 (2011).

[29] W. D. Sacher, X. Luo, Y. Yang, F.-D. Chen, T. Lordello, J. C. C. Mak, X. Liu, T. Hu, T. Xue, P. Guo-Qiang Lo, M. L. Roukes, and J. K. S. Poon, "Visible-light silicon nitride waveguide devices and implantable neurophotonic probes on thinned 200 mm silicon wafers," Opt. Express **27**, 37400–37418 (2019).

[30] B. Stern, X. Ji, Y. Okawachi, A. L. Gaeta, and M. Lipson, "Battery-operated integrated frequency comb generator," Nature **562**, 401–405 (2018).

[31] P. Maier, Y. Chen, Y. Xu, Y. Bao, M. Blaicher, D. Geskus, R. Dekker, J. Liu, P.-I. Dietrich, H. Peng, S. Randel, W. Freude, T. J. Kippenberg, and C. Koos, "Sub-kHz-Linewidth External-Cavity Laser (ECL) With Si_3N_4 Resonator Used as a Tunable Pump for a Kerr Frequency Comb," J. Light. Technol. **41**, 3479–3490 (2023).

[32] M.-G. Suh, Q.-F. Yang, K. Y. Yang, X. Yi, and K. J. Vahala, "Microresonator soliton dual-comb spectroscopy," Science. **354**, 600–603 (2016).

[33] R. Botter, K. Ye, Y. Klaver, R. Suryadharma, O. Daulay, G. Liu, J. van den Hoogen, L. Kanger, P. van der Slot, E. Klein, M. Hoekman, C. Roeloffzen, Y. Liu, and D. Marpaung, "Guided-acoustic stimulated Brillouin scattering in silicon nitride photonic circuits," Sci. Adv. **8**, eabq2196 (2022).

[34] N. Chauhan, A. Isichenko, K. Liu, J. Wang, Q. Zhao, R. O. Behunin, P. T. Rakich, A. M. Jayich, C. Fertig, C. W. Hoyt, and D. J. Blumenthal, "Visible light photonic integrated Brillouin laser," Nat. Commun. **12**, 4685 (2021).

[35] S. Gundavarapu, G. M. Brodnik, M. Puckett, T. Huffman, D. Bose, R. Behunin, J. Wu, T. Qiu, C. Pinho, N. Chauhan, J. Nohava, P. T. Rakich, K. D. Nelson, M. Salit, and D. J. Blumenthal, "Sub-hertz fundamental linewidth photonic integrated Brillouin laser," Nat. Photonics **13**, 60–67 (2019).

[36] A. W. Elshaari, W. Pernice, K. Srinivasan, O. Benson, and V. Zwiller, "Hybrid integrated quantum photonic circuits," Nat. Photonics **14**, 285–298 (2020).

[37] J. Wang, F. Sciarrino, A. Laing, and M. G. Thompson, "Integrated photonic quantum technologies," Nat. Photonics **14**, 273–284 (2020).

[38] E. Pelucchi, G. Fagas, I. Aharonovich, D. Englund, E. Figueroa, Q. Gong, H. Hannes, J. Liu, C.-Y. Lu, N. Matsuda, J.-W. Pan, F. Schreck, F. Sciarrino, C. Silberhorn, J. Wang, and K. D. Jöns, "The potential and global outlook of integrated photonics for quantum technologies," Nat. Rev. Phys. **4**, 194–208 (2021).

[39] H. Haffner, C. Roos, and R. Blatt, "Quantum computing with trapped ions," Phys. Reports **469**, 155–203 (2008).

[40] R. J. Niffenegger, J. Stuart, C. Sorace-Agaskar, D. Kharas, S. Bramhavar, C. D. Bruzewicz, W. Loh, R. T. Maxson, R. McConnell, D. Reens, G. N. West, J. M. Sage, and J. Chiaverini, "Integrated multi-wavelength control of an ion qubit," Nature **586**, 538–542 (2020).

[41] K. K. Mehta, C. Zhang, M. Malinowski, T.-L. Nguyen, M. Stadler, and J. P. Home, "Integrated optical multi-ion quantum logic," Nature **586**, 533–537 (2020).

[42] C. Qiao, C. Z. Tan, F. C. Hu, L. Couturier, I. Nosske, P. Chen, Y. H. Jiang, B. Zhu, and M. Weidemüller, "An ultrastable laser system at 689 nm for cooling and trapping of strontium," Appl. Phys. B **125**, 215 (2019).

[43] H. Mahmudlu, R. Johanning, A. van Rees, A. K. Kashi, J. P. Epping, R. Haldar, K.-J. Boller, and M. Kues, "Fully on-chip photonic turnkey quantum source for entangled qubit/qudit state generation," Nat. Photonics **17**, 518–524 (2023).

[44] P. A. Morton, C. Xiang, J. B. Khurgin, C. D. Morton, M. Tran, J. Peters, J. Guo, M. J. Morton, and J. E. Bowers, "Integrated Coherent Tunable Laser (ICTL) With Ultra-Wideband Wavelength Tuning and Sub-100 Hz Lorentzian Linewidth," J. Light. Technol. **40**, 1802–1809 (2022).

[45] Y. Fan, A. van Rees, P. J. M. van der Slot, J. Mak, R. M. Oldenbeuving, M. Hoekman, D. Geskus, C. G. H. Roeloffzen, and K.-J. Boller, "Hybrid integrated InP-Si$_3$N$_4$ diode laser with a 40-Hz intrinsic linewidth," Opt. Express **28**, 21713–21727 (2020).

[46] W. Jin, Q.-F. Yang, L. Chang, B. Shen, H. Wang, M. A. Leal, L. Wu, M. Gao, A. Feshali, M. Paniccia, K. J. Vahala, and J. E. Bowers, "Hertz-linewidth semiconductor lasers using CMOS-ready ultra-high-Q microresonators," Nat. Photonics **15**, 346–353 (2021).

[47] J. Guo, C. A. McLemore, C. Xiang, D. Lee, L. Wu, W. Jin, M. Kelleher, N. Jin, D. Mason, L. Chang, A. Feshali, M. Paniccia, P. T. Rakich, K. J. Vahala, S. A. Diddams, F. Quinlan, and J. E. Bowers, "Chip-based laser with 1-hertz integrated linewidth," Sci. Adv. **8**, eabp9006 (2022).

[48] C. Xiang, W. Jin, O. Terra, B. Dong, H. Wang, L. Wu, J. Guo, T. J. Morin, E. Hughes, J. Peters, Q.-X. Ji, A. Feshali, M. Paniccia, K. J. Vahala, and J. E. Bowers, "3D integration enables ultralow-noise isolator-free lasers in silicon photonics," Nature. **620**, 78–85 (2023).

[49] B. Li, W. Jin, L. Wu, L. Chang, H. Wang, B. Shen, Z. Yuan, A. Feshali, M. Paniccia, K. J. Vahala, and J. E. Bowers, "Reaching fiber-laser coherence in integrated photonics," Opt. Lett. **46**, 5201–5204 (2021).

[50] M. A. Tran, D. Huang, and J. E. Bowers, "Tutorial on narrow linewidth tunable semiconductor lasers using Si/III-V heterogeneous integration," APL Photonics **4**, 111101 (2019).

[51] Y. Guo, X. Li, M. Jin, L. Lu, J. Xie, J. Chen, and L. Zhou, "Hybrid integrated external cavity laser with a 172-nm tuning range," APL Photonics **7**, 066101 (2022).

[52] M. Ishizaka and H. Yamazaki, "Wavelength tunable laser using silica double ring resonators," Electron. Commun. Jpn. (Part II: Electron. **89**, 34–41 (2006).

[53] R. M. Oldenbeuving, E. J. Klein, H. L. Offerhaus, C. J. Lee, H. Song, and K. J. Boller, "25 kHz narrow spectral bandwidth of a wavelength tunable diode laser with a short waveguide-based external cavity," Laser Phys. Lett. **10**, 015804 (2013).

[54] R. Wang, A. Malik, I. Šimonytė, A. Vizbaras, K. Vizbaras, and G. Roelkens, "Compact GaSb/silicon-on-insulator 2.0x μm widely tunable external cavity lasers," Opt. Express **24**, 28977–28986 (2016).

[55] R. Wang, S. Sprengel, A. Vasiliev, G. Boehm, J. V. Campenhout, G. Lepage, P. Verheyen, R. Baets, M.-C. Amann, and G. Roelkens, "Widely tunable 2.3 μm III-V-on-silicon Vernier lasers for broadband spectroscopic sensing," Photon. Res. **6**, 858–866 (2018).

[56] J. X. B. Sia, W. Wang, Z. Qiao, X. Li, X. Guo, J. Zhou, C. G. Littlejohns, Z. Zhang, C. Liu, G. T. Reed, and H. Wang, "Compact silicon photonic hybrid ring external cavity (SHREC)/InGaSb-AlGaAsSb wavelength-tunable laser diode operating from 1881-1947 nm," Opt. Express **28**, 5134–5146 (2020).

[57] J. X. Brian Sia, X. Li, W. Wang, Z. Qiao, X. Guo, J. Zhou, C. G. Littlejohns, C. Liu, G. T. Reed, and H. Wang, "Sub-kHz linewidth, hybrid III-V/silicon wavelength-tunable laser diode operating at the application-rich 1647-1690 nm," Opt. Express **28**, 25215–25224 (2020).

[58] S.-P. Ojanen, J. Viheriälä, M. Cherchi, N. Zia, E. Koivusalo, P. Karioja, and M. Guina, "GaSb diode lasers tunable around 2.6 μm using silicon photonics resonators or external diffractive gratings," Appl. Phys. Lett. **116**, 081105 (2020).

[59] J. X. B. Sia, X. Li, W. Wang, Z. Qiao, X. Guo, J. Wang, C. G. Littlejohns, C. Liu, G. T. Reed, K. S. Ang, and H. Wang, "Compact, Hybrid III-V/Silicon Vernier Laser Diode Operating From 1955–1992 nm," IEEE Photonics J. **13**, 1500205 (2021).

[60] N. Zia, S.-P. Ojanen, J. Viheriala, E. Koivusalo, J. Hilska, H. Tuorila, and M. Guina, "Widely tunable 2 μm hybrid laser using GaSb semiconductor optical amplifiers and a Si_3N_4 photonics integrated reflector," Opt. Lett. **48**, 1319–1322 (2023).

[61] J. T. Bovington, M. J. R. Heck, and J. E. Bowers, "Heterogeneous lasers and coupling to Si_3N_4 near 1060 nm," Opt. Lett. **39**, 6017–6020 (2014).

[62] T. Komljenovic, S. Srinivasan, E. Norberg, M. Davenport, G. Fish, and J. E. Bowers, "Widely Tunable Narrow-Linewidth Monolithically Integrated External-Cavity Semiconductor Lasers," IEEE J. Sel. Top. Quantum Electron. **21**, 1501909 (2015).

[63] S. Kumari, J. Gustavsson, E. P. Haglund, J. Bengtsson, A. Larsson, G. Roelkens, and R. Baets, "Design of an 845-nm GaAs Vertical-Cavity Silicon-Integrated Laser with an Intracavity Grating for Coupling to a SiN Waveguide Circuit," IEEE Photonics J. **9**, 1504109 (2017).

[64] Y. Zhu and L. Zhu, "Narrow-linewidth, tunable external cavity dual-band diode lasers through InP/GaAs-Si_3N_4 hybrid integration," Opt. Express **27**, 2354–2362 (2019).

[65] Y. Han, X. Zhang, F. Huang, X. Liu, M. Xu, Z. Lin, M. He, S. Yu, R. Wang, and X. Cai, "Electrically pumped widely tunable o-band hybrid lithium niobite/iii-v laser," Opt. Lett. pp. 5413–5416 (2021).

[66] M. A. Tran, C. Zhang, T. J. Morin, L. Chang, S. Barik, Z. Yuan, W. Lee, G. Kim, A. Malik, Z. Zhang, J. Guo, H. Wang, B. Shen, L. Wu, K. Vahala, J. E. Bowers, H. Park, and T. Komljenovic, "Extending the spectrum of fully integrated photonics to submicrometre wavelengths," Nature. **610**, 54–60 (2022).

[67] N. Schilder, A. Everhardt, T. Horner, D. Geskus, E. Klein, M. Benedictus, S. Kriswandhi, F. Schreuder, and R. G. Heideman, "850 nm hybrid-integrated tunable laser with Si_3N_4 micro-ring resonator feedback circuits," in *Optical Fiber Communications Conference and Exhibition (OFC),* (IEEE, 2022), p. Th1E.6.

[68] J. Guo, C. Xiang, T. J. Morin, J. D. Peters, L. Chang, and J. E. Bowers, "E-band widely tunable, narrow linewidth heterogeneous laser on silicon," APL Photonics **8** (2023).

[69] R. Frentrop, N. A. Schilder, I. Hegeman, A. S. Everhardt, E. J. Klein, D. H. Geuzebroek, L. V. Winkler, J. Ensher, R. G. Heideman, and C. Kelly, "800 nm narrow linewidth tunable hybrid laser based on a dual microring external cavity," in *Novel In-Plane Semiconductor Lasers XXII,* vol. 12440 (SPIE Photonics West, 2023), p. 1244003.

[70] M. Corato-Zanarella, A. Gil-Molina, X. Ji, M. C. Shin, A. Mohanty, and M. Lipson, "Widely tunable and narrow-linewidth chip-scale lasers from near-ultraviolet to near-infrared wavelengths," Nat. Photonics **17**, 157–164 (2023).

[71] L. Winkler, K. Gerritsma, A. van Rees, P. Schrinner, M. Hoekman, R. Dekker, P. van der Slot, C. Nölleke, and K.-J. Boller, "Tunable Hybrid-Integrated Diode Laser at 637 nm," in *Conference on Lasers and Electro-Optics Europe & European Quantum Electronics Conference (CLEO/Europe-EQEC),* (IEEE, 2023), p. 124241K.

[72] C. A. A. Franken, A. van Rees, L. V. Winkler, Y. Fan, D. Geskus, R. Dekker, D. H. Geuzebroek, C. Fallnich, P. J. M. van der Slot, and K.-J. Boller, "Hybrid-integrated diode laser in the visible spectral range," Opt. Lett. **46**, 4904–4907 (2021).

[73] A. Siddharth, T. Wunderer, G. Lihachev, A. S. Voloshin, C. Haller, R. N. Wang, M. Teepe, Z. Yang, J. Liu, J. Riemensberger, N. Grandjean, N. Johnson, and T. J. Kippenberg, "Near ultraviolet photonic integrated lasers based on silicon nitride," APL Photonics **7**, 046108 (2022).

[74] T. Wunderer, A. Siddharth, N. M. Johnson, C. L. Chua, M. Teepe, M. Batres, P. Maeda, G. Likhachev, and T. J. Kippenberg, "Single-Frequency Violet and Blue Laser Emission from AlGaInN Photonic Integrated Circuit Chips," Opt. Open (2023).

[75] C. A. A. Franken, W. A. P. M. Hendriks, L. V. Winkler, M. Dijkstra, A. R. do Nascimento, A. van Rees, M. R. S. Mardani, R. Dekker, J. van Kerkhof, P. J. M. van der Slot, S. M. García-Blanco, and K. J. Boller, "Hybrid integrated near UV lasers using the deep-UV Al_2O_3 platform," arXiv p. 2302.11492 (2023).

[76] M. A. Tran, D. Huang, J. Guo, T. Komljenovic, P. A. Morton, and J. E. Bowers, "Ring-resonator based Widely-tunable narrow-linewidth Si/InP integrated lasers," IEEE J. Sel. Top. Quantum Electron. **26**, 1500514 (2020).

[77] C. Xiang, W. Jin, D. Huang, M. A. Tran, J. Guo, Y. Wan, W. Xie, G. Kurczveil, A. M. Netherton, D. Liang, H. Rong, and J. E. Bowers, "High-Performance Silicon Photonics Using Heterogeneous Integration," IEEE J. Sel. Top. Quantum Electron. **28**, 8200515 (2022).

[78] M. Smit, K. Williams, and J. van der Tol, "Past, present, and future of InP-based photonic integration," APL Photonics **4**, 050901 (2019).

[79] P. Muñoz, P. W. L. van Dijk, D. Geuzebroek, M. Geiselmann, C. Domínguez, A. Stassen, J. D. Doménech, M. Zervas, A. Leinse, C. G. H. Roeloffzen, B. Gargallo, R. Baños, J. Fernández, G. M. Cabanes, L. A. Bru, and D. Pastor, "Foundry Developments Toward Silicon Nitride Photonics From Visible to the Mid-Infrared," IEEE J. Sel. Top. Quantum Electron. **25**, 8200513 (2019).

[80] M. A. Porcel, A. Hinojosa, H. Jans, A. Stassen, J. Goyvaerts, D. Geuzebroek, M. Geiselmann, C. Dominguez, and I. Artundo, "Silicon nitride photonic integration for visible light applications," Opt. & Laser Technol. **112**, 299–306 (2019).

[81] M. W. Puckett, K. Liu, N. Chauhan, Q. Zhao, N. Jin, H. Cheng, J. Wu, R. O. Behunin, P. T. Rakich, K. D. Nelson, and D. J. Blumenthal, "422 Million intrinsic quality factor planar integrated all-waveguide resonator with sub-MHz linewidth," Nat. Commun. **12**, 934 (2021).

[82] K. Liu, N. Jin, H. Cheng, N. Chauhan, M. W. Puckett, K. D. Nelson, R. O. Behunin, P. T. Rakich, and D. J. Blumenthal, "Ultralow 0.034 dB/m loss wafer-scale integrated photonics realizing 720 million Q and 380 μW threshold Brillouin lasing," Opt. Lett. **47**, 1855–1858 (2022).

[83] D. de Felipe, Z. Zhang, W. Brinker, M. Kleinert, A. M. Novo, C. Zawadzki, M. Moehrle, and N. Keil, "Polymer-Based External Cavity Lasers: Tuning Efficiency, Reliability, and Polarization Diversity," IEEE Photonics Technol. Lett. **26**, 1391–1394 (2014).

[84] X. Zhang, X. Liu, L. Liu, Y. Han, H. Tan, L. Liu, Z. Lin, S. Yu, R. Wang, and X. Cai, "Heterogeneous integration of III–V semiconductor lasers on thin-film lithium niobite platform by wafer bonding," Appl. Phys. Lett. **122**, 081103 (2023).

[85] C. Xiang, J. Guo, W. Jin, L. Wu, J. Peters, W. Xie, L. Chang, B. Shen, H. Wang, Q.-F. Yang, D. Kinghorn, M. Paniccia, K. J. Vahala, P. A. Morton, and J. E. Bowers, "High-performance lasers for fully integrated silicon nitride photonics," Nat. Commun. **12**, 6650 (2021).

[86] C. O. de Beeck, B. Haq, L. Elsinger, A. Gocalinska, E. Pelucchi, B. Corbett, G. Roelkens, and B. Kuyken, "Heterogeneous III-V on silicon nitride amplifiers and lasers via microtransfer printing," Optica. **7**, 386–393 (2020).

[87] E. Soltanian, G. Muliuk, S. Uvin, D. Wang, G. Lepage, P. Verheyen, J. V. Campenhout, S. Ertl, J. Rimböck, N. Vaissiere, D. Néel, J. Ramirez, J. Decobert, B. Kuyken, J. Zhang, and G. Roelkens, "Micro-transfer-printed narrow-linewidth III-V-on-Si double laser structure with a combined 110 nm tuning range," Opt. Express **30**, 39329–39339 (2022).

[88] K.-J. Boller, A. van Rees, Y. Fan, J. Mak, R. E. M. Lammerink, C. A. A. Franken, P. J. M. van der Slot, D. A. I. Marpaung, C. Fallnich, J. P. Epping, R. M. Oldenbeuving, D. Geskus, R. Dekker, I. Visscher, R. Grootjans, C. G. H. Roeloffzen, M. Hoekman, E. J. Klein, A. Leinse, and R. G. Heideman, "Hybrid integrated semiconductor lasers with silicon nitride feedback circuits," Photonics **7**, 4 (2019).

[89] X. Li, J. Shi, L. Wei, K. Ding, Y. Ma, Z. Li, L. Li, Y. Qu, Z. Qiao, G. Liu, and L. Zeng, "Research on Silicon-Substrate-Integrated Widely Tunable, Narrow Linewidth External Cavity Lasers," Crystals **12**, 674 (2022).

[90] C. Porter, S. Zeng, X. Zhao, and L. Zhu, "Hybrid integrated chip-scale laser systems," APL Photonics **8** (2023).

[91] G. Brunetti, R. Heuvink, E. Schreuder, M. N. Armenise, and C. Ciminelli, "Silicon Nitride Spot Size Converter With Very Low-Loss Over the C-Band," IEEE Photonics Technol. Lett. **35**, 1215–1218 (2023).

[92] Y. Xu, P. Maier, M. Blaicher, P.-I. Dietrich, P. Marin-Palomo, W. Hartmann, Y. Bao, H. Peng, M. R. Billah, S. Singer, U. Troppenz, M. Moehrle, S. Randel, W. Freude, and C. Koos, "Hybrid external-cavity lasers (ECL) using photonic wire bonds as coupling elements," Sci. Reports **11**, 16426 (2021).

[93] M. Theurer, M. Moehrle, A. Sigmund, K.-O. Velthaus, R. M. Oldenbeuving, L. Wevers, F. M. Postma, R. Mateman, F. Schreuder, D. Geskus, K. Worhoff, R. Dekker, R. G. Heideman, and M. Schell, "Flip-Chip Integration of InP to SiN Photonic Integrated Circuits," J. Light. Technol. **38**, 2630–2636 (2020).

[94] W. Tian, L. Beste, A. Khachikyan, C. Mittelstadt, R. Dekker, K. Worhoff, J. V. Kerkhof, R. Santos, K. Williams, and X. Leijtens, "Flip-Chip Bonding of InP Die on SiN-Based TriPleX Carrier With Novel Laser Soldering," IEEE J. Quantum Electron. **59**, 0600307 (2023).

[95] B. Liu, A. Shakouri, and J. E. Bowers, "Passive microring-resonator-coupled lasers," Appl. Phys. Lett. **79**, 3561–3563 (2001).

[96] B. Liu, A. Shakouri, and J. Bowers, "Wide tunable double ring resonator coupled lasers," IEEE Photonics Technol. Lett. **14**, 600–602 (2002).

[97] Y. Fan, J. P. Epping, R. M. Oldenbeuving, C. G. H. Roeloffzen, M. Hoekman, R. Dekker, R. G. Heideman, P. J. M. van der Slot, and K.-J. Boller, "Optically Integrated InP-Si$_3$N$_4$ Hybrid Laser," IEEE Photonics J. **8**, 1–11 (2016).

[98] A. van Rees, Y. Fan, D. Geskus, E. Klein, R. Oldenbeuving, P. van der Slot, and K.-J. Boller, "Ring resonator enhanced mode-hop-free wavelength tuning of an integrated extended-cavity laser," Opt. Express **28**, 5669–5683 (2020).

[99] D. G. Rabus, *Integrated ring resonators. The compendium* (Springer, 2007).

[100] C. G. H. Roeloffzen, M. Hoekman, E. J. Klein, L. S. Wevers, R. B. Timens, D. Marchenko, D. Geskus, R. Dekker, A. Alippi, R. Grootjans, A. van Rees, R. M. Oldenbeuving, J. P. Epping, R. G. Heideman, K. Wörhoff, A. Leinse, D. Geuzebroek, E. Schreuder, P. W. L. van Dijk, I. Visscher, C. Taddei, Y. Fan, C. Taballione, Y. Liu, D. Marpaung, L. Zhuang, M. Benelajla, and K.-J. Boller, "Low-Loss Si$_3$N$_4$ TriPleX Optical Waveguides: Technology and Applications Overview," IEEE J. Sel. Top. Quantum Electron. **24**, 4400321 (2018).

[101] W. Bogaerts, P. de Heyn, T. van Vaerenbergh, K. de Vos, S. K. Selvaraja, T. Claes, P. Dumon, P. Bienstman, D. van Thourhout, and R. Baets, "Silicon microring resonators," Laser & Photonics Rev. **6**, 47–73 (2012).

[102] W. Tsong, I. van den Vlekkert, S. Musa, R. N. Frentrop, N. A. Schilder, M. Hoekman, A. Meijerink, E. J. Klein, and D. Geskus, "139 nm tuning range, high speed wavelength modulation, and high output power up to 60 mW from a single gain, two-ring vernier external cavity laser," in *Integrated Optics: Devices, Materials, and Technologies XXVII*, S. M. García-Blanco and P. Cheben, eds. (SPIE Photonics West, 2023), p. 124240G.

[103] T. Matsumoto, A. Suzuki, M. Takahashi, S. Watanabe, S. Ishii, K. Suzuki, T. Kaneko, H. Yamazaki, and N. Sakuma, "Narrow Spectral Linewidth Full Band Tunable Laser Based on Waveguide Ring Resonators with Low Power Consumption," in *Optical Fiber Communication Conference,* (OSA, 2010), p. OThQ5.

[104] T. Komljenovic, S. Liu, E. Norberg, G. A. Fish, and J. E. Bowers, "Control of Widely Tunable Lasers With High-Q Resonator as an Integral Part of the Cavity," J. Light. Technol. **35**, 3934–3939 (2017).

[105] Y. Guo, X. Li, W. Xu, C. Liu, M. Jin, L. Lu, J. Xie, A. Stroganov, J. Chen, and L. Zhou, "A hybrid-integrated external cavity laser with ultra-wide wavelength tuning range and high side-mode suppression," in *Optical Fiber Communication Conference (OFC),* (2022), p. Tu3D.4.

[106] J. Mak, A. van Rees, Y. Fan, E. J. Klein, D. Geskus, P. J. van der Slot, and K.-J. Boller, "Linewidth narrowing via low-loss dielectric waveguide feedback circuits in hybrid integrated frequency comb lasers," Opt. Express **27**, 13307–13318 (2019).

[107] A. Memon, A. van Rees, J. Mak, Y. Fan, P. J. M. van der Slot, H. M. J. Bastiaens, and K.-J. Boller, "Using hybrid integrated InP-Si$_3$N$_4$ diode lasers for the generation of sub-GHz repetition rate frequency combs," in *Integrated Optics: Devices, Materials, and Technologies XXVII*, S. M. García-Blanco and P. Cheben, eds. (SPIE Photonics West, 2023), p. 124240H.

[108] C. Rimoldi, L. L. Columbo, J. Bovington, S. Romero-Garcia, and M. Gioannini, "CW Emission and Self-Pulsing in a III-V/SiN Hybrid Laser With Narrow Band Mirror," IEEE Photonics J. **14**, 1540707 (2022).

[109] G. D. Domenico, S. Schilt, and P. Thomann, "Simple approach to the relation between laser frequency noise and laser line shape," Appl. Opt. **49**, 4801–4807 (2010).

[110] P. W. Milonni and J. H. Eberly, *Laser Physics* (Wiley, 2010).

[111] C. Henry, "Theory of the linewidth of semiconductor lasers," IEEE J. Quantum Electron. **18**, 259–264 (1982).

[112] Y. Fan, R. E. Lammerink, J. Mak, R. M. Oldenbeuving, P. J. van der Slot, and K.-J. Boller, "Spectral linewidth analysis of semiconductor hybrid lasers with feedback from an external waveguide resonator circuit," Opt. Express **25**, 32767–32782 (2017).

[113] Y. Fan, "Semiconductor-glass waveguide hybrid lasers with ultra-high spectral purity," Ph.D. thesis, University of Twente (2017).

[114] R. Kazarinov and C. Henry, "The relation of line narrowing and chirp reduction resulting from the coupling of a semiconductor laser to passive resonator," IEEE J. Quantum Electron. **23**, 1401–1409 (1987).

[115] G. Agrawal and C. Bowden, "Concept of linewidth enhancement factor in semiconductor lasers: its usefulness and limitations," IEEE Photonics Technol. Lett. **5**, 640–642 (1993).

[116] G. Huang, E. Lucas, J. Liu, A. S. Raja, G. Lihachev, M. L. Gorodetsky, N. J. Engelsen, and T. J. Kippenberg, "Thermorefractive noise in silicon-nitride microresonators," Phys. Rev. A **99**, 061801 (2019).

[117] N. Kondratiev and M. Gorodetsky, "Thermorefractive noise in whispering gallery mode microresonators: Analytical results and numerical simulation," Phys. Lett. A **382**, 2265–2268 (2018).

[118] M. L. Gorodetsky and I. S. Grudinin, "Fundamental thermal fluctuations in microspheres," J. Opt. Soc. Am. B **21**, 697–705 (2004).

[119] A. Arbabi and L. L. Goddard, "Measurements of the refractive indices and thermo-optic coefficients of Si_3N_4 and SiO_x using microring resonances," Opt. letters **38**, 3878–3881 (2013).

[120] C. E. Wieman and L. Hollberg, "Using diode lasers for atomic physics," Rev. Sci. Instruments **62**, 1–20 (1991).

[121] J. M. Lopez-Higuera, L. Rodriguez Cobo, A. Quintela Incera, and A. Cobo, "Fiber Optic Sensors in Structural Health Monitoring," J. Light. Technol. **29**, 587–608 (2011).

[122] A. S. Raja, A. S. Voloshin, H. Guo, S. E. Agafonova, J. Liu, A. S. Gorodnitskiy, M. Karpov, N. G. Pavlov, E. Lucas, R. R. Galiev, A. E. Shitikov, J. D. Jost, M. L. Gorodetsky, and T. J. Kippenberg, "Electrically pumped photonic integrated soliton microcomb," Nat. Commun. **10**, 680 (2019).

[123] J. Buus, M.-C. Amann, and D. J. Blumenthal, *Tunable Laser Diodes and Related Optical Sources* (Wiley-IEEE Press, 2005).

[124] M. de Labachelerie, K. Nakagawa, Y. Awaji, and M. Ohtsu, "High-frequency-stability laser at 1.5 μm using Doppler-free molecular lines," Opt. Lett. **20**, 572–574 (1995).

[125] M. Lax, "Classical Noise. V. Noise in Self-Sustained Oscillators," Phys. Rev. **160**, 290–307 (1967).

[126] M. G. Littman, "Single-mode operation of grazing-incidence pulsed dye laser," Opt. Lett. **3**, 138–140 (1978).

[127] K. Liu and M. G. Littman, "Novel geometry for single-mode scanning of tunable lasers," Opt. Lett. **6**, 117–118 (1981).

[128] M. Fleming and A. Mooradian, "Spectral characteristics of external-cavity controlled semiconductor lasers," IEEE J. Quantum Electron. **17**, 44–59 (1981).

[129] K. Kasai, M. Nakazawa, Y. Tomomatsu, and T. Endo, "1.5μm, mode-hop-free full C-band wavelength tunable laser diode with a linewidth of 8 kHz and a RIN of -130 dB/Hz and its extension to the L-band," Opt. Express **25**, 22113–22124 (2017).

[130] K. Kobayashi and I. Mito, "Single frequency and tunable laser diodes," J. Light. Technol. **6**, 1623–1633 (1988).

[131] L. A. Coldren, "Monolithic tunable diode lasers," IEEE J. Sel. Top. Quantum Electron. **6**, 988–999 (2000).

[132] N. Kobayashi, K. Sato, M. Namiwaka, K. Yamamoto, S. Watanabe, T. Kita, H. Yamada, and H. Yamazaki, "Silicon Photonic Hybrid Ring-Filter External Cavity Wavelength Tunable Lasers," J. Light. Technol. **33**, 1241–1246 (2015).

[133] B. Stern, X. Ji, A. Dutt, and M. Lipson, "Compact narrow-linewidth integrated laser based on a low-loss silicon nitride ring resonator," Opt. Lett. **42**, 4541–4544 (2017).

[134] T. Komljenovic, L. Liang, R.-l. Chao, J. Hulme, S. Srinivasan, M. Davenport, and J. E. Bowers, "Widely-Tunable Ring-Resonator Semiconductor Lasers," Appl. Sci. **7**, 732 (2017).

[135] C. S. Goldenstein, V. A. Miller, R. Mitchell Spearrin, and C. L. Strand, "SpectraPlot.com: Integrated spectroscopic modeling of atomic and molecular gases," J. Quant. Spectrosc. Radiat. Transf. **200**, 249–257 (2017).

[136] L. Rothman, I. Gordon, Y. Babikov, A. Barbe, D. C. Benner, P. Bernath, M. Birk, L. Bizzocchi, V. Boudon, L. Brown, A. Campargue, K. Chance, E. Cohen, L. Coudert, V. Devi, B. Drouin, A. Fayt, J.-M. Flaud, R. Gamache, J. Harrison, J.-M. Hartmann, C. Hill, J. Hodges, D. Jacquemart, A. Jolly, J. Lamouroux, R. L. Roy, G. Li, D. Long, O. Lyulin, C. Mackie, S. Massie, S. Mikhailenko, H. Müller, O. Naumenko, A. Nikitin, J. Orphal, V. Perevalov, A. Perrin, E. Polovtseva, C. Richard, M. Smith, E. Starikova, K. Sung, S. Tashkun, J. Tennyson, G. Toon, V. Tyuterev, and G. Wagner, "The HITRAN2012 molecular spectroscopic database," J. Quant. Spectrosc. Radiat. Transf. **130**, 4–50 (2013).

[137] R. Amin, R. Maiti, C. Carfano, Z. Ma, M. H. Tahersima, Y. Lilach, D. Ratnayake, H. Dalir, and V. J. Sorger, "0.52 V mm ITO-based Mach-Zehnder modulator in silicon photonics," APL Photonics **3**, 126104 (2018).

[138] A. Tandaechanurat, S. Ishida, D. Guimard, M. Nomura, S. Iwamoto, and Y. Arakawa, "Lasing oscillation in a three-dimensional photonic crystal nanocavity with a complete bandgap," Nat. Photonics **5**, 91–94 (2011).

[139] Y. Takahashi, Y. Inui, M. Chihara, T. Asano, R. Terawaki, and S. Noda, "A micrometre-scale Raman silicon laser with a microwatt threshold," Nature **498**, 470 – 474 (2013).

[140] K. Numata, J. Camp, M. A. Krainak, and L. Stolpner, "Performance of planar-waveguide external cavity laser for precision measurements," Opt. Express **18**, 22781–22788 (2010).

[141] D. Huang, M. A. Tran, J. Guo, J. Peters, T. Komljenovic, A. Malik, P. A. Morton, and J. E. Bowers, "High-power sub-kHz linewidth lasers fully integrated on silicon," Optica **6**, 745–752 (2019).

[142] C. Grivas, "Optically pumped planar waveguide lasers: Part II: Gain media, laser systems, and applications," Prog. Quantum Electron. **45-46**, 3–160 (2016).

[143] K. M. Kiani, H. C. Frankis, H. M. Mbonde, R. Mateman, A. Leinse, A. P. Knights, and J. D. B. Bradley, "Thulium-doped tellurium oxide waveguide amplifier with 7.6 dB net gain on a silicon nitride chip," Opt. Lett. **44**, 5788–5791 (2019).

[144] J.-C. Tinguely, Ø. I. Helle, and B. S. Ahluwalia, "Silicon nitride waveguide platform for fluorescence microscopy of living cells," Opt. Express **25**, 27678–27690 (2017).

[145] L. Liu, D. Shan, X. Zhou, H. Shi, B. Song, F. Falke, A. Leinse, and R. Heideman, "TriPleX™ waveguide-based fluorescence biosensor for multichannel environmental contaminants detection," Biosens. Bioelectron. **106**, 117–121 (2018).

[146] I. M. White and X. Fan, "On the performance quantification of resonant refractive index sensors," Opt. Express **16**, 1020–1028 (2008).

[147] Y. Sun, K. Zhou, Q. Sun, J. Liu, M. Feng, Z. Li, Y. Zhou, L. Zhang, D. Li, S. Zhang, M. Ikeda, S. Liu, and H. Yang, "Room-temperature continuous-wave electrically injected InGaN-based laser directly grown on Si," Nat. Photonics **10**, 595–599 (2016).

[148] D. Melati, F. Morichetti, and A. Melloni, "A unified approach for radiative losses and backscattering in optical waveguides," J. Opt. **16**, 055502 (2014).

[149] T. Kamei, T. Kamikawa, M. Araki, S. P. DenBaars, S. Nakamura, and J. E. Bowers, "Research Toward a Heterogeneously Integrated InGaN Laser on Silicon," Phys. Status Solidi A **217**, 1900770 (2020).

[150] D. T. Spencer, J. F. Bauters, M. J. R. Heck, and J. E. Bowers, "Integrated waveguide coupled Si_3N_4 resonators in the ultrahigh-Q regime," Optica **1**, 153–157 (2014).

[151] L. Richter, H. Mandelberg, M. Kruger, and P. McGrath, "Linewidth determination from self-heterodyne measurements with subcoherence delay times," IEEE J. Quantum Electron. **22**, 2070–2074 (1986).

[152] L. B. Mercer, "1/f frequency noise effects on self-heterodyne linewidth measurements," J. Light. Technol. **9**, 485–493 (1991).

[153] A. T. Mashayekh, T. Klos, D. Geuzebroek, E. Klein, T. Veenstra, M. Büscher, F. Merget, P. Leisching, and J. Witzens, "Silicon nitride PIC-based multi-color laser engines for life science applications," Opt. Express **29**, 8635–8653 (2021).

[154] P. Ciddor and R. Duffy, "Two-mode frequency-stabilised He-Ne (633 nm) lasers: studies of short-and long-term stability," J. Phys. E: Sci. Instruments **16**, 1223–1227 (1983).

[155] W. Rowley, "The performance of a longitudinal Zeeman-stabilised He-Ne laser (633 nm) with thermal modulation and control," Meas. Sci. Technol. **1**, 348–351 (1990).

[156] A. Arnold, J. Wilson, and M. Boshier, "A simple extended-cavity diode laser," Rev. Sci. Instruments **69**, 1236–1239 (1998).

[157] A. Martin, P. Baus, and G. Birkl, "External cavity diode laser setup with two interference filters," Appl. Phys. B **122**, 298 (2016).

[158] F. Krause, E. Benkler, C. Nölleke, P. Leisching, and U. Sterr, "Simple and compact diode laser system stabilized to Doppler-broadened iodine lines at 633 nm," Appl. Opt. **59**, 10808–10812 (2020).

[159] S. Herbers, S. Häfner, S. Dörscher, T. Lücke, U. Sterr, and C. Lisdat, "Transportable clock laser system with an instability of 1.6×10^{-16}," Opt. Lett. **47**, 5441–5444 (2022).

[160] D. G. Matei, T. Legero, S. Häfner, C. Grebing, R. Weyrich, W. Zhang, L. Sonderhouse, J. M. Robinson, J. Ye, F. Riehle, and U. Sterr, "1.5 μm Lasers with Sub-10 mHz Linewidth," Phys. Rev. Lett. **118**, 263202 (2017).

[161] C. Cherfan, I. Manai, S. Zemmouri, J.-C. Garreau, J.-F. Clément, P. Szriftgiser, and R. Chicireanu, "Acetylene-based frequency stabilization of a laser system for potassium laser cooling," Opt. Express **28**, 494–502 (2020).

[162] W. Zhang, L. Stern, D. Carlson, D. Bopp, Z. Newman, S. Kang, J. Kitching, and S. B. Papp, "Ultranarrow Linewidth Photonic-Atomic Laser," Laser & Photonics Rev. **14**, 1900293 (2020).

[163] K. Liu, N. Chauhan, J. Wang, A. Isichenko, G. M. Brodnik, P. A. Morton, R. O. Behunin, S. B. Papp, and D. J. Blumenthal, "36 Hz integral linewidth laser based on a photonic integrated 4.0 m coil resonator," Optica. **9**, 770–775 (2022).

[164] L. Stern, W. Zhang, L. Chang, J. Guo, C. Xiang, M. A. Tran, D. Huang, J. D. Peters, D. Kinghorn, J. E. Bowers, and S. B. Papp, "Ultra-precise optical-frequency stabilization with heterogeneous III–V/Si lasers," Opt. Lett. **45**, 5275–5278 (2020).

[165] L.-S. Ma, P. Jungner, J. Ye, and J. L. Hall, "Delivering the same optical frequency at two places: accurate cancellation of phase noise introduced by an optical fiber or other time-varying path," Opt. Lett. **19**, 1777–1779 (1994).

[166] L. V. Winkler, A. van Rees, P. J. van der Slot, C. Nölleke, and K.-J. Boller, "Frequency stabilization of a hybrid-integrated InP-Si$_3$N$_4$ diode laser by locking to a fiber ring resonator," in *25th Annual Symposium of the IEEE Photonics Benelux Chapter,* (IEEE, 2021).

[167] F. Kéfélian, H. Jiang, P. Lemonde, and G. Santarelli, "Ultralow-frequency-noise stabilization of a laser by locking to an optical fiber-delay line," Opt. Lett. **34**, 914–916 (2009).

[168] T. Day, E. Gustafson, and R. Byer, "Sub-hertz relative frequency stabilization of two-diode laser-pumped Nd:YAG lasers locked to a Fabry-Perot interferometer," IEEE J. Quantum Electron. **28**, 1106–1117 (1992).

[169] Z. Yuan, H. Wang, P. Liu, B. Li, B. Shen, M. Gao, L. Chang, W. Jin, A. Feshali, M. Paniccia, J. Bowers, and K. Vahala, "Correlated self-heterodyne method for ultra-low-noise laser linewidth measurements," Opt. Express **30**, 25147–25161 (2022).

[170] J. Rutman, "Characterization of phase and frequency instabilities in precision frequency sources: Fifteen years of progress," Proc. IEEE **66**, 1048–1075 (1978).

[171] W. C. Swann and S. L. Gilbert, "Pressure-induced shift and broadening of 1510–1540-nm acetylene wavelength calibration lines," J. Opt. Soc. Am. B **17**, 1263–1270 (2000).

[172] G. C. Bjorklund, M. D. Levenson, W. Lenth, and C. Ortiz, "Frequency modulation (FM) spectroscopy," Appl. Phys. B Photophysics Laser Chem. **32**, 145–152 (1983).

[173] K. Saleh, J. Millo, A. Didier, Y. Kersalé, and C. Lacroûte, "Frequency stability of a wavelength meter and applications to laser frequency stabilization," Appl. Opt. **54**, 9446–9449 (2015).

[174] K. König, P. Imgram, J. Krämer, B. Maaß, K. Mohr, T. Ratajczyk, F. Sommer, and W. Nörtershäuser, "On the performance of wavelength meters: Part 2—frequency-comb based characterization for more accurate absolute wavelength determinations," Appl. Phys. B **126**, 86 (2020).

[175] L. Gonzalez-Guerrero, R. Guzman, M. Ali, A. Zarzuelo, J. Cesar, D. Dass, C. Browning, L. P. Barry, I. Visscher, R. Grootjans, C. G. H. Roeloffzen, and G. Carpintero, "Injection Locking Properties of an InP-Si$_3$N$_4$ Dual Laser Source for Mm-wave Communications," J. Light. Technol. **40**, 6685–6692 (2022).

[176] L. Couturier, I. Nosske, F. Hu, C. Tan, C. Qiao, Y. Jiang, P. Chen, and M. Weidemüller, "Laser frequency stabilization using a commercial wavelength meter," Rev. Sci. Instruments **89**, 043103 (2018).

[177] Y. Sakai, I. Yokohama, T. Kominato, and S. Sudo, "Frequency stabilization of laser diode using a frequency-locked ring resonator to acetylene gas absorption lines," IEEE Photonics Technol. Lett. **3**, 868–870 (1991).

[178] H. Lee, M.-G. Suh, T. Chen, J. Li, S. A. Diddams, and K. J. Vahala, "Spiral resonators for on-chip laser frequency stabilization," Nat. Commun. **4**, 2468 (2013).

[179] Q. Zhao, M. W. Harrington, A. Isichenko, K. Liu, R. O. Behunin, S. B. Papp, P. T. Rakich, C. W. Hoyt, C. Fertig, and D. J. Blumenthal, "Integrated reference cavity with dual-mode optical thermometry for frequency correction," Optica. **8**, 1481–1487 (2021).

[180] M. T. Hummon, S. Kang, D. G. Bopp, Q. Li, D. A. Westly, S. Kim, C. Fredrick, S. A. Diddams, K. Srinivasan, V. Aksyuk, and J. E. Kitching, "Photonic chip for laser stabilization to an atomic vapor with 10^{-11} instability," Optica. **5**, 443–449 (2018).

[181] R. Zektzer, M. T. Hummon, L. Stern, Y. Sebbag, Y. Barash, N. Mazurski, J. Kitching, and U. Levy, "A Chip-Scale Optical Frequency Reference for the Telecommunication Band Based on Acetylene," Laser & Photonics Rev. **14**, 1900414 (2020).

[182] L. V. Winkler, K. Gerritsma, A. van Rees, P. P. J. Schrinner, M. Hoekman, R. Dekker, P. J. M. van der Slot, C. Nölleke, and K.-J. Boller, "Silicon nitride hybrid-integrated diode laser at 637 nm," in *Integrated Optics: Devices, Materials, and Technologies XXVII,* vol. 12424 (SPIE Photonics West, 2023), p. 124241K.

[183] J. P. Epping, A. Leinse, R. Oldenbeuving, I. Visscher, D. H. Geuzebroek, D. Geskus, A. van Rees, K. J. Boller, M. Theurer, M. Möhrle, M. Schell, C. G. Roeloffzen, and R. Heideman, "Hybrid integrated silicon nitride lasers,"

in *Physics and Simulation of Optoelectronic Devices XXVIII,* (SPIE Photonics West, 2020), p. 112741L.

[184] N. Hosseini, R. Dekker, M. Hoekman, M. Dekkers, J. Bos, A. Leinse, and R. Heideman, "Stress-optic modulator in TriPleX platform using a piezoelectric lead zirconate titanate (PZT) thin film," Opt. Express **23**, 14018–14026 (2015).

[185] M. Li, L. Chang, L. Wu, J. Staffa, J. Ling, U. A. Javid, S. Xue, Y. He, R. Lopez-rios, T. J. Morin, H. Wang, B. Shen, S. Zeng, L. Zhu, K. J. Vahala, J. E. Bowers, and Q. Lin, "Integrated Pockels laser," Nat. Commun. **13**, 5344 (2022).

[186] K. Petermann, *Laser Diode Modulation and Noise* (Springer Netherlands, 1988).

[187] N. M. Kondratiev, V. E. Lobanov, A. V. Cherenkov, A. S. Voloshin, N. G. Pavlov, S. Koptyaev, and M. L. Gorodetsky, "Self-injection locking of a laser diode to a high-Q WGM microresonator," Opt. Express **25**, 28167–28178 (2017).

[188] J. Mork, B. Tromborg, and J. Mark, "Chaos in semiconductor lasers with optical feedback: theory and experiment," IEEE J. Quantum Electron. **28**, 93–108 (1992).

[189] C. Chen, F. Wei, X. Han, Q. Su, H. Pi, G. Xin, H. Wu, A. Stroganov, Y. Sun, W. Ren, X. Chen, Q. Ye, H. Cai, and W. Chen, "Hybrid integrated Si_3N_4 external cavity laser with high power and narrow linewidth," Opt. Express **31**, 26078–26091 (2023).

[190] R. Botter, J. van den Hoogen, A. Mishra, K. Ye, A. van Rees, M. Hoekman, K. Boller, and D. Marpaung, "Observation of a Brillouin dynamic grating in silicon nitride waveguides," arXiv p. 2308.09814 (2023).

[191] L. A. Coldren, S. W. Corzine, and M. L. Mašanović, *Diode Lasers and Photonic Integrated Circuits* (Wiley, 2012), 2nd ed.

Summary

This thesis describes our investigation into diode lasers based on hybrid integration with frequency-selective waveguide feedback circuits. Deploying intra-cavity ring resonators as feedback filters, implemented using low-loss Si_3N_4 waveguides, enables single-mode laser operation with wavelength tunability over very wide ranges. Using high-Q ring resonators for cavity length extension is also very effective for improving the laser's short-term frequency stability, which shows as an ultra-narrow intrinsic (Schawlow-Townes) linewidth. We demonstrate in this thesis that these lasers are also continuously tunable, that the spectral coverage can be extended from the infrared to the visible range, and that these lasers can be frequency locked to optical references to greatly enhance their long-term frequency stability.

In chapters 1 and 2 we describe an introduction to the field of chip-integrated lasers and the relevant theory regarding optical feedback circuits and laser frequency stability. In chapter 3, we present a novel method to increase the range of continuous tuning for hybrid-integrated diode lasers, based on feedback from ring resonators. Although laser cavity length extension using high-Q ring resonators is highly effective for obtaining ultra-narrow linewidths, it also decreases the wavelength range of continuous laser tuning that can be achieved with a given phase shift of an intracavity phase tuning element. To increase the range of continuous tuning to that of a short equivalent laser cavity, while maintaining the ultra-narrow linewidth of a long cavity, we describe an analytical model for synchronous tuning of the ring resonators with an intracavity phase tuning element. This method is confirmed with an experimental demonstration by recording Doppler broadened absorption lines of acetylene (C_2H_2) molecules using a hybrid-integrated InP-Si_3N_4 diode laser. The laser has a 120-nm coverage around 1540 nm, a maximum output power of 24 mW, and a lowest intrinsic linewidth of 2.2 kHz. We demonstrate a six-fold increased continuous and mode-hop-free tuning range of 0.22 nm (28 GHz) as compared to the free-spectral range of the laser cavity.

In chapter 4 we present the first realization of a hybrid-integrated diode laser in the visible spectral range. Before this, all previous realizations of such lasers had been restricted to the infrared. Providing chip-sized diode lasers to generate visible light with wide tunability and high frequency stability is of great interest for applications in biophotonics, precision metrology and quantum technology. For this demonstration in the 685-nm (red) wavelength range, we coupled an AlGaInP optical amplifier with a Si_3N_4 circuit for feedback from a ring resonator-based spectral filter. The laser

delivers up to 4.8 mW output power, has a spectral coverage of 10.8 nm around 684.4 nm wavelength and exhibits a low intrinsic linewidth of 2.3 ± 0.2 kHz.

In chapter 5 we describe our results on long-term frequency stabilization of a hybrid-integrated laser with a ring-resonator based extended cavity, by electronic locking to two optical references. Although feedback from high-Q ring resonators improves the laser's short-term frequency stability, long-term stability is often also required. By locking a widely tunable hybrid-integrated laser with a central wavelength of 1550 nm to suitable references, namely a fiber-based optical frequency discriminator (OFD), and an acetylene absorption line, we greatly enhance the laser's long-term frequency stability. Locking the laser to the OFD improves the laser's fractional frequency stability down to $1.5 \cdot 10^{-12}$ over an averaging time of 0.5 ms. Locking the laser frequency to an acetylene absorption line, reduces the residual frequency deviations of the laser to a range of less than 12 MHz within 5 days.

The thesis is concluded with chapter 6, where we provide an outlook to the exciting developments that can be expected regarding these widely-tunable and ultra-stable hybrid-integrated diode lasers.

Samenvatting

Dit proefschrift beschrijft ons onderzoek naar diodelasers gebaseerd op hybride integratie met frequentieselectieve feedbackcircuits gebaseerd op golfgeleiders. Door intra-cavity ringresonatoren in te zetten als feedbackfilters, geïmplementeerd met behulp van Si_3N_4 golfgeleiders met een laag verlies, wordt single-mode laserwerking mogelijk gemaakt met golflengteverstemming over zeer brede bereiken. Het gebruik van hoge-Q-ringresonatoren voor het verlengen van de laserholte is ook zeer effectief voor het verbeteren van de frequentiestabiliteit van de laser op korte termijn, wat tot uiting komt in een ultra-smalle intrinsieke (Schawlow-Townes) lijnbreedte. We laten in dit proefschrift zien dat deze lasers ook continu verstembaar zijn, dat het spectrale bereik kan worden uitgebreid van het infrarood naar het zichtbare bereik, en dat deze lasers in frequentie kunnen worden gestabiliseerd aan een optische referentie om de frequentiestabiliteit op lange termijn aanzienlijk te verbeteren.

In de hoofdstukken 1 en 2 beschrijven we een inleiding op het gebied van lasers geïntegreerd op chip en de relevante theorie met betrekking tot optische feedbackcircuits en laserfrequentiestabiliteit. In hoofdstuk 3 presenteren we een nieuwe methode om het bereik van continue verstemming voor hybride-geïntegreerde diodelasers te vergroten, gebaseerd op feedback van ringresonatoren. Hoewel de verlenging van de laserholte met behulp hoge-Q ringresonatoren zeer effectief is voor het verkrijgen van ultrasmalle lijnbreedtes, verkleint het ook het golflengtebereik van continue laserafstemming dat kan worden bereikt met een gegeven faseverschuiving van een verstemmingselement in de laserholte. Om het bereik van continue verstemming te vergroten tot dat van een korte equivalente laserholte, terwijl de smalle lijnbreedte van een lange laserholte behouden blijft, beschrijven we een analytisch model voor synchrone afstemming van de ringresonatoren met een fase-verstemmingselement in de laserholte. Deze methode wordt bevestigd met een experimentele demonstratie door Doppler-verbrede absorptielijnen van acetyleen (C_2H_2) moleculen vast te leggen met behulp van een hybride-geïntegreerde InP-Si_3N_4 diodelaser. De laser heeft een golflengtebereik van 120 nm rond 1540 nm, een maximaal uitgangsvermogen van 24 mW en een laagste intrinsieke lijnbreedte van 2.2 kHz. We demonstreren een zesvoudig vergroot continu en mode-hop-vrij verstemmingsbereik van 0.22 nm (28 GHz) ten opzichte van het vrije spectrale bereik van de laserholte.

In hoofdstuk 4 presenteren we de eerste realisatie van een hybride-geïntegreerde diodelaser in het zichtbare spectrale bereik. Voordien waren alle eerdere realisaties van dergelijke lasers beperkt tot het infrarood. Het leveren van diodelasers ter

grootte van een chip om zichtbaar licht te genereren met een brede verstembaarheid en hoge frequentiestabiliteit is van groot belang voor toepassingen in biofotonica, precisiemetrologie en kwantumtechnologie. Voor deze demonstratie in het golflengte-bereik van 685 nm (rood) hebben we een AlGaInP optische versterker gekoppeld aan een Si_3N_4 circuit voor feedback van een op ringresonatoren gebaseerd spectraal filter. De laser levert een uitgangsvermogen van maximaal 4.8 mW, heeft een verstem-baarheid van 10.8 nm rond een golflengte van 684.4 nm en heeft een lage intrinsieke lijnbreedte van 2.3 ± 0.2 kHz.

In hoofdstuk 5 beschrijven we onze resultaten op het gebied van frequentiestabili-satie op lange termijn van een hybride geïntegreerde laser met een op ringresonatoren gebaseerde laserholte, door elektronische stabilisatie aan twee optische referenties. Hoewel feedback van hoge-Q ringresonatoren de frequentiestabiliteit van de laser op de korte termijn verbetert, is stabiliteit op de lange termijn vaak ook vereist. Door een breed verstembare hybride-geïntegreerde laser met een centrale golflengte van 1550 nm te stabiliseren aan geschikte referenties, namelijk een op glasvezels gebaseerde opti-sche frequentiediscriminator (OFD) en een acetyleen absorptielijn, verbeteren we de frequentiestabiliteit van de laser op de lange termijn aanzienlijk. Het stabiliseren van de laser aan de OFD verbetert de fractionele frequentiestabiliteit van de laser tot $1.5 \cdot 10^{-12}$ over een middelingstijd van 0.5 ms. Door de laserfrequentie aan een ab-sorptielijn van acetyleen te stabiliseren, worden de resterende frequentieafwijkingen van de laser teruggebracht tot een bereik van minder dan 12 MHz over een periode van 5 dagen.

We sluiten het proefschrift af in hoofdstuk 6, waar we een vooruitblik geven op de ontwikkelingen die kunnen worden verwacht met betrekking tot deze breed verstem-bare en ultrastabiele hybride-geïntegreerde diodelasers.

List of publications

Journal articles

- **Albert van Rees**[1], Lisa V. Winkler[1], Pierre Brochard, Dimitri Geskus, Peter J. M. van der Slot, Christian Nölleke, and Klaus J. Boller, "Long-term Absolute Frequency Stabilization of a Hybrid-Integrated InP-Si$_3$N$_4$ Diode Laser," IEEE Photonics J. **15**(5), 1502408 (2023).

- Roel Botter, Jasper van den Hoogen, Akhileshwar Misra, Kaixuan Ye, **Albert van Rees**, Marcel Hoekman, Klaus Boller, and David Marpaung, "Observation of a Brillouin dynamic grating in silicon nitride waveguides," arXiv. 2308.09814 (2023).

- Cornelis A. A. Franken, Ward A. P. M. Hendriks, Lisa V. Winkler, Meindert Dijkstra, Adriano Ricardo do Nascimento Jr., **Albert van Rees**, M. R. Soheila Mardani, Ronald Dekker, Joost van Kerkhof, Peter J. M. van der Slot, Sonia M. García Blanco, and Klaus-J. Boller, "Hybrid integrated lasers in the deep-UV capable InP-Al$_2$O$_3$ platform," arXiv. 2302.11492 (2023).

- Hatam Mahmudlu, Robert Johanning, **Albert van Rees**, Anahita Khodadad Kashi, Jörn P. Epping, Raktim Haldar, Klaus-J. Boller, and Michael Kues, "Fully on-chip photonic turnkey quantum source for entangled qubit/qudit state generation," Nat. Photonics **17**, 518–524 (2023).

- Cornelis A. A. Franken[1], **Albert van Rees**[1], Lisa V. Winkler, Youwen Fan, Dimitri Geskus, Ronald Dekker, Douwe H. Geuzebroek, Carsten Fallnich, Peter J. M. van der Slot, and Klaus-J. Boller, "Hybrid-integrated diode laser in the visible spectral range," Opt. Lett. **46**(19), 4904–4907 (2021). **Spotlight on Optics.**

- Jesse Mak, **Albert van Rees**, Rob E. M. Lammerink, Dimitri Geskus, Youwen Fan, Peter J. M. van der Slot, Chris G. H. Roeloffzen, and Klaus-J. Boller, "High spectral purity microwave generation using a dual-frequency hybrid integrated semiconductor-dielectric waveguide laser," OSA Continuum **4**(8), 2133–2142 (2021). **Editors' pick.**

---

[1]Both authors contributed equally to this work.

- Youwen Fan, **Albert van Rees**, Peter J. M. van der Slot, Jesse Mak, Ruud M. Oldenbeuving, Marcel Hoekman, Dimitri Geskus, Chris G. H. Roeloffzen, and Klaus-J. Boller, "Hybrid integrated InP-Si$_3$N$_4$ diode laser with a 40-Hz intrinsic linewidth," Opt. Express **28**(15), 21713–21728 (2020).

- **Albert van Rees**, Youwen Fan, Dimitri Geskus, Edwin Klein, Ruud M. Oldenbeuving, Peter J. M. van der Slot, and Klaus-J. Boller, "Ring resonator enhanced mode-hop-free wavelength tuning of an integrated extended-cavity laser," Opt. Express **28**(4), 5669–5683 (2020).

- Klaus-J. Boller, **Albert van Rees**, Youwen Fan, Jesse Mak, Rob E. M. Lammerink, Cornelis A. A. Franken, Peter J. M. van der Slot, David A. I. Marpaung, Carsten Fallnich, Jörn P. Epping, Ruud M. Oldenbeuving, Dimitri Geskus, Ronald Dekker, Ilka Visscher, Robert Grootjans, Chris G. H. Roeloffzen, Marcel Hoekman, Edwin J. Klein, Arne Leinse, and René G. Heideman, "Hybrid Integrated Semiconductor Lasers with Silicon Nitride Feedback Circuits," Photonics **7**(1), 4 (2019).

- Jesse Mak, **Albert van Rees**, Youwen Fan, Edwin J. Klein, Dimitri Geskus, Peter J. M. van der Slot, and Klaus-J. Boller, "Linewidth narrowing via low-loss dielectric waveguide feedback circuits in hybrid integrated frequency comb lasers," Opt. Express **27**(9), 13307–13318 (2019).

Patent

- **Albert van Rees**, Klaus-J. Boller, Ruud-M. Oldenbeuving, Dimitri Geskus, "Integrated-optics-based external-cavity laser configured for mode-hop-free wavelength tuning," WO/2020/148656 (2020)

Conference proceedings

- Hatam Mahmudlu, Raktim Haldar, Robert Johanning, Anahita Khodadad Kashi, **Albert van Rees**, Jörn P. Epping, Klaus-J. Boller, and Michael Kues, "Fully On-chip Laser-integrated Quantum Source of Entangled Photon States," in *Conference on Lasers and Electro-Optics Europe & European Quantum Electronics Conference*, paper CD14.1 (2023).

- Lisa V. Winkler, Kirsten Gerritsma, **Albert van Rees**, Philip P. J. Schrinner, Marcel Hoekman, Ronald Dekker, Peter J. M. van der Slot, Christian Nölleke, and Klaus-J. Boller, "Tunable Hybrid-Integrated Diode Laser at 637 nm," in *Conference on Lasers and Electro-Optics Europe & European Quantum Electronics Conference*, paper CB5.1 (2023).

- Raktim Haldar, Hatam Mahmudlu, Robert Johanning, Anahita Khodadad Kashi, **Albert van Rees**, Jörn P. Epping, Klaus-J. Boller, and Michael Kues, "Fully On-chip Laser-integrated Entangled Photon Pair Source," in *European Conference on Integrated Optics*, F1.2 (2023).

- Lisa V. Winkler, Kirsten Gerritsma, **Albert van Rees**, Philip P. J. Schrinner, Marcel Hoekman, Ronald Dekker, Peter J. M. van der Slot, Christian Nölleke, and Klaus-J. Boller, "Silicon nitride hybrid-integrated diode laser at 637 nm," in *SPIE Proceedings 12424, Integrated Optics: Devices, Materials, and Technologies XXVII*, 124241K (2023).

- Anzal Memon, **Albert van Rees**, Jesse Mak, Youwen Fan, Peter J. M. van der Slot, Hubertus M. J. Bastiaens and Klaus-J. Boller, "Using hybrid, integrated InP-Si$_3$N$_4$ mode-locked diode lasers for the generation of sub-GHz repetition rate frequency combs," in *SPIE Proceedings 12424, Integrated Optics: Devices, Materials, and Technologies XXVII*, 124240H (2023).

- Cornelis A. A. Franken, Ward A. P. M. Hendriks, Meindert Dijkstra, Adriano Ricardo do Nascimento Jr., Lisa V. Winkler, **Albert van Rees**, M. R. Soheila Mardani, Ronald Dekker, Joost van Kerkhof, Peter J. M. van der Slot, Sonia M. García Blanco, and Klaus-J. Boller, "Ultra-violet hybrid integrated diode laser in the aluminium oxide PIC platform," in *SPIE Proceedings 12424, Integrated Optics: Devices, Materials, and Technologies XXVII*, PC124240A (2023).

- Hatam Mahmudlu, Raktim Haldar, Robert Johanning, Anahita Khodadad Kashi, **Albert van Rees**, Jörn P. Epping, Klaus-J. Boller, and Michael Kues, "Fully on-chip photonic turnkey quantum light source of two- and high-dimensional entangled photons," in *SPIE Proceedings 12424, Integrated Optics: Devices, Materials, and Technologies XXVII*, PC124240E (2023).

- Lisa V. Winkler, **Albert van Rees**, Kirsten Gerritsma, Marcel Hoekman, Philip P. J. Schrinner, Ronald Dekker, Peter J. M. van der Slot, Christian Nölleke, and Klaus-J. Boller, "637-nm High-Confinement SiN Waveguide Feedback Circuits for Hybrid-Integrated Diode Lasers," in *Proceedings of the 27th Annual Symposium of the IEEE Photonics Society Benelux*, (2022).

- Anzal Memon, **Albert van Rees**, Jesse Mak, Youwen Fan, Peter J. M. van der Slot, Hubertus M. J. Bastiaens and Klaus-J. Boller, "Generation of optical frequency combs at sub-GHz repetition rates with a hybrid-integrated mode-locked diode laser," in *Proceedings of the 27th Annual Symposium of the IEEE Photonics Society Benelux*, (2022).

- Raktim Haldar, Hatam Mahmudlu, Robert Johanning, Anahita Khodadad Kashi, **Albert van Rees**, Jörn P. Epping, Klaus-J. Boller, and Michael Kues, "Fully On-chip Electrically-pumped Laser-integrated Two and High-dimensional Entangled Photon Pair Source, " in *Frontiers in Optics + Laser Science*, paper FTh3E.6 (2022).

- Anzal Memon, **Albert van Rees**, Jesse Mak, Youwen Fan, Peter J. M. van der Slot, Hubertus M. J. Bastiaens and Klaus-J. Boller, "Generation of low repetition rate frequency combs with a hybrid integrated InP-Si$_3$N$_4$ diode laser" in *European Semiconductor Laser Workshop*, 71–72 (2022).

- **Albert van Rees**, Lisa V. Winkler, Peter J. M. van der Slot, Christian Nölleke, and Klaus J. Boller, "Long-term Frequency Stabilization of a Hybrid-integrated InP-Si$_3$N$_4$ Diode Laser, " in *Optica Advanced Photonics Congress*, paper IM4C.3 (2022).

- Lisa V. Winkler, **Albert van Rees**, Peter J. M. van der Slot, and Klaus-J. Boller, "Frequency stabilization of a hybrid-integrated InP-Si$_3$N$_4$ diode laser by locking to a fiber ring resonator," in *Proceedings of the 26th Annual Symposium of the IEEE Photonics Society Benelux*, (2021).

- **Albert van Rees**, Youwen Fan, Jesse Mak, Rob E. M. Lammerink, Cornelis A. A. Franken, Ruud M. Oldenbeuving, Dimitri Geskus, Jörn P. Epping, Marcel Hoekman, Ronald Dekker, Edwin J. Klein, Douwen H. Geuzebroek, Chris G. H. Roeloffzen, Carsten Fallnich, Peter J. M. van der Slot, and Klaus-J. Boller, "Narrow-linewidth hybrid-integrated semiconductor lasers by exploiting feedback from Si$_3$N$_4$ circuits," in *SPIE Proceedings **11692**, Optical Interconnects XXI*, 1169209 (2021). **Invited presentation.**

- **Albert van Rees**, Cornelis A. A. Franken, Youwen Fan, Dimitri Geskus, Ronald Dekker, Douwe H. Geuzebroek, Carsten Fallnich, Peter J. M. van der Slot, and Klaus-J. Boller, "Realization of a Hybrid Integrated Diode Laser for Visible Light," in *European Conference on Integrated Optics* (2020).

- Cornelis A. A. Franken, **Albert van Rees**, Youwen Fan, Dimitri Geskus, Ronald Dekker, Douwe H. Geuzebroek, Carsten Fallnich, Peter J. M. van der Slot, and Klaus-J. Boller, "First realization of a hybrid integrated diode laser in the visible spectral range," in *SPIE Proceedings **11301**, Novel In-Plane Semiconductor Lasers XIX*, 1130106 (2020).

- Jörn P. Epping, Arne Leinse, Ruud M. Oldenbeuving, Ilka Visscher, Douwe H. Geuzebroek, Dimitri Geskus, **Albert van Rees**, Klaus-J. Boller, Michael Theurer, Martin Möhrle, Martin Schell, Chris G. H. Roeloffzen, and René G. Heideman, "Hybrid integrated silicon nitride lasers," in *SPIE Proceedings **11274**, Physics and Simulation of Optoelectronic Devices XXVIII*, 112741L (2020).

- **Albert van Rees**, Dimitri Geskus, Edwin J. Klein, Youwen Fan, Peter J. M. van der Slot, and Klaus-J. Boller, "Mode-Hop-Free Tuning of a Chip-Based Hybrid Integrated InP-Si$_3$N$_4$ Laser," in *OSA Technical Digest, Conference on Lasers and Electro-Optics Europe and European Quantum Electronics Conference*, paper cb_3_5 (2019).

- Jesse Mak, **Albert van Rees**, Youwen Fan, Edwin J. Klein, Dimitri Geskus, Peter J. M. van der Slot, and Klaus-J. Boller, "Narrow Intrinsic Linewidth Frequency Combs from a Chip-Based Hybrid Integrated InP-Si$_3$N$_4$ Diode Laser," in *OSA Technical Digest, Conference on Lasers and Electro-Optics*, paper STu4N.4 (2019).

- Youwen Fan, Jesse Mak, **Albert van Rees**, Edwin J. Klein, and Klaus-J. Bolter, "Extended-Cavity Single-Frequency Semiconductor Lasers using Ring Filters in Low-Loss SiN Technology," in *IEEE International Semiconductor Laser Conference*, 25–26 (2018).

Acknowledgements

As I write this, at the end of the year 2023, it is time to look back on a period of more than 4 years of research during my PhD and almost 6 years if I also include my MSc assignment. I am grateful and happy that I can now finish this period. During this time, many people around me have contributed in different ways. They have pushed me to keep going, supported me when things got more difficult, and helped me to achieve nice results.

First of all, I would like to thank my promotor Klaus. Thank you very much for your guidance and the many hours you have spent correcting and improving texts and presentations. I am very grateful for the freedom you offer to PhD students to follow their path and conduct their own research. Thank you for all explanations of difficult physics with funny examples. Flying as a passenger in your glider plane was also a great experience!

Peter, my co-promotor and daily supervisor, thank you for your helpfulness. You were always available to check and derive a challenging equation, and to have a critical look at the details of a text. I will remember the delicious food that you prepared and the accompanying wines that you selected for group barbecues and dinners!

I would like to thank the other members of the graduation committee, Prof. Maurizio Burla, Prof. Carsten Fallnich, Prof. Herman Offerhaus and Prof. Pepijn Pinkse, for their valuable time to be part of this committee and to read and provide feedback on my thesis.

A special thanks for my fellow PhD students. Youwen, you inspired me with your enthusiasm for these lasers during my MSc assignment, and, even more, with several unanswered questions to challenge me. Jesse, you introduced me to these lasers with the many options for the design of different feedback circuits. Thank you for the many talks we had in our office and for explaining to me the day-to-day affairs of the group. Caterina, thanks for your hospitality, when I first arrived in the group, and for your encouragements for my first talk! Lisa, it was great to make experiments successful together, even when it required travelling to Le Mans and München! I will remember the times we had our "Sprachtandem" where we exchanged our culture and language in many fun ways. Kees, I liked our conversations to understand experiments and thanks for sharing your experiences from Harvard. Anzal, I want to thank you for your kindness, I admire your persistence and determination to move forward. Lisi, I always enjoyed the many small chats with you in the office, and, during our trip to a

conference in Belgium. Roel and Yvan, thanks for exchanging experiences on how to deal with all the Twente Graduate School (TGS) requirements!

I would also like to thank the other staff members. Bert, you always come up with an interesting question or a nice experience to discuss. David, thank you for breathing new life into the group, with your ideas, people and equipment. Carla, thank you for your support, and for the many fun and serious topics that you brought up during the lunch breaks.

During my research I had the honor to supervise students for their BSc and MSc assignments. Rob, Kees, Lida and Constantijn, I enjoyed performing measurements together, and discussing the questions that you asked me. Kirsten, I also enjoyed introducing you to these lasers, when Lisa was still on holiday.

I thank the rest of the group for the nice atmosphere and the chats and discussions during the lunch and coffee breaks. Thank you: Ahmet, Akhileshwar, Akshay, Aldi, Bas, Björn, Gaojian, Govert, Haider, Jasper, Lou, Maarten, Martijn, Max, Okky, Pieter, Radius, Randy, Redlef, Robert, Roland, Roos, Sam, Steven, Suze, Thomas, Victoria, Xin, and Zheng.

The results described in this thesis were also made possible through the support and cooperation with the companies LioniX, Chilas, PHIX and QuiX. I am particularly grateful to the enthusiastic support of Dimitri. You were always available to help me solve any laser issue, to fix broken assemblies, to offer some leftover space on wafer runs and to come up with creative solutions. In addition, I would like to thank many more people at these companies, who were very supportive, especially Arjan, Arne, Chris, Hans, Jörn, Douwe, Edwin, Erik, Lennart, Marcel, Philip, René, Robert, Ronald and Ruud. Currently, as I write this, I am employed by one of these companies, Chilas, where we further develop and market the lasers as described in this thesis. I enjoy being part of an enthusiastic team with Dimitri, Fathema, Hans, Ian, Rob, Sami, and Wilson. Thank you all for your patience during the last weeks, when I had to finish writing this thesis.

I want to thank our colleagues within the Applied Nanophotonics (ANP) cluster for the nice events and the interesting discussions. Thanks also to our partners in the 3PEAT project, who made this a successful project. The monthly telcos and semi-annual meetings were a nice experience. I also would like to thank Silentsys and Toptica for their support with measuring equipment and their hospitality to perform measurements on-site. Thanks to Prof. Michael Kues and his group in Hannover for the interesting scientific discussions about using hybrid lasers as a quantum source.

Finally, I am very grateful to my friends and family who always supported me throughout my life, study, and research. Marko, thank you for your friendship and support during our study time and PhDs. Papa, mama, Maria, en Richard, bedankt voor jullie steun, vooral in de tijd dat mijn studie moeizaam ging, en voor jullie interesse in mijn onderzoek!